



**AFRL-RB-WP-TR-2007-3116**

## **CJ2 ICING EFFECTS SIMULATOR**

**Delivery Order 0019: Development of an Icing Effects Simulation for a Typical Business Jet Configuration**

**Billy Barnhart  
Bihrl Applied Research, Inc.**

**AUGUST 2007  
Final Report**

**Approved for public release; distribution unlimited.**

*See additional restrictions described on inside pages*

**AIR FORCE RESEARCH LABORATORY  
AIR VEHICLES DIRECTORATE  
WRIGHT-PATTERSON AIR FORCE BASE, OH 45433-7542  
AIR FORCE MATERIEL COMMAND  
UNITED STATES AIR FORCE**

## NOTICE

Using Government drawings, specifications, or other data included in this document for any purpose other than Government procurement does not in any way obligate the U.S. Government. The fact that the Government formulated or supplied the drawings, specifications, or other data does not license the holder or any other person or corporation; or convey any rights or permission to manufacture, use, or sell any patented invention that may relate to them.

This report was cleared for public release by the Air Force Research Laboratory Wright Site (AFRL/WS) Public Affairs Office (PAO) and is releasable to the National Technical Information Service (NTIS). It will be available to the general public, including foreign nationals.

THIS TECHNICAL REPORT IS APPROVED FOR PUBLICATION.

\*//signature//

---

THOMAS J. CORD, Project Engineer

//signature//

---

DENIS P. MROZINSKI, Chief  
Aero Configuration Branch

//signature//

---

MICHAEL J. STANEK, Tech Advisor  
Aero Sciences Division

This report is published in the interest of scientific and technical information exchange and its publication does not constitute the Government's approval or disapproval of its ideas or findings.

\*Disseminated copies will show “//signature//” stamped or typed above the signature blocks.

<b>REPORT DOCUMENTATION PAGE</b>				<i>Form Approved</i> OMB No. 0704-0188				
The public reporting burden for this collection of information is estimated to average 1 hour per response, including the time for reviewing instructions, searching existing data sources, gathering and maintaining the data needed, and completing and reviewing the collection of information. Send comments regarding this burden estimate or any other aspect of this collection of information, including suggestions for reducing this burden, to Department of Defense, Washington Headquarters Services, Directorate for Information Operations and Reports (0704-0188), 1215 Jefferson Davis Highway, Suite 1204, Arlington, VA 22202-4302. Respondents should be aware that notwithstanding any other provision of law, no person shall be subject to any penalty for failing to comply with a collection of information if it does not display a currently valid OMB control number. <b>PLEASE DO NOT RETURN YOUR FORM TO THE ABOVE ADDRESS.</b>								
<b>1. REPORT DATE (DD-MM-YY)</b> August 2007		<b>2. REPORT TYPE</b> Final		<b>3. DATES COVERED (From - To)</b> 29 September 2003 – 08 September 2006				
<b>4. TITLE AND SUBTITLE</b> CJ2 ICING EFFECTS SIMULATOR Delivery Order 0019: Development of an Icing Effects Simulation for a Typical Business Jet Configuration				<b>5a. CONTRACT NUMBER</b> F33615-98-D-3601-0019				
				<b>5b. GRANT NUMBER</b>				
				<b>5c. PROGRAM ELEMENT NUMBER</b> 62201F				
<b>6. AUTHOR(S)</b> Billy Barnhart				<b>5d. PROJECT NUMBER</b> A06M				
				<b>5e. TASK NUMBER</b>				
				<b>5f. WORK UNIT NUMBER</b> 0A				
<b>7. PERFORMING ORGANIZATION NAME(S) AND ADDRESS(ES)</b>  Bihrl Applied Research, Inc. 400 Jericho Pike Jericho, NY 11753				<b>8. PERFORMING ORGANIZATION REPORT NUMBER</b>  BAR07-13				
<b>9. SPONSORING/MONITORING AGENCY NAME(S) AND ADDRESS(ES)</b>  Air Force Research Laboratory Air Vehicles Directorate Wright-Patterson Air Force Base, OH 45433-7542 Air Force Materiel Command United States Air Force				<b>10. SPONSORING/MONITORING AGENCY ACRONYM(S)</b> AFRL/RBAA				
				<b>11. SPONSORING/MONITORING AGENCY REPORT NUMBER(S)</b> AFRL-RB-WP-TR-2007-3116				
<b>12. DISTRIBUTION/AVAILABILITY STATEMENT</b> Approved for public release; distribution unlimited.								
<b>13. SUPPLEMENTARY NOTES</b> PAO case number AFRL/WS 07-0497, 19 Nov 2007.								
<b>14. ABSTRACT</b> In this effort, Cessna Aircraft Company and Bihrl Applied Research teamed to develop and validate flight simulation models of a typical business jet incorporating the effects of various forms of ice. The ice conditions considered were: - Icing protection system failure ice - Inter-cycle (roughness) ice - Run-back ice. The study entailed wind tunnel tests of different scale wing panels with a wide range of Reynolds numbers to look at how ice effects scaled from a low-speed subscale model to the fullscale airplane. Complete airplane tests were then performed on a 1/12-scale model of the business jet to collect static and dynamic data required for development of a simulation model of the airplane with and without the various ice configurations. The wind tunnel data, properly adjusted for Reynolds number corrections, was used to construct simulation math models of the clean and iced airplane. In order to validate the models, a flight test program was undertaken to collect flight data the ice configurations. The math models were then incorporated into NASA's Ice Contamination Effects Flight Training Device and evaluated by the airframe manufacturer's test pilots. The simulator showed very good agreement with flight results for each of the ice conditions.								
<b>15. SUBJECT TERMS</b> certification testing, wind tunnel tests								
<b>16. SECURITY CLASSIFICATION OF:</b> <table border="1" style="width: 100%; border-collapse: collapse; margin-top: 5px;"> <tr> <td style="width: 33%; padding: 2px;"><b>a. REPORT</b> Unclassified</td> <td style="width: 33%; padding: 2px;"><b>b. ABSTRACT</b> Unclassified</td> <td style="width: 33%; padding: 2px;"><b>c. THIS PAGE</b> Unclassified</td> </tr> </table>			<b>a. REPORT</b> Unclassified	<b>b. ABSTRACT</b> Unclassified	<b>c. THIS PAGE</b> Unclassified	<b>17. LIMITATION OF ABSTRACT:</b> SAR		<b>18. NUMBER OF PAGES</b> 98
<b>a. REPORT</b> Unclassified	<b>b. ABSTRACT</b> Unclassified	<b>c. THIS PAGE</b> Unclassified						
<b>19a. NAME OF RESPONSIBLE PERSON (Monitor)</b> Thomas J. Cord <b>19b. TELEPHONE NUMBER (Include Area Code)</b> (937) 255-2074								

1. INTRODUCTION.....	1
2. NOMENCLATURE.....	2
2.1. Symbols:.....	2
2.2. Abbreviations:.....	3
3. WIND TUNNEL TESTS .....	4
3.1. Wing Panel Tests .....	4
3.1.1. Langley Full-Scale Wind Tunnel Tests .....	6
3.1.2. University of Illinois at Urbana-Champaign Wind Tunnel Tests.....	12
3.1.3. Results .....	16
3.2. Complete Airplane Model Tests.....	19
3.2.1. Model.....	19
3.2.2. Test Facility .....	29
3.2.3. Test Procedures .....	36
3.2.4. Test Conditions .....	27
3.2.5. Data Acquisition and Reduction .....	28
3.2.6. Data Presentation.....	29
3.2.7. LAMP Data Discussion.....	31
4. SIMULATION IMPLEMENTATION .....	48
4.1. Initial modeling.....	48
4.1.1. Baseline Airplane.....	48
4.1.2. Iced Airplane Configurations .....	63
4.2. Ice Contamination Effects Flight Training Device .....	63
5. VALIDATION DATA FLIGHT TEST PROGRAM .....	66
6. FINAL SIMULATION MODEL AND RESULTS.....	73
7. CONCLUDING REMARKS.....	80
8. REFERENCES .....	81

## SUMMARY

In an effort to improve flight safety, NASA's Aviation Safety and Security Program (AvSSP) set out to develop and validate complete aircraft test methods and flight simulation models with emphasis on pilot training and aircraft icing certification testing. As part of this effort, NASA teamed with Cessna Aircraft Company and Bihle Applied Research to develop and validate flight simulation models of a typical business jet that incorporates the effects of various forms of ice. The ice conditions considered were:

- Icing protection system failure ice
- Inter-cycle (roughness) ice
- Run-back ice.

The initial stage of the study entailed a series of wind tunnel tests of different scale wing panels with a wide range of Reynolds numbers to look at how the ice effects scaled from the planned low-speed sub-scale complete airplane model to the full-scale airplane. Once the wing panel tests were analyzed, the complete airplane tests were performed on a 1/12-scale model of the business jet to collect static and dynamic data required for development of a simulation model of the airplane with and without the various ice configurations.

The final stage of the program was to use the wind tunnel data, properly adjusted for Reynolds' Number corrections to construct simulation math models of the clean airplane, as well as for each of the studied ice configurations. In order to validate the models, a flight test program was undertaken to collect flight data of the airplane configuration flying with each of the identical ice configurations that were tested in the wind tunnel. The math models were then incorporated into NASA's Ice Contamination Effects Flight Training Device so that the models could be evaluated by the airframe manufacturer's test pilots. The simulator showed very good agreement with flight results for each of the ice conditions.

## 1. INTRODUCTION

In an effort to improve flight safety, NASA's Aviation Safety and Security Program (AvSSP) set out to develop and validate complete aircraft test methods and flight simulation models with emphasis on pilot training and aircraft icing certification testing. Specific objectives were to:

- 1) Develop piloted flight simulations to evaluate potentially risky flying qualities prior to development and certification flight tests with ice shapes, and
- 2) Develop piloted flight simulation models for operational training through higher-fidelity flight training devices.

To fulfill these objectives, NASA teamed with a business jet manufacturer and Bihrl Applied Research to develop and validate flight simulation models of a typical business jet that incorporates the effects of various forms of ice. Prior to this effort, NASA, Bihrl Applied Research and the Wichita State University developed and validated a flight simulation demonstrator for a turbo-prop commuter aircraft for pilot training (References 1,2, and 3)

The general methodology to develop the icing flight simulation models required static and dynamic wind tunnel testing of a subscale, complete aircraft model with and without ice shapes to develop a database of force and moment coefficients over a wide range of angles of attack, sideslip and control surface deflections. For the business jet simulation, a 1/12-scale complete aircraft model was used to develop the database for a no-ice baseline and three types of ice accretions. These were pre-activation roughness, runback shapes that form downstream of the thermal wing ice protection system, and a wing ice protection system failure shape.

Because of the significant reduction in both the geometry and the Reynolds number, a series of wind tunnel tests was conducted on wing panel models prior to the 1/12-scale complete aircraft model testing. These wing panel model tests examined the scaling relationship between the full-scale aircraft and the subscale model with the three icing cases (Reference 4). From this scaling study, the subscale ice shape size, position, and roughness were determined for the complete aircraft testing. The 1/12-scale complete aircraft model was then tested on a rotary force-balance at the Bihrl Applied Research Large Amplitude Multi-Purpose Tunnel to develop the icing effects data base (Reference 5). Using this database, high-fidelity flight simulation models for the baseline (no-ice) and three icing cases were developed using the Bihrl Applied Research simulation environment software called D-Six. A limited validation exercise was conducted on the baseline data using flight data provided by the manufacturer.

Additional flight test data with ice shapes were needed to validate the simulation models with the various forms of icing. Thus, a flight test program was conducted during September 2005 using a business jet to acquire the full-scale flight dynamics with the no-ice baseline and three icing cases. Finally, company pilots flew the simulator to evaluate how well the final simulation represented the real airplane.

## 2. NOMENCLATURE

### 2.1. Symbols:

The units for physical quantities used herein are presented in U.S. Customary Units.

$b$	wing span, ft
$\bar{c}$	mean aerodynamic chord, ft
$C_A$	axial-force coefficient, Axial force/ $\bar{q} S$
$C_L$	lift-force coefficient, Lift force/ $\bar{q} S$
$C_D$	drag-force coefficient, Drag force/ $\bar{q} S$
$C_N$	normal-force coefficient, Normal force/ $\bar{q} S$
$C_Y$	side-force coefficient, Side force/ $\bar{q} S$
$C_l$	body-axis rolling-moment coefficient, Rolling moment/ $\bar{q} S b$
$C_m$	pitching-moment coefficient, Pitching moment/ $\bar{q} S \bar{c}$
$C_n$	body-axis yawing-moment coefficient, Yawing moment/ $\bar{q} S b$
$p, q, r$	body-axis roll, pitch, yaw rates, rad/sec
$pb/2V$	non-dimensional roll rate
$\bar{q}, qbar$	free-stream dynamic pressure, lb/ft <sup>2</sup>
$qc/2V$	non-dimensional pitch rate
$rb/2V$	non-dimensional yaw rate
$S$	wing area, ft <sup>2</sup>
$V$	free-stream velocity, ft/sec
$\alpha$	angle of attack, AOA, positive nose up, deg
$\beta$	angle of sideslip, Beta, positive nose left (pilot's right ear windward), deg
$\Omega b/2V$	non-dimensionalized wind-axis rotation rate, positive for clockwise spin
$\delta_a$	aileron deflection, positive when trailing-edge is down, deg
$\delta_e, de$	elevator deflection, positive when trailing-edge is down, deg
$\delta_{flap}$	flap deflection, positive when trailing-edge is down, deg
$\delta_r$	rudder deflection, positive when trailing-edge is left, deg

## **2.2.      *Abbreviations:***

cg	center of gravity
FS	fuselage station
LAMP	Large Amplitude Multiple Purpose Wind Tunnel
LFSWT	Langley Full Scale Wind Tunnel
Re	Reynolds number
TE	Trailing-edge
UIUC	University of Illinois at Urbana-Champaign
WL	water line



### 3. WIND TUNNEL TESTS

The first series of wind tunnel tests were designed to provide scaling of the ice shapes. Consequently, a full-scale wing panel, an intermediate 5/12-scale wing panel and a 1/12-scale panel were each tested alone and with ice shapes at different Reynolds numbers to determine how the effects of the ice shapes scaled. After this was completed, a 1/12-scale complete model of the airplane was tested to generate the static and dynamic aerodynamic data required for development of a simulation model.

#### 3.1. *Wing Panel Tests*

Wind tunnel tests of two different scale wing panels were performed during the period 15 through 23 March 2004 in the Langley Full Scale Wind Tunnel (30' X 60') that is operated by Old Dominion University.

The models consisted of right wing panels with an aileron. One panel was a full-scale wing panel and the second one was a 5/12-scale panel of the same wing built specifically for this test. Both models had the capability to set the aileron deflection and measure the hinge moments. Figure 1 shows both of the models in the LFSWT test section. In this photograph, the 5/12-scale model is mounted for testing while the full-scale panel was only placed here for the photo – both were not mounted in the tunnel at the same time.

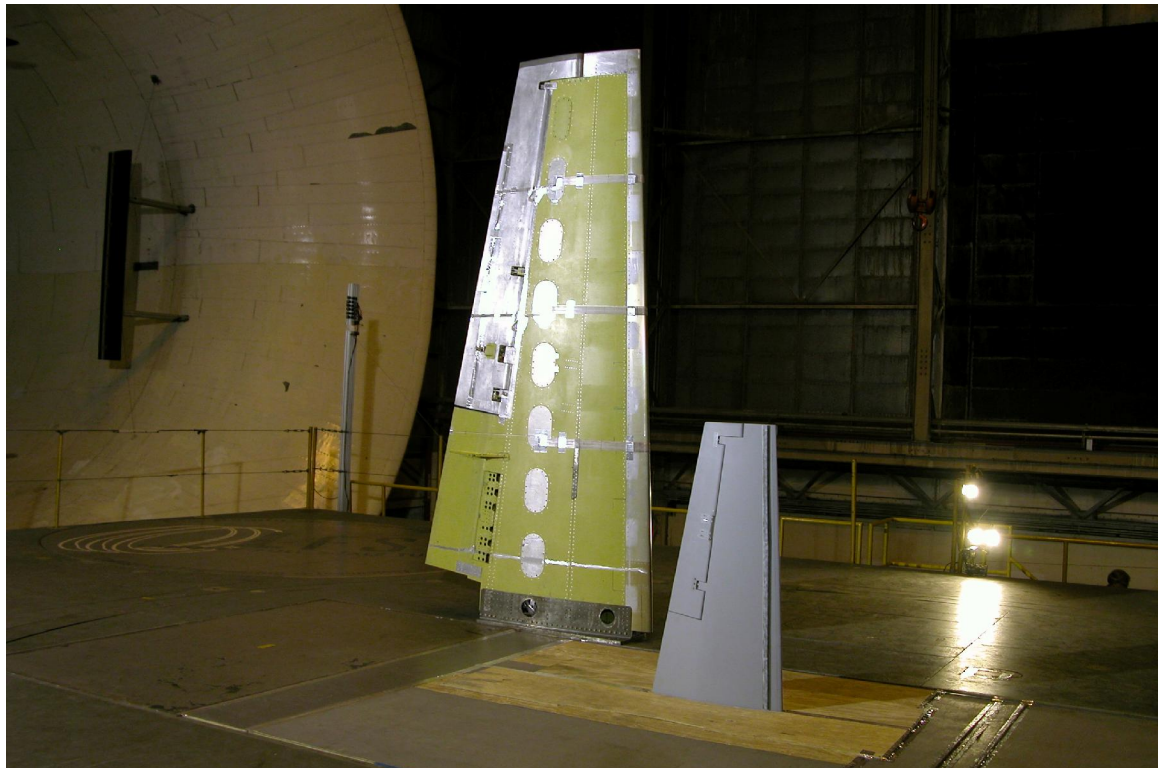


Figure 1. - Full-scale and 5/12-scale wing panels in LFSWT

A 1/12-scale model of the same wing panel was also constructed for testing at the University of Illinois at Urbana-Champaign (UIUC) during May of

2004. It was constructed of foam and fiberglass with aluminum spars. The aileron was deflectable and supplied with a hinge moment balance. The model had one chord-wise row of pressure taps. Figure 2 shows a photograph of the 1/12-scale model mounted in the University of Illinois 3'X4' wind tunnel.

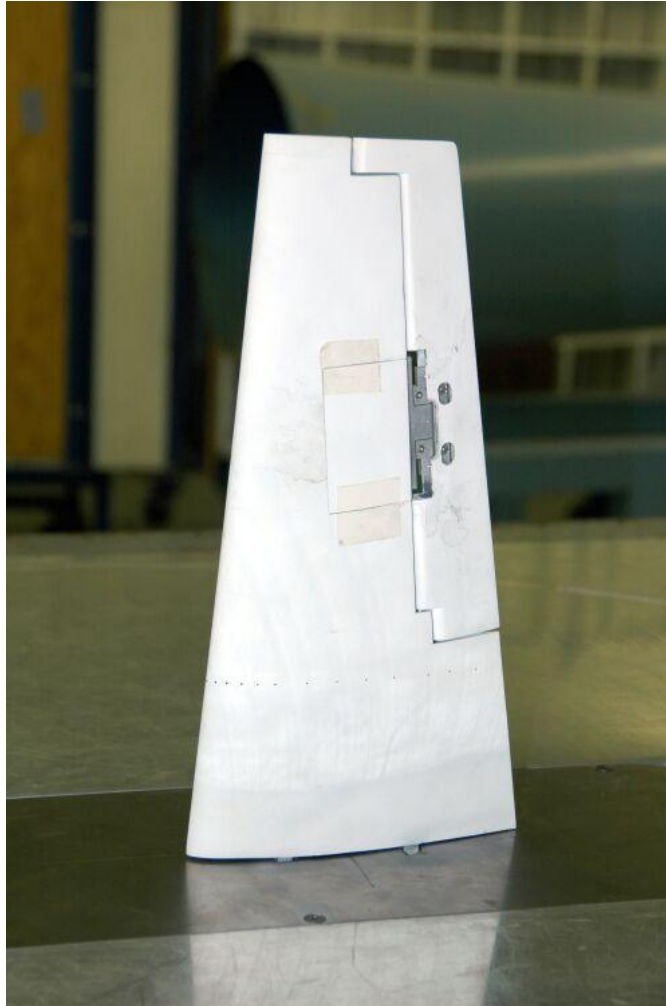


Figure 2. – 1/12-scale model mounted in UIUC wind tunnel.

As shown in Table 1, the tests were planned to span the Reynolds numbers from the maximum that could be obtained with the full-scale wing panel in the LFSWT to what would be used for the complete airplane static and dynamic testing with an overlap in  $Re$  at each scale.

Table 1. – Reynolds' Numbers tested with the three models

Scale	Q (psf)	Re	Comments
Full	15	4.1 million	Max Re in LFSWT
Full	2.6	1.7 million	Max Re for 5/12-scale model
5/12	15	1.7 million	Max Re in LFSWT
5/12	7	1.2 million	Intermediate case
5/12	2	0.6 million	Max Re for 1/12-scale model
1/12	50	0.6 million	Max Re in UIUC tunnel
1/12	18	0.4 million	Intermediate case
1/12	3	0.2 million	Re for LAMP test

Three ice conditions were chosen for this study:

- 22.5 minute ice-protection failure case
- 2 minute initial (pre-activation) ice accretion (roughness)
- a runback ice shape resulting from the leading edge thermal anti-ice system.

Table 2 presents the icing conditions for the failure and pre-activation ice. The failure case shapes were obtained using LEWICE. The pre-activation roughness were simulated with sandpaper/grit using the droplet impingement limits obtain from LEWICE. The runback shape was consistent with the shapes used during certification flights for this airplane.

Table 2. – Icing conditions for the failure and pre-activation shapes.

Ice Shape	Aircraft $\alpha$	V (KCAS)	LWC (g/m <sup>3</sup> )	MVD ( $\mu$ m)	OAT (F)
22.5-min. failure	3.08 deg	160	0.6	15	14
2 min. roughness	3.08 deg	160	0.3	15	-4

### 3.1.1. Langley Full-Scale Wind Tunnel Tests

The Langley Full-scale Wind Tunnel (LFSWT) has a test section that is nominally 30-ft. high, 60-ft. wide, with a quasi-elliptical cross-section, and is 56-ft. long. It is a closed-circuit, three-quarter open-jet, double-return, continuous flow design which operates at atmospheric pressure. It is capable of operating at speeds up to a dynamic pressure of 15.0 psf.

#### 3.1.1.1. Installation and Instrumentation

The two larger scale models tested in the LFSWT were mounted vertically in the test section and supported by NASA sidewall balances mounted to the

tunnel turn-table platform under the test section floor. The balances measured the force and moment data during the test. Because of the range of force and moment data expected with the different scale models two balances were used for these tests. For the full-scale wing panel the 1637-S balance was used and for the 5/12-scale wing panel the TDT-05S balance was used. A spacer was required between the wind tunnel turntable center support pedestal and the TDT-05S balance in order to have the test section floor at the same relative location on the spans of the two different scaled wing panels. This spacer was fabricated by the ODU shop. A sketch is shown in Figure 3 and a photograph of the model installation is shown in Figure 4.

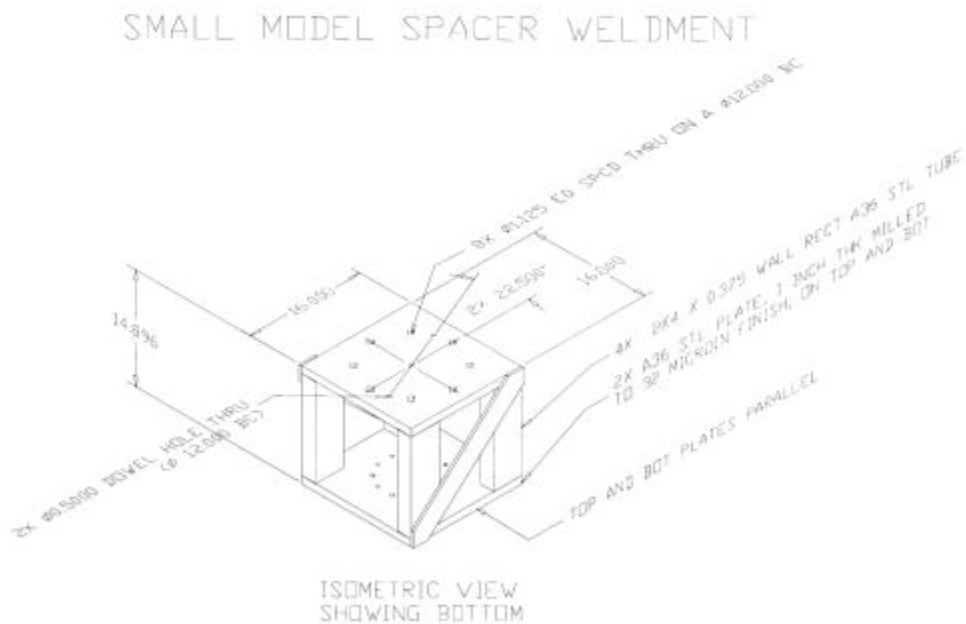


Figure 3. – Sketch of spacer constructed for proper placement of 5/12-scale model.

The BAR data acquisition and reduction system and software were used for collection and processing of the force and moment data. The pressure measurements were made using a PSI system, and the Old Dominion University's pressure data acquisition system was used to reduce and record the pressure data.

The full-scale wing was supplied with instrumentation for measuring the aileron hinge moments. For the 5/12-scale wing panel, a NASA 38 remote control fin balance was used to measure the aileron hinge moments. Parts were machined for mounting the balance within the wing and for setting the aileron deflection. The BAR data acquisition system was also used to take, process, and record the hinge moment data simultaneously with the wing panel force and moment data.



Figure 4. – Photograph of the installation of the 5/12-scale wing panel in the LFSWT showing the spacer mounted under the TDT-05S balance.

In addition, each of the models was instrumented for pressure measurements at three span-wise cuts, which were 51", 86", and 121" from the full-scale wing panel mounting flange. For the full-scale wing, pressure belts were attached to the wing for the pressure measurements. Each belt had 30 tap locations. The 5/12-scale model was pressure tapped at the same relative span-wise and chord-wise locations.

### 3.1.1.2. Ice Shapes

The full-scale runback shapes were constructed of insulation foam cut using a hotwire. The full-scale failure shape was constructed using a laser-sintering process. These shapes had 40-grit (nominal) roughness applied on them in order to simulate the ice roughness. The full-scale 2-minute roughness was simulated using 40-grit sandpaper. Figure 5 shows the full scale ice shapes.

The 5/12 scale failure and upper surface runback shapes were constructed by the laser-sintering process. The 5/12 scale lower-surface runback shape was constructed of foam cut with hotwire. These shapes had 80-grit roughness applied to them. Both 80-grit and 120-grit roughness (sandpaper) were used for representation of the 2-minute roughness case for the 5/12-scale model.

For all iced conditions, the ice shapes or roughness sandpaper were attached with double-sided tape.



Figure 5. – Full-scale model simulated ice shapes.

### 3.1.1.3. Test Programs

Table 3 shows the run program that was conducted in the LFSWT for the full-scale wing panel. Table 4 presents similar information for the 5/12-scale wing panel. As shown, two candidate equivalent runback shapes were considered during these tests, as well. For the 5/12-scale model, 80 and 120 grit sandpaper were also tested for the 2-minute roughness tests to check the effect of grit size on scaling.



Table 3 - Full-Scale Wing Panel Runs in LFSWT

Config	qbar	$\alpha$ 's	$\delta a$	File Name	Comments	
Wclean-25a	2.5	Sched B	-25	2CJFS1B	Clean Wing	
Wclean-10a			-10	2CJFS1D		
Wclean		Sched A	0	2CJFS1A		
		Sched B		2CJFS1AR		
		Sched A		2CJFS1A1		
Wclean+10a	Sched B	+10	2CJFS1E			
Wclean+25a		+25	2CJFS1C			
Wclean-25a	15		-25	15CJFS1B		
Wclean-10a			-10	15CJFS1D		
Wclean			0	15CJFS1A		
				15CJFS1AR		
Wclean+10a			+10	15CJFS1E		
Wclean+25a			+25	15CJFS1C		
Wlewise-25a			2.5	Sched D	-25	2CJFS2B
Wlewise-10a	Sched C	-10		2CJFS2D		
Wlewise	Sched B	0		2CJFS2A		
Wlewise+10a	Sched D	+10		2CJFS2E		
Wlewise+25a		+25		2CJFS2C		
Wlewise-25a	15		-25	15CJFS2B		
Wlewise-10a			-10	15CJFS2D		
Wlewise			0	15CJFS2A		
Wlewise+10a			+10	15CJFS2E		
Wlewise+25a			+25	15CJFS2C		
Wrough-25a	2.5	Sched D	-25	2CJFS3B	Roughness – 40 grit	
Wrough			0	2CJFS3A		
Wrough+25a			+25	2CJFS3C		
Wrough-25a	15	Sched E	-25	15CJFS3B		
Wrough			0	15CJFS3A		
Wrough+25a			+25	15CJFS3C		
Wrunback-25a	2.5	Sched E	-25	2CJFS4B	Runback	
Wrunback		Sched D	0	2CJFS4A		
		Sched E		2CJFS4AR		
Wrunback+25		15		+25		2CJFS4C
Wrunback-25a	-25			15CJFS4B		
Wrunback	0			15CJFS4A	Suction side ice section blew off by $14\alpha$	
				15CJFS4AR		
Wrunback+25	+25			15CJFS4C	Suction side ice section blew off, run terminated early @ $\alpha = 8$	

Schedule A:  $-4^\circ, 0^\circ, 4^\circ, 6^\circ, 7^\circ, 8^\circ, 9^\circ, 10^\circ, 11^\circ, 12^\circ, 13^\circ, 14^\circ, 15^\circ, 16^\circ, 17^\circ, 18^\circ, 20^\circ$

Schedule B:  $-4^\circ, 0^\circ, 4^\circ, 6^\circ, 8^\circ, 10^\circ, 12^\circ, 14^\circ, 16^\circ, 18^\circ, 19^\circ, 20^\circ, 21^\circ$

Schedule C:  $-4^\circ, 0^\circ, 4^\circ, 6^\circ, 8^\circ, 10^\circ, 11^\circ, 12^\circ, 13^\circ, 14^\circ, 15^\circ, 16^\circ, 17^\circ, 18^\circ, 19^\circ, 21^\circ$

Schedule D:  $-4^\circ, 0^\circ, 4^\circ, 6^\circ, 8^\circ, 10^\circ, 11^\circ, 12^\circ, 13^\circ, 14^\circ, 16^\circ, 18^\circ, 19^\circ, 21^\circ$

Schedule E:  $-4^\circ, 0^\circ, 4^\circ, 6^\circ, 8^\circ, 10^\circ, 12^\circ, 14^\circ, 15^\circ, 16^\circ, 17^\circ, 18^\circ, 19^\circ, 21^\circ$

Table 4 - 5/12-Scale Wing Panel Model Runs in LFSWT

Config	qbar	$\alpha$ 's	$\delta\alpha$	File Name	Comments
Wclean-25a	2.0	Sched G	-25	2CJ5121B	Clean
Wclean-10a			-10	2CJ5121D	
Wclean		Sched J	0	2CJ5121A	BLC off
Wclean+10a		Sched G	+10	2CJ5121E	
Wclean+25a			+25	2CJ5121C	
Wclean	7.0	$\alpha =$ 0,10,15,20	0	7CJ5121A	
		Sched F		7CJ5121AR	
Wclean-25a	15	Sched G	-25	15CJ5121B	
Wclean-10a			-10	15CJ5121D	
Wclean		Sched H	0	15CJ5121A	BLC off
			15CJ5121AR		
Wclean+10a		Sched G	+10	15CJ5121E	
Wclean+25a			+25	15CJ5121C	
Wlewise-10a	2.0	Sched I	-10	2CJ5122D	Failure + Roughness
Wlewise		Sched G	0	2CJ5122A	
Wlewise+10a		Sched I	+10	2CJ5122E	
Wlewise	7.0	Sched G	0	7CJ5122A	
Wlewise-10a	15	Sched I	-10	15CJ5122D	
Wlewise		Sched G	0	15CJ5122A	
Wlewise+10a		Sched I	+10	15CJ5122E	
WroughB-10a	2.0	Sched F	-10	2CJ5126D	Roughness B – 80 grit
WroughB			0	2CJ5126A	
WroughB+10a			+10	2C25126E	
WroughB	7.0		0	7CJ5126A	
WroughB-10a	15		-10	15CJ5126D	
WroughB			0	15CJ5126A	
WroughB+10a			+10	15CJ5126E	
WroughC	2.0		0	2CJ5127A	Roughness C – 120 grit
	15			15CJ5127A	
Wrunback-10A	2.0	Sched F	-10	2CJ5124D	Runback
Wrunback			0	2CJ5124A	
Wrunback+10A			+10	2C25124E	
Wrunback	7.0		0	7CJ5124A	
Wrunback-10A	15		-10	15CJ5124D	
Wrunback			0	15CJ5124A	
Wrunback+10A			+10	15CJ5124E	
Wrunback eq1	2.0	Sched J	0	2CJ5128A	3/32" balsa strip at pt. of max height
	15			15CJ5128A	on suction side
Wrunback eq2	2.0			2CJ5129A	1/16" balsa strip at pt. of max height
	15			15CJ5129A	on suction side

Schedule F: -4°, 0°, 4°, 6°, 8°, 10°, 12°, 13, 14°, 15°, 16°, 17°, 18°, 19°, 21°

Schedule G: -4°, 0°, 4°, 6°, 8°, 10°, 12°, 14°, 15°, 16°, 17°, 18°, 19°, 20°, 21°

Schedule H: -4°, 0°, 4°, 6°, 8°, 10°, 12°, 13°, 14°, 15°, 16°, 17°, 18°, 19°, 20°, 21°, 22°

Schedule I: -4°, 0°, 4°, 6°, 8°, 10°, 11°, 12°, 13°, 14°, 15°, 16°, 18°, 20°

Schedule J: -4°, 0°, 4°, 6°, 8°, 10°, 12°, 13°, 14°, 15°, 16°, 17°, 19°, 21°



### **3.1.2. University of Illinois at Urbana-Champaign Wind Tunnel Tests**

The University of Illinois Subsonic Wind Tunnel is an open return wind tunnel that has a 3x4 ft test section and is capable of dynamic pressures up to 50 psf.

The 1/12-scale model tested at UIUC was mounted to a fixture specially made for these tests that connected it to a NASA six-component balance that was used to measure the forces and moments. Unlike the LFSWT tests where the models were mounted under the floor, the 1/12 scale model was mounted so that its root was just above the test section floor and only the spars extended through the floor to mate with the mounting fixture. The span of the smaller scale model was adjusted accordingly so that all tests had the same exposed wing span.

A hinge moment balance was built by Modern Machine to be used for aileron hinge moment measurements. Because of the balance's large size relative to the 1/12-scale model and the aileron hinge line lying at 30% aileron chord, a relatively large portion of the aileron leading edge had to be removed to accommodate the balance and prevent fouling when the aileron was deflected. This proved to be troublesome during the test.

Because of the small size of this model, it was not possible to include the outer two rows of pressure taps since they extended through the aileron. It was felt that there was no way to bridge the hinge without impacting the hinge moment readings. Consequently, only one row of taps was included at the same relative span station as the most inboard position used for the larger scale tests.

#### **3.1.2.1. Ice shapes**

The ice conditions tested in the UIUC wind tunnel were the same as those that had been tested on the larger scale wing panels at the LFSWT. The LFSWT results showed that the failure shape could be scaled by a simple geometric method. However this method could not be applied to the runback shapes due to significant Reynolds number effects. The runback ice condition was therefore simulated by various easy to produce simpler shapes (such as wooden strips and piano wire) in an attempt to identify a shape that would produce an equivalent effect to what had been seen in the large scale tests. Also, various grits were tested as part of the two minute initial (pre-activation) ice accretion tests in order to judge how best to scale the grit to produce results for the 1/12-scale tests that were similar to the larger scale results.

#### **3.1.2.2. Test Program**

The run program that was tested at UIUC is presented in Table 5.

Table 5. - 1/12-Scale Model Runs

Config	qbar	$\delta a$	File Name	Comments
Wclean-25a	3.0	-25	R3A5C046	Clean
Wclean-10a		-10	R3A4C042	
Wclean		0	R3A1C024	
Wclean+10a		+10	R3A2C031	
Wclean+25a		+25	R3A3C033	
Wclean-25a	18.0	-25	R2A5C045	
Wclean-10a		-10	R2A4C041	
Wclean		0	R2A1C026	
Wclean+10a		+10	R2A2C032	
Wclean+25a		+25	R2A3C034	
Wclean	50.0	0	R1A1C027	
Wlewise-25a	3.0	-25	R3A5F062	Failure (no grit)
Wlewise-10a		-10	R3A4F058	
Wlewise		0	R3A1F053	
Wlewise+10a		+10	R3A2F056	
Wlewise+25a		+25	R3A3F060	
Wlewise-25a	18.0	-25	R2A5F063	
Wlewise-10a		-10	R2A4F059	
Wlewise		0	R2A1F054	
Wlewise-10a		+10	R2A2F057	
Wlewise-25a		+25	R2A3F061	
Wlewise	50.0	0	R1A1F055	
Wlewise3	3.0	0	R3A1R151	Failure w/ 220 grit
	18.0		R2A1R152	
	50.0		R1A1R153	
Wlewise equiv	3.0	0	R3A1F049	Failure Equivalent (3/16" rod)
	18.0		R2A1F050	
	50.0		R1A1F052	

Table 5. – Continued.

Config	qbar	$\delta a$	File Name	Comments
Wrough1-10a	3.0	-10	R3A4G071	Roughness 1 – 80 grit
Wrough1		0	R3A1G065	
Wrough1+10a		+10	R3A2G069	
Wrough1-10a	18.0	-10	R2A4G070	
Wrough1		0	R2A1G066	
Wrough1+10a		+10	R2A2G068	
Wrough1	50.0	0	R1A1G067	
Wrough2	3.0	0	R3A1G072	Roughness 2 – 40 grit
	18.0		R2A1G073	
	50.0		R1A1G074	
Wrough3	3.0	0	R3A1G075	Roughness 3 - double Sided tape only
	18.0		R2A1G076	
	50.0		R1A1G077	
Wrough4	3.0	0	R3A1G078	Roughness 4 – 120 grit
	18.0		R2A1G079	
	50.0		R1A1G080	
Wrough5-25a	3.0	-25	R3A5G088	Roughness 5 – 220 grit
Wrough5		0	R3A1G081	
Wrough5+10a		+10	R3A2G084	
Wrough5+25a	18.0	+25	R3A3G086	
Wrough5-25a		-25	R2A5G089	
Wrough5		0	R2A1G082	
Wrough5+10a		+10	R2A2G085	
Wrough5+25a		+25	R2A3G087	
Wrough5	50.0	0	R1A1G083	
Wrunback1	3.0	0	R3A1R093	1/8" sq. on lower surface only
	18.0		R2A1R094	
	50.0		R1A1R095	
Wrunback2	3.0	0	R3A1R096	3/32" sq. on lower surface only
	18.0		R3A1R097	
	50.0		R3A1R098	
Wrunback3	3.0	0	R3A1R099	0.3" X 0.05" thick double sided tape at l.e. of runback line, 3/32" sq. l.s.
	18.0		R2A1R100	
	50.0		R1A1R104	
Wrunback4	3.0	0	R3A1R101	Added 80-grit to Runback3
	18.0		R2A1R102	
	50.0		R1A1R103	
Wrunback5	3.0	0	R3A1R105	1/16" square on upper at runback line, 3/32" square on lower surface
	18.0		R2A1R106	
	50.0		R1A1R107	
Wrunback6	3.0	0	R3A1R108	24-grit on 1/2" wide double sided tape at runback line, 3/32" square on lower surface
	18.0		R2A1R109	
	50.0		R1A1R110	
Wrunback7	3.0	0	R3A1R111	16-grit on 1/2" wide double sided tape at runback line, 3/32" square on lower surface
	18.0		R2A1R112	
	50.0		R1A1R113	
Wrunback8	3.0	0	R3A1R114	u.s 1/16" sq., (tip 0.14", root 0.3". dwnstrm of LEWICE line), 3/32" on l.s
	18.0		R2A1R115	

Table 5. – Concluded.

Config	qbar	$\delta a$	File Name	Comments
Wrunback9	3.0	0	R3A1R116	1/16" square on u.s., (at LEWICE line), 3/32" on l.s.
	18.0		R2A1R117	
	50.0		R1A1R118	
Wrunback10	3.0	0	R3A1R119	1/16" square on u.s., (tip 1/16" and root 5/32" downstream of LEWICE line), 3/32" on l.s.
	18.0		R2A1R120	
	50.0		R1A1R121	
Wrunback11	3.0	0	R3A1R122	1/16" square on u.s., (tip 1/32" and root 5/64" downstream of LEWICE line), 3/32" on l.s.
	18.0		R2A1R123	
	50.0		R1A1R124	
Wrunback12	3.0	0	R3A1R125	1/16" piano wire u.s., (tip 1/32" and root 5/64" dwnstrm LEWICE line), 3/32" on l.s.
	18.0		R2A1R126	
Wrunback13	3.0	0	R3A1R127	0.025" piano wire on u.s., (tip 1/32" and root 5/64" downstream of LEWICE line), 3/32" on l.s.
	18.0		R2A1R128	
Wrunback14	3.0	0	R3A1R129	0.025" piano wire on u.s., (tip 1/16" and root 5/32" downstream of LEWICE line), 3/32" on l.s.
	18.0		R2A1R130	
Wrunback15	3.0	0	R3A1R131	0.025" piano wire on u.s., (tip 0.14" and root 0.3" downstream of LEWICE line), 3/32" on l.s.
	18.0		R2A1R132	
Wrunback16	3.0	0	R3A1R133	0.025" piano wire on u.s. at LEWICE line, 3/32" on l.s.
	18.0		R2A1R134	
Wrunback17	3.0	0	R3A1R135	0.032" piano wire on u.s. at runback line, 3/32" square on l.s.
	18.0		R2A1R136	
Wrunback18	3.0	0	R3A1R137	0.047" piano wire u.s. (at runback line), 3/32" square on l.s.
	18.0		R2A1R138	
Wrunback19	3.0	0	R3A1R140	0.047" piano wire u.s. (0.14" tip and 0.3" root downstream of runback line), 3/32" square on l.s.
	18.0		R2A1R139	
Wrunback20	3.0	0	R3A1R141	1/16" piano wire u.s. (0.14" tip, 0.3" rt dwnstrm runback line), 3/32" sq l.s.
Wrunback21-25a	3.0	-25	R3A5R148	0.032" piano wire u.s. (0.14" tip and 0.3" root downstream of runback line), 3/32" square on l.s.
	18.0		R2A5R149	
Wrunback21	3.0	0	R3A1R142	
	18.0		R2A1R144	
	50.0		R1A1R145	
Wrunback21+25a	3.0	+25	R3A3R146	
	18.0		R3A3R147	
Wrunback21A	3.0	0	R3A1R143	scotch tape over runback 21 shape
Wgurney1+10a	3.0	+10	R3A2R160	Gurney flap - 1/16" square balsa
Wgurney1+25a		+25	R3A3R159	(aileron taped over balance)
Wgurney2+10a	3.0	+10	R3A2R161	0.025" piano wire Gurney flap

### 3.1.3. Results

In general, the following brief observations can be made:

- The icing conditions all reduced the maximum lift and lowered the stall angle, as shown in Figure 6 for the full-scale wing.
- In addition, as was expected, the maximum lift and stall angles were also a function of Reynolds number and scale, as shown in Figure 7.
- While it was possible in some cases to have equivalent low Re iced configurations that approached the lift characteristics of the high Re test, the clean airplane characteristics at low Re were significantly different than those at high Re making modeling of incremental ice effects based solely on low Re test data challenging.

Early in the test of the 5/12-scale wing at the LFSWT, it was noticed that the hinge moment characteristics of this model did not match the characteristics of the full-scale aileron hinge moments. A check of the instrumentation and calibrations found nothing obviously wrong. Inspection of the model and comparison to the full-scale wing showed that the leading edge shape of the model aileron was significantly different from that of the full-scale. It was determined that the drawings used for model construction had the incorrect aileron leading-edge shape and that this would account for the difference in measured hinge moments. Because the remaining available test time was short, it was decided to continue the test with the model as it was and to forgo hinge moment comparisons.

Hinge moment measurements during the UIUC tests of the 1/12-scale model also proved to be troublesome. The hinge moment balance constructed for these tests based its load limits on the hinge moment coefficients measured during the full-scale tests in the LFSWT. Once the testing began at UIUC, it became evident that the hinge moments being measured there did not agree very well with the previous LFSWT results and became significantly larger at stall angles of attack. Since there was no other way to support and set the ailerons than through the hinge moment balance, it was decided to not test aileron deflections at the highest dynamic pressure and in some cases to limit the angles of attack being tested in order to minimize overloading the hinge moment balance. Despite these precautions, the balance was evidently damaged at some point during the tests, as readings for the configurations tested in the later part of the entry are nonsensical.

A significant number of runs during the latter part of the UIUC tests were involved in evaluating equivalent ice shapes that would produce similar aerodynamic effects as the actual ice shapes at the low geometric scale and Reynolds number of the up-coming complete airplane tests. These results were analyzed during the period between the completion of the wing panel tests and the beginning of the complete airplane tests, and equivalent ice shapes were chosen for the runback condition and non-geometrically scaled grit was selected for the complete airplane tests.

- The 22.5-minute failure shape could be scaled from full scale to 1/12 scale through simple geometric scaling. Nearly identical lift curves were maintained (with the geometrically scaled ice shape) as the full scale model was reduced to 1/12-scale model and the Reynolds number reduced from 4.1 million to 0.15 million. Similar results were observed for the pitching moment.
- The 2-minute roughness shape exhibited slightly more Reynolds number sensitivity than the failure shape. However, similar lift and pitching moment curves could be maintained (as the model chord and Reynolds number is decreased) by choosing an appropriate grit height for each model.
- The runback shape exhibited even more Reynolds number dependence. Geometrically scaled runback shapes produced different lift curves on the full-scale and 5/12-scale models, even at matched Reynolds number. However, on the same model, there was little variation in the lift curve with Reynolds number. To obtain a comparable lift curve on the 5/12-scale model, a square cross-section wooden strip equivalent geometry was required. A comparable lift curve could not be obtained with the 1/12-scale model because the clean model had lower  $C_{Lmax}$  than the iced full-scale model. Because of this, an equivalent ice shape that resulted in similar relative reduction in  $C_{Lmax}$  and stall angle of attack (when compared to the clean model at same Reynolds number) was found.

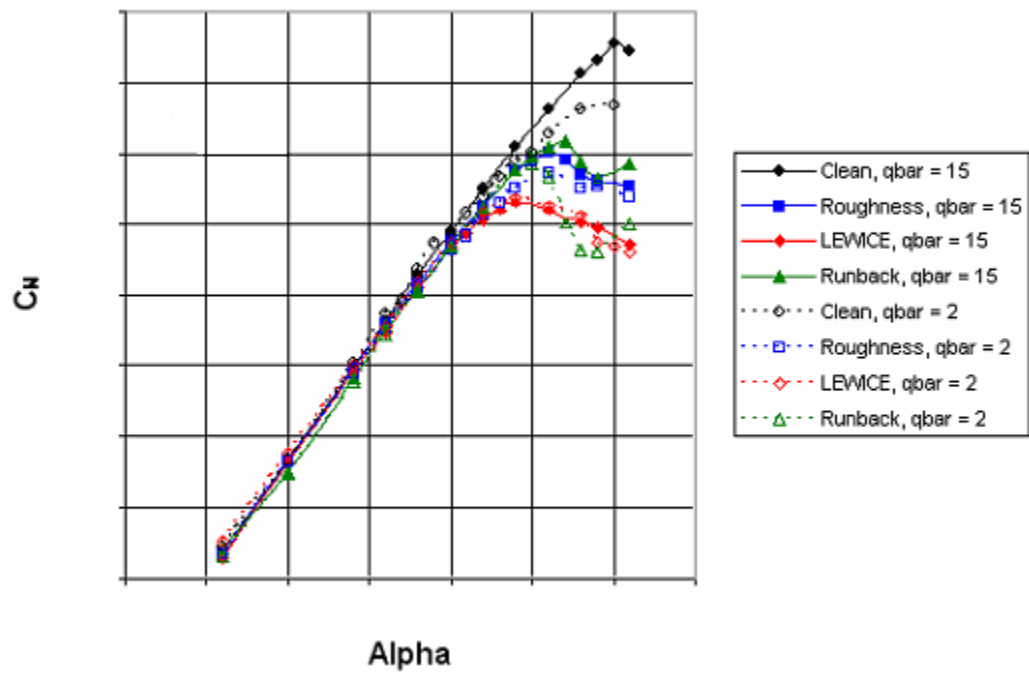


Figure 6. – Comparison of normal force coefficients from LFSWT tests of full-scale wing panel with different icing conditions.

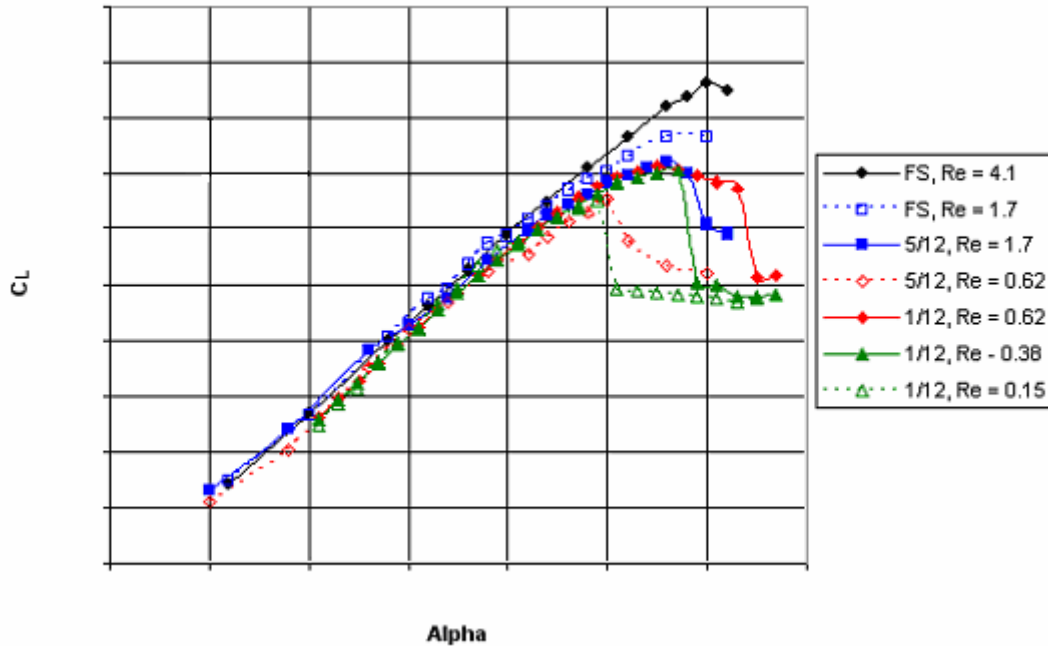


Figure 7. – Effect of scale and Reynolds number on maximum lift and stall characteristics of the clean wing panel.

### **3.2. Complete Airplane Model Tests**

After the wing panel tests were completed and the scaling effects were analyzed, static, rotary-balance and forced-oscillation test data were measured for a complete model of the business jet aircraft using a 1/12-scale model mounted on the aerodynamic test rig in the Bihle Applied Research Aeronautische Forschung, GmbH Large-Amplitude Multiple Purpose (LAMP) wind tunnel, located in Neuburg a.d. Donau, Germany.

Data were typically measured through an angle-of-attack range of  $0^\circ$  to  $50^\circ$ , with a limited amount of data measured at inverted angles of attack between  $-20^\circ$  and  $0^\circ$ . Static tests were performed with the rotary rig stationary, while rotary-balance tests were performed with the model undergoing steady rotations (both clockwise and counter-clockwise) about the velocity vector. Forced-oscillation tests were performed for individual body-axis pitch, roll and yaw oscillations at selected rates. This data set was subsequently used as the primary basis for developing a new clean, un-iced aircraft simulation, as well as for developing the models for the iced conditions.

#### **3.2.1. Model**

The model tested was a 1/12-scale representation of the business jet. The model had been previously constructed by Bihle Applied Research for configuration studies during the development phase of the aircraft. A photograph of the model on the LAMP test rig is presented in Figure 8. The following movable surfaces could be set to any specified deflection within the following limits and sign convention:

Aileron	$-25^\circ$ TE Up, $+20^\circ$ TE Down
Elevator	$-20^\circ$ TE Up, $+15^\circ$ TE Down
Rudder	$-35^\circ$ TE Right (viewed from aft), $+35^\circ$ TE Left
Flaps	$0^\circ$ , $+40^\circ$ TE Down

In addition to the basic (un-iced) airplane, data were collected during this test for the same three iced conditions considered in the wing tests. These were:

- Wing Ice protection system failure
- Pre-Activation (Roughness) Ice
- Wing Run-back ice



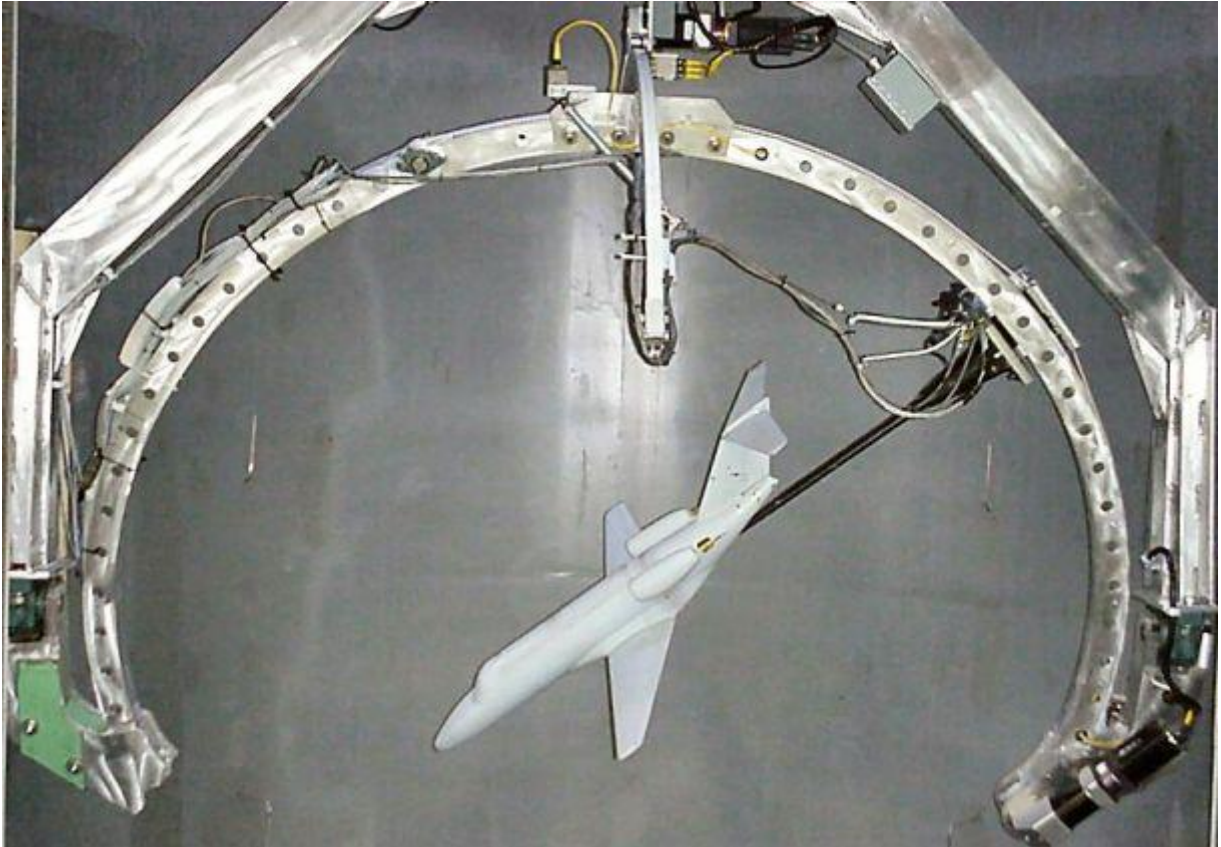


Figure 8. - 1/12-scale business jet model mounted on the test rig in the LAMP wind tunnel.

The wing ice protection system failure condition consisted of:

- LEWICE predicted 22.5 minute ice shapes on the normally protected wing leading-edge areas (Figure 9.)
- 45 minute LEWICE predicted shapes on the unprotected wing tips (Figure 9.)
- 40 grit silicon carbide on the protected leading edge of the horizontal tail
- 45 minute LEWICE predicted shapes on the unprotected portions of the horizontal tail (small areas at the root and tip – Figure 10.)
- 45 minute LEWICE predicted shapes on the leading edge of the vertical tail, which is not ice protected (Figure 11.)

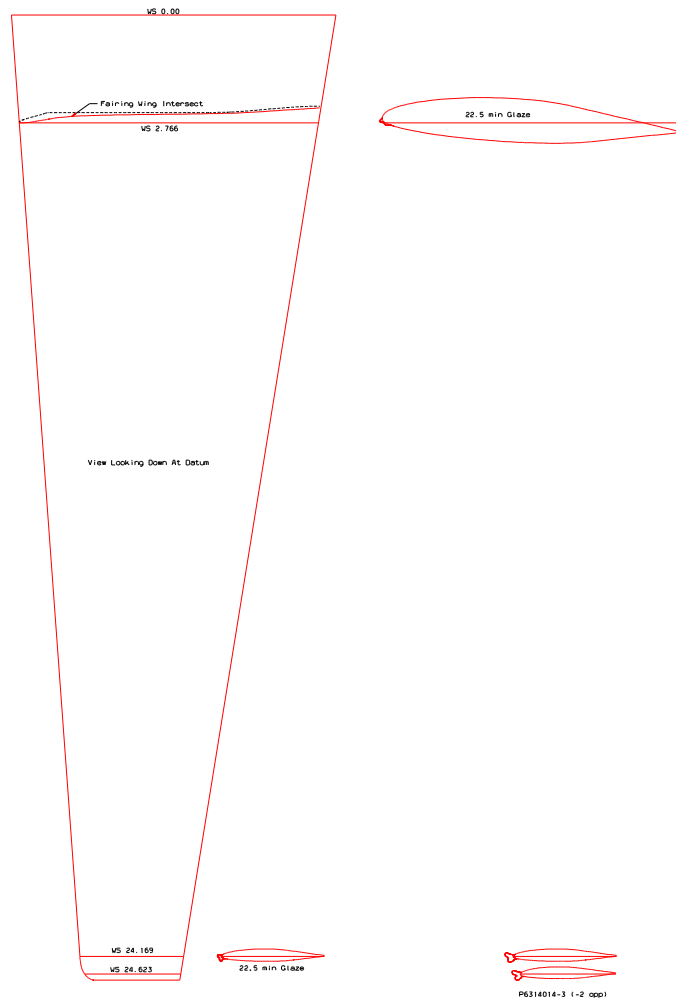


Figure 9. - Wing Icing Protection System Failure Ice shapes predicted using LEWICE

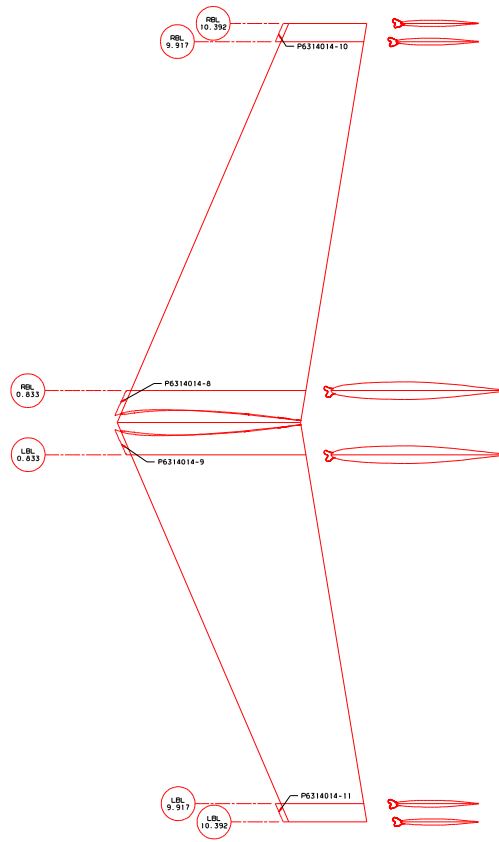


Figure 10. – Horizontal tail Ice shapes for the unprotected areas at the root and tip. 40-grit silicon carbide was attached on the protected areas to represent inter-cycle ice accumulations.

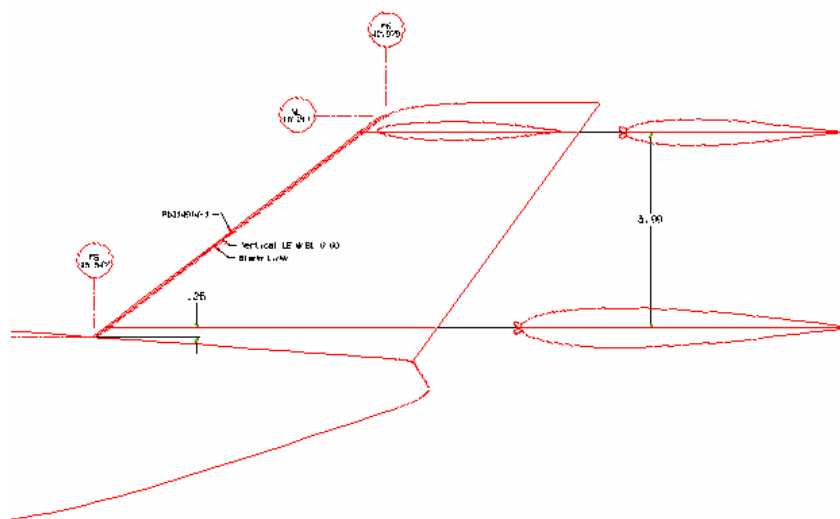


Figure 11. – LEWICE predicted ice shape for the unprotected vertical tail.

The ice shapes were produced by stereo lithographic techniques and attached to the appropriate surfaces with double-sided tape. The silicon carbide 40-grit, the grit size chosen based on the wing panel tests done at the UIUC wind tunnel, was also attached using double-sided tape. A photograph of the ice shapes on the wing is presented in Figure 12 and those on the tail surfaces are shown in Figure 13.

The *pre-activation ice* condition consisted of 40 grit silicon carbide attached to the entire wing leading edge and all tail surface leading edges independent of whether or not they were protected. The percent of the surface chord where the grit was attached was the same as would have been covered by the LEWICE shapes used for the icing system failure condition. A photograph of the 1/12-scale model with the grit attached is shown in Figure 14.

The *wing runback ice* condition represents a condition where the wing icing protection system is working and melts the ice that forms on the wing leading edge. The water then flows farther back on the wing and re-freezes behind the heated leading edge. The actual ice shapes used to represent the runback condition are shown in Figure 15 mounted on a partial wing model tested in the LFSWT. They consist of a region of ice accumulation on the upper surface and a blunt ridge of ice on the lower surface, both behind the heated ice protection system leading edge region.



Figure 12. – Icing Protection System Failure Ice shapes on the 1/12-scale model wing.

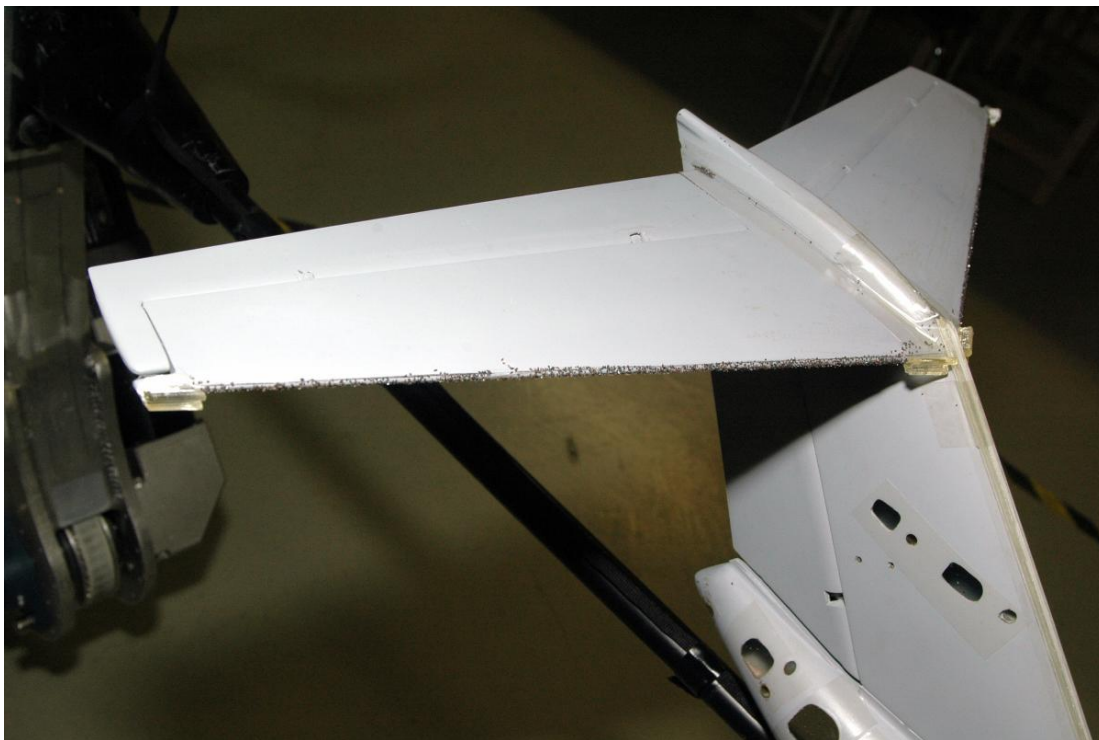


Figure 13. – Tail surface Ice shapes tested on the 1/12-scale model.



Figure 14. – Pre-Activation Ice representation on 1/12-scale model.

The tests in the LAMP facility used equivalent ice shapes for the upper and lower wing surfaces that were previously tested on a 1/12-scale wing panel in the University of Illinois at Urbana-Champaign (UIUC) wind tunnel. During the UIUC tests, this equivalent ice shape produced wing lift characteristics at low Reynolds numbers (similar to those of the LAMP test) that reproduced the relative effects seen at higher Reynolds numbers for the actual ice shapes on a full-scale wing panel in the Langley Full-Scale Wind Tunnel. The equivalent shape consisted of 0.025" piano wire attached to the wing upper surface and a 3/32" square wooden strip attached to the lower surface. These were attached at the same relative chord position as tested at the UIUC wind tunnel. A photograph of the equivalent ice shape is shown in Figure 16.

The 45 minute ice shapes that were tested for the wing icing protection system failure condition were also used for the runback ice case at the unprotected areas with the pre-activation grit on the protected portions of the horizontal tail. Consequently, the only difference between the runback case and the wing icing protection failure case was that the 22.5 minute LEWICE shape was removed from the wing and replaced with the equivalent runback shapes.

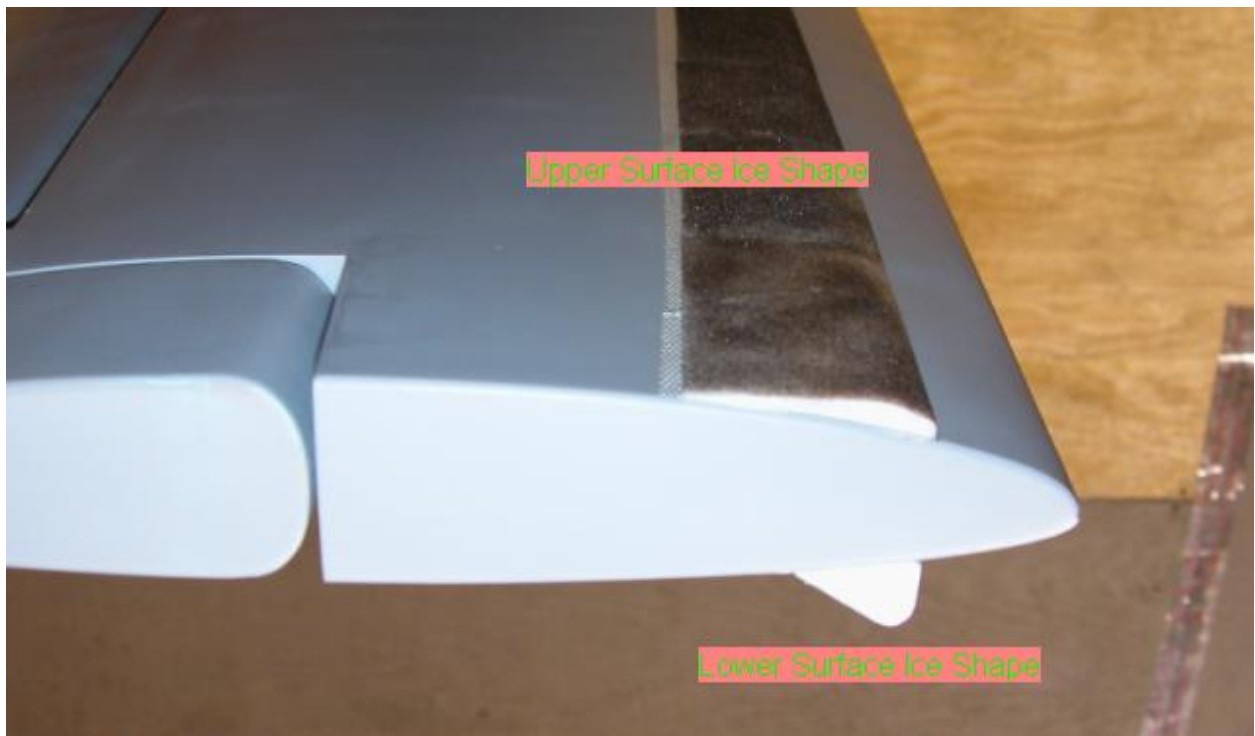


Figure 15. – Runback ice shapes tested a LFSWT on partial wing panel.



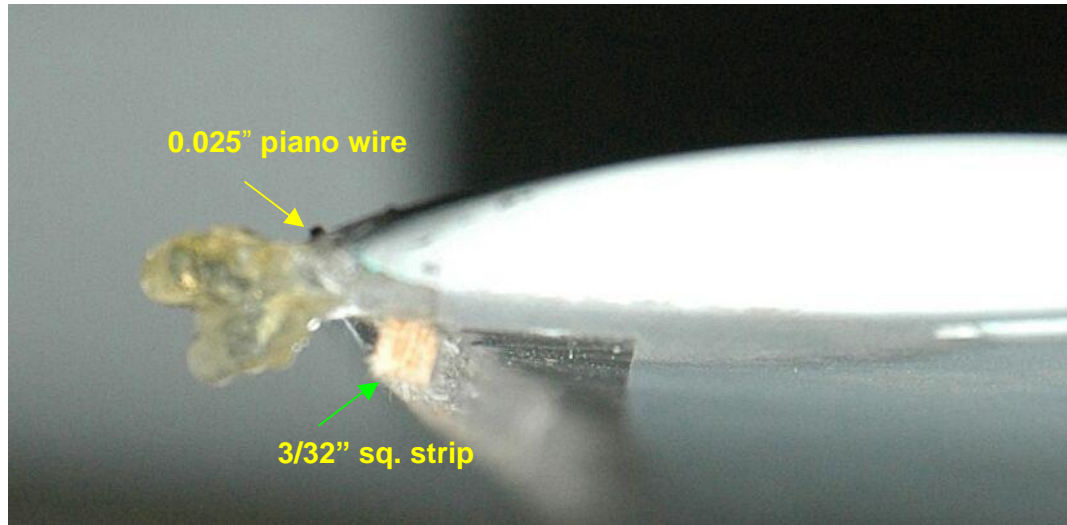


Figure 16. – Equivalent Runback Ice Shape tested during LAMP test.

### 3.2.2. Test Facility

The test program was conducted in the Bihle Applied Research Aeronautische Forschung, GmbH Large-Amplitude Multiple Purpose (LAMP) Wind Tunnel Facility located in Neuburg a.d. Donau, Germany in August-September 2004.

The LAMP test rig features a C-sector sting support system that provides the capability for continuous angle-of-attack sweeps of  $0^\circ$  to  $+90^\circ$  and the entire C-sector can be tilted for continuous sideslip angle sweeps to  $\pm 30^\circ$ . Oscillatory stings, capable of sinusoidal motions at selected amplitudes and frequencies, also attach to the test rig to measure body-axis pitch, roll, and yaw forced oscillation dynamic characteristics.

The same angle-of-attack and sideslip ranges are available during steady rotation rates of up to 70 revolutions per minute in either direction. The range of  $\Omega b/2V$  values are again obtained by adjusting rotational speed and/or tunnel air flow velocity. (Static aerodynamic forces and moments are obtained when  $\Omega=0$ .) In addition, forced oscillation tests can be performed with the rig rotating, for unique combined motion testing.

Model installation and configuration modifications are conveniently performed in the area outside the tunnel section, since the entire rig, including the model, can be quickly moved in and out of the tunnel on a motorized traveling beam.

A six-component strain gauge balance, affixed to the end of the sting and mounted inside the model, is used to measure the six forces and moments acting along and about the model body axis. A control panel located outside of the tunnel test section is used to activate motors on the rig, which position the model

to the desired attitude. Electrical currents from the balance and to the motors on the rig are conducted through slip rings.

The data acquisition, reduction, and presentation system is composed of a NEFF System 470 16-channel scanner/voltmeter, a personal computer running HTBasic, with a CRT display, and printer. This equipment permits data to be presented via on-line digital printouts and/or graphical plots. Tunnel operation, data acquisition/reduction, and plotting are totally automated.

### **3.2.3. Test Procedures**

Tare (wind-off) data are acquired prior to any wind-on tests. These give the forces and moments acting on the model due to its weight at each attitude. These data are then stored for future use. After the tares are completed, the model is tested with the wind on. In this phase, the tunnel airspeed is set to the proper value and the model is set to the desired attitude. The total forces and moments are then measured with the data acquisition system. The tare values are subtracted and the remaining aerodynamic values are nondimensionalized to coefficient form. Set up for the next run, including any model changes are then performed and the process repeated.

For rotary testing, it is necessary to measure the tares for the rotating model since the inertial tare values will vary with rotation rate. In order to minimize the resistance from moving the model through the still air, tares are measured with the model surrounded by a sealed structure (tare bag) that traps a volume of air around the model and moves with it when it is rotated. Tares for a rotating model will vary as the square of rotation rate, so tares for rotary testing are taken for a series of rotation rates, for both clockwise and counter-clockwise rotations, and a least-squares linear curve is fitted through the data at each angle of attack and sideslip. The slope and intercept of these tare data are then used to calculate the tare to be subtracted for any rotation rate tested.

For forced oscillation testing, tare data must be measured for each oscillation frequency (and amplitude) to be tested, as well as for each angle of attack and sideslip. The oscillations for the tare data and for the air-on data must be properly synchronized for the data reduction of these data.

### **3.2.4. Test Conditions**

The test matrix for the business jet model entry is presented in Table 6 at the end of this report. The run program for this set of tests was designed to provide the effects of angles of attack and sideslip, control deflections (elevator, aileron, rudder and flaps), and icing conditions on the static and rotary aerodynamic characteristics and on the forced oscillation data for oscillations about each of the body axes. Nominally, data were measured through an angle-of-attack range of  $0^\circ$  to  $+50^\circ$  in ascending order unless otherwise indicated by the angle-of-attack schedules shown in Table 6. Tests were conducted in the Bihle Applied Research LAMP 10-Foot Vertical Tunnel Facility at a dynamic pressure of  $2.0 \text{ lb/ft}^2$ , an approximate airstream velocity of  $41 \text{ ft/sec}$ , corresponding to a Reynolds number of approximately 122,000, based on the



model wing mean aerodynamic chord. All configurations were tested with an aft sting, except for the pitch and yaw forced oscillation data, which required using a top sting. The balance moment reference center was located at the 25% chord location.

An initial set of tests were run to look at the effect of dynamic pressure on the wind tunnel data. Static data were run at  $q_{bar} = 1.0, 1.5, 2.0$ , and  $3.0 \text{ lbs/ft}^2$  (Figure 17). Because there was essentially no difference between the 2.0 and 3.0 data, it was decided to run all of the data at 2.0 because the rotation rates and oscillatory frequencies at that speed were reasonably within the LAMP facility's capability. Consequently, all of the test results for LAMP were run at  $q_{bar} = 2.0 \text{ lbs/ft}^2$ . The previous low speed tests conducted at the UIUC tunnel were all run at  $q_{bar} = 3.0 \text{ lbs/ft}^2$ .

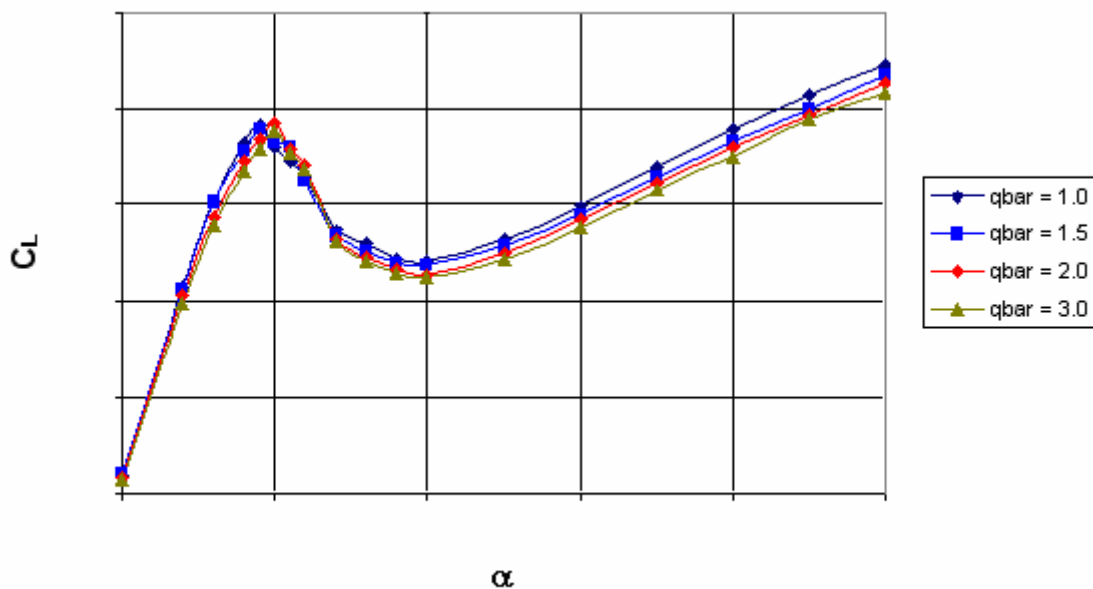


Figure 17. – Influence of dynamic pressure on static lift coefficient measured in the LAMP wind tunnel.

### 3.2.5. Data Acquisition and Reduction

The LAMP force and moment measurement data acquisition system is comprised of the following:

- A six-component internal strain-gauge balance manufactured by Modern Machine & Tool Company of Newport News, VA. The range and typical operating accuracy of the SPT-989 balance are listed below:

Channel	Range	Typical Accuracy
Normal	20 lbs	$\pm 0.02$ lbs
Axial	20 lbs	$\pm 0.02$ lbs
Pitch	400 in-lbs	$\pm 0.40$ lbs
Roll	80 in-lbs	$\pm 0.10$ lbs
Yaw	200 in-lbs	$\pm 0.20$ lbs
Side	15 lbs	$\pm 0.015$ lbs

- A NEFF System 470
- A Data Acquisition Computer and Printer

The strain gauge balance was powered by 5VDC. The output of the balance is approximately 5mVDC at the full-scale load. The NEFF System 470 provides data conditioning/multiplexing for the analog balance signals, converting them to digital signals for the digital computer. This includes filtering and amplification of the analog signal. The NEFF 470 is connected to the computer by an IEEE-488 (GPIB) Interface.

In the data acquisition computer, the balance voltages (converted from analog to digital signals by the Neff System 470) were converted to forces and moments, the balance interactions applied, tares removed, and the resulting coefficient data calculated using the model geometry and dynamic pressure reading.

### 3.2.6. Data Presentation

Conventional static data, measured on the rotary balance when the rotation rate is zero, are presented by plotting the aerodynamic coefficients versus angle of attack or angle of sideslip for the respective sweep runs. For inverted testing, the sign convention that positive sideslip signifies nose left to the pilot is maintained. This convention dictates that static lateral stability (the return of the aircraft to a horizontal wings level position) for the inverted aircraft will be of opposite sign to that seen upright, while static directional stability will be the same sign as that observed upright. Therefore, the aircraft possesses lateral stability when producing negative rolling moment for positive sideslip angle at upright angles of attack and producing positive rolling moments for positive sideslip angle at inverted angles of attack. Directional stability exists for the aircraft when producing positive yawing moment for positive sideslip angle at both upright and inverted angles of attack.

Rotary balance data are presented by plotting the aerodynamic coefficients versus the non-dimensional rotation rate,  $\Omega b/2V$ . It is common practice to use a reference non-dimensional rotation rate expressed in terms of the angular velocity,  $\Omega$ , the free-stream velocity,  $V$ , and a reference length which

is usually taken to be half the wingspan,  $b/2$ . With this convention, the ratio of the velocity at the wing tip to the free-stream velocity is  $(\Omega b/2)/V$  or  $\Omega b/2V$ . This ratio is also equal to the arctangent of the helix angle at the wing tip when the airplane is in an equilibrium steady spin. The rotary balance data plots are divided into four quadrants by the coordinate axes. Static data points occur on the ordinate axis ( $\Omega b/2V=0$ ). All points to the right of the ordinate axis represent data measured for positive rotation rates (nose moving to the right). Conversely, all data to the left of the ordinate axis represent negative rotation rates.

Rotary balance testing measures moments generated by the aircraft when subjected to rotation about the velocity vector, and thus the potential propelling or damping characteristics of the aircraft. Propelling moments indicate the possibility for departure from controlled flight and for entering a developed spin. For clockwise rotation during upright testing, a positive rolling or yawing moment is propelling, since it will increase the rotation rate, whereas a negative moment will decrease the rotation rate and is, therefore, a damping moment. Conversely, for a counter-clockwise rotation, negative moments are propelling and positive moments are damping. Rotationally, positive  $\Omega b/2V$  signifies clockwise rotation of the aircraft to the outside observer. This perspective dictates that damped yawing moments for the inverted aircraft will be of opposite sign to that seen in the upright case, while damped rolling moments are the same sign whether upright or inverted.

Body-axis dynamic damping data, representing a specific point and not a linearized derivative, are plotted in a format similar to rotary balance damping data. At a given angle of attack, the measured pitching, rolling or yawing moment is plotted against the body-axis rate term of  $q\bar{c}/2V$ ,  $p b/2V$  or  $r b/2V$ . Traditional static values are plotted when the body-axis rate is zero. As with rotary balance data, the plots are broken into four quadrants each representing damping or propelling characteristics. A negative pitching, rolling or yawing moment produced by positive body axis pitch, roll or yaw rates, respectively, is considered damped for it tends to resist the motion. Conversely, positive pitching, rolling or yawing moments produced by positive pitch, roll or yaw rates, respectively, increase the rate and are therefore considered propelling. This plotting style makes it easier to observe the characteristics at specific body-axis rates and eliminates the ambiguity associated with a particular rate-based dynamic derivative and gives a better understanding as to where a particular damping value is valid. Additionally, due to the highly coupled nature of the aerodynamic properties between the lateral and directional axes, the excitation of either body-axis roll or yaw rate generally yields changes in both rolling and yawing moments. These cross coupling effects, yawing moment due to roll rate and rolling moment due to yaw rate, are considered favorable or proverse if the resulting moment tends to induce coordination (positive yawing moment vs.  $p b/2V$  slope and positive rolling moment vs.  $r b/2V$  slope for positive angles of attack and negatively sloped at inverted angles of attack). Conversely, these cross coupling effects are considered adverse if the moments tend to drive the vehicle to a further uncoordinated state.

### 3.2.7. LAMP Data Discussion

#### 3.2.7.1. Baseline Un-iced Data

Figure 18 through Figure 20 present the comparison of the un-iced airplane static lift coefficients measured at LAMP with those provided by the manufacturer (based on their low-speed wind tunnel data at  $q_{bar} = 80 \text{ lbs/ft}^2$  adjusted to flight determined  $C_{Lmax}$ ) for neutral flaps and for flaps deflected. The lift characteristics measured in the LAMP wind tunnel are consistent with what would be expected at low Reynolds numbers but, as shown, when shifted up to the  $C_{Lmax}$  from flight, provides a good representation of the full-scale lift curve. For the simulation modeling, all of the other static and dynamic data would have to be similarly shifted to the flight stall angle of attack. The LAMP data flap effectiveness matches the manufacturer's simulation data very well.

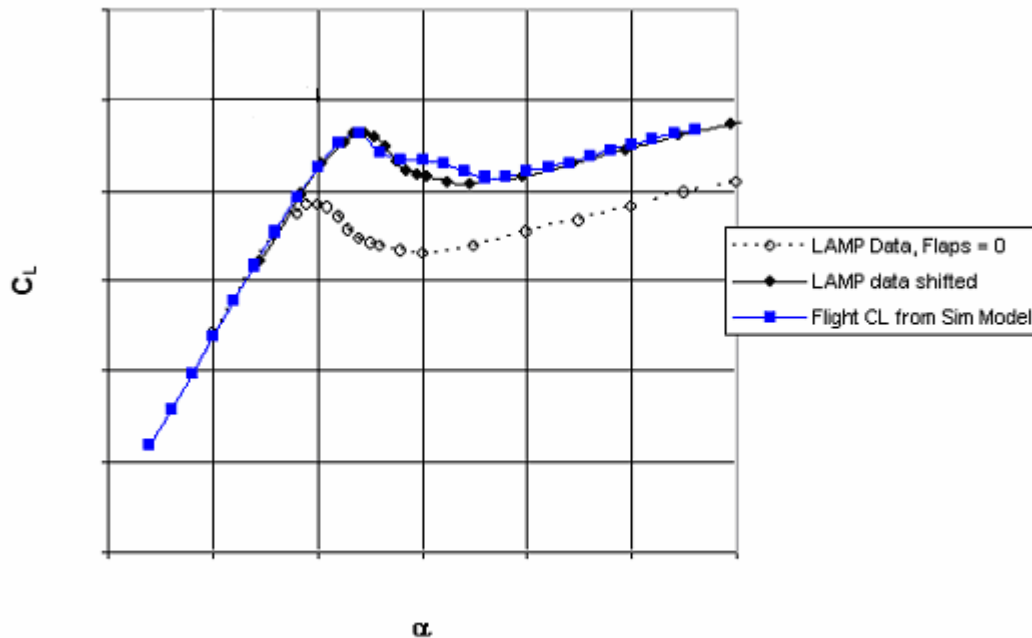


Figure 18. – Comparison of 1/12-scale business jet model lift coefficient at flaps = 0 measured in the LAMP wind tunnel with flight lift coefficient represented by the manufacturer's simulation model shifted to flight  $C_{Lmax}$

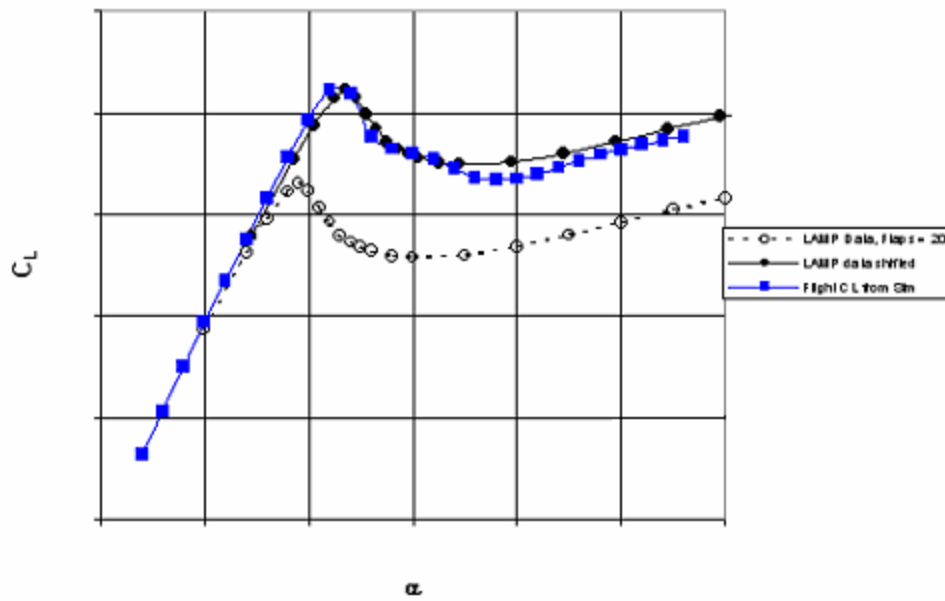


Figure 19. – Comparison of 1/12-scale business jet model lift coefficient at flaps = 20 measured in the LAMP wind tunnel with flight lift coefficient represented by the manufacturer's simulation model shifted to flight

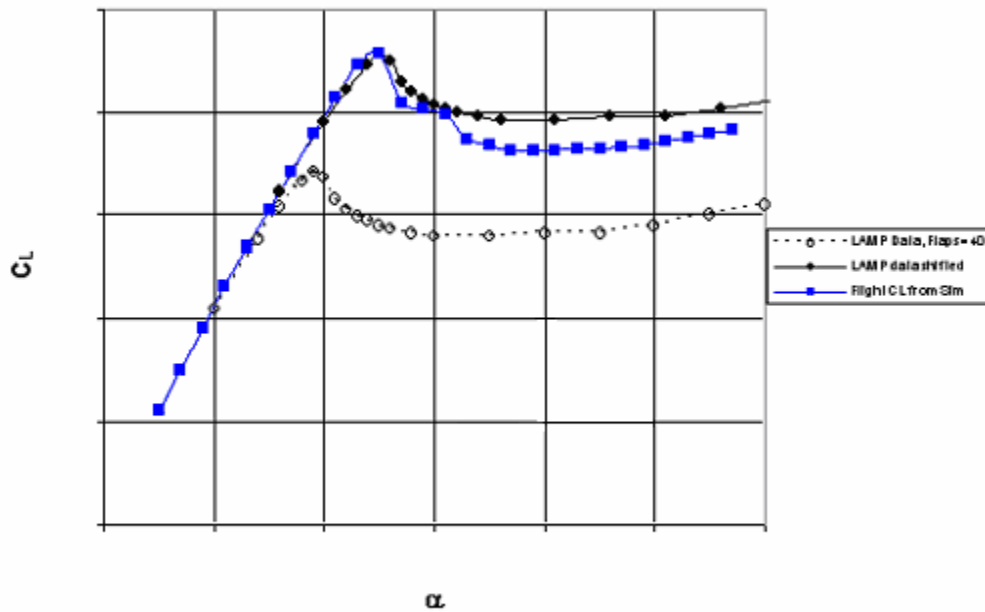


Figure 20. – Comparison of 1/12-scale business jet model lift coefficient at flaps = 40 measured in the LAMP wind tunnel with flight lift coefficient represented by the manufacturer's simulation model shifted to flight  $C_{L_{max}}$

The static pitching moment for neutral flaps is shown in Figure 21. As with the lift coefficient, shifting the LAMP data to agree with the full-scale stall provides good agreement with the manufacturer's simulation data in the unstalled and stalled region. At very high angles of attack, however, the LAMP data are less nose down than the manufacturer's data. This difference will need to be evaluated for the aerodynamic math modeling, but its significance is low, because the difference occurs at much higher angles of attack than are likely to be of importance for the icing study.

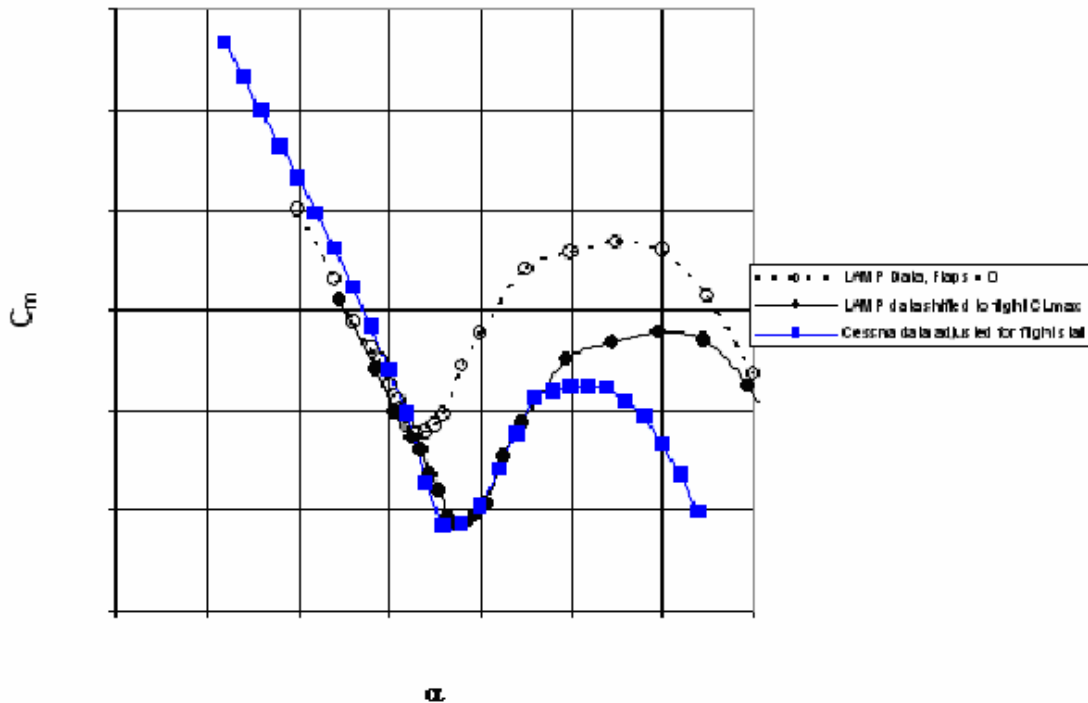


Figure 21. – Comparison of 1/12-scale business jet model pitching moment coefficient at flaps = 0 measured in the LAMP wind tunnel with flight lift coefficient represented by the manufacturer's simulation model shifted to flight stall angle.

Figure 22 presents the pitching moment curves for neutral, full trailing-edge up and full trailing-edge down elevator deflections as measured for the 1/12-scale model compared to the manufacturer's math model data for the full-scale airplane. It can be seen that for trailing-edge down elevator deflection, the 1/12-scale data shows slightly less elevator effectiveness than the full-scale airplane data, while for trailing-edge up deflection, it is significantly less for full deflections. It is unclear whether this was the result of Re effect, or if it resulted from an interference effect due to the proximity of the sector behind the tail, but the data was adjusted when the math model was developed.

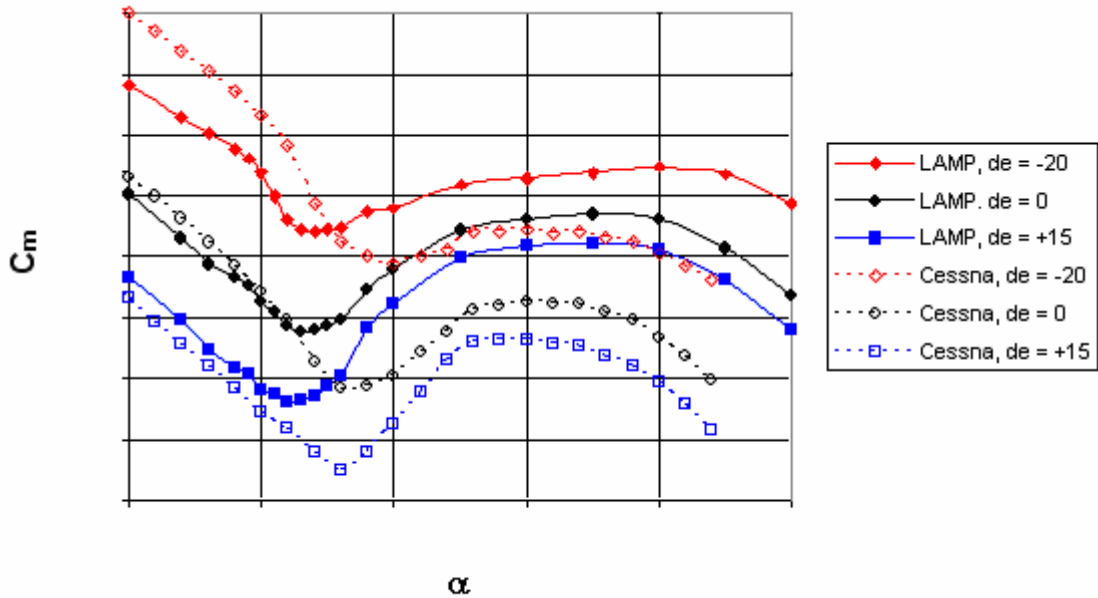


Figure 22. - Comparison of pitching moment data as a function of angle of attack and elevator deflection for the 1/12-scale model tested at LAMP with the manufacturer's simulation data base,  $\beta = 0$ , flaps = 0.

### 3.2.7.2. Effect of Ice Conditions

The LAMP data comparing the failure ice condition with the un-iced model are presented in Figure 23. The initial stall angle of attack is not greatly changed at this  $Re$ , but the immediate post-stall lift characteristics are. The effects of the same ice condition on the wing panel tests for the full-scale wing panel and for the 1/12-scale panel are shown in Figure 24. As can be seen in this figure there is a significant effect of  $Re$  on the un-iced wing that greatly influences the stall angle of attack and the maximum lift coefficient. However, there is only a relatively small influence on the lift characteristics when the failure ice shapes are added. This is most likely the result of the separation point being fixed by the location of the upper horn on the ice shape regardless of  $Re$ . To model the full-scale airplane, the un-iced lift was adjusted, as discussed in the previous section, however, relatively little adjustment was needed to be made to the failure ice lift data.

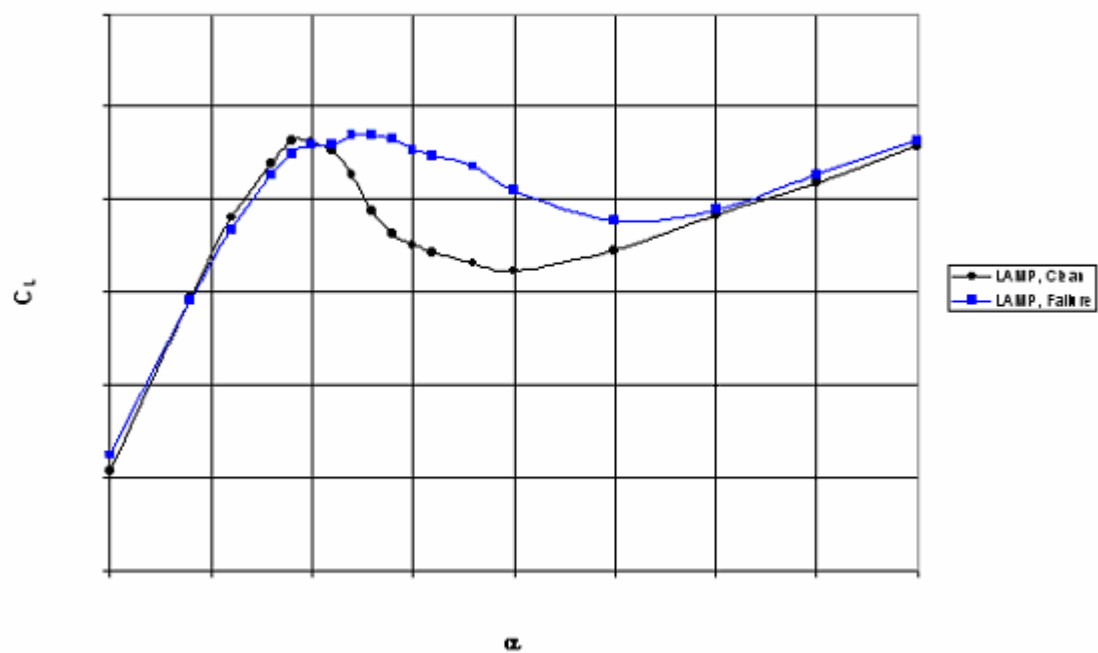


Figure 23. – Effect of failure ice condition on lift coefficient of 1/12-scale model in the LAMP wind tunnel.



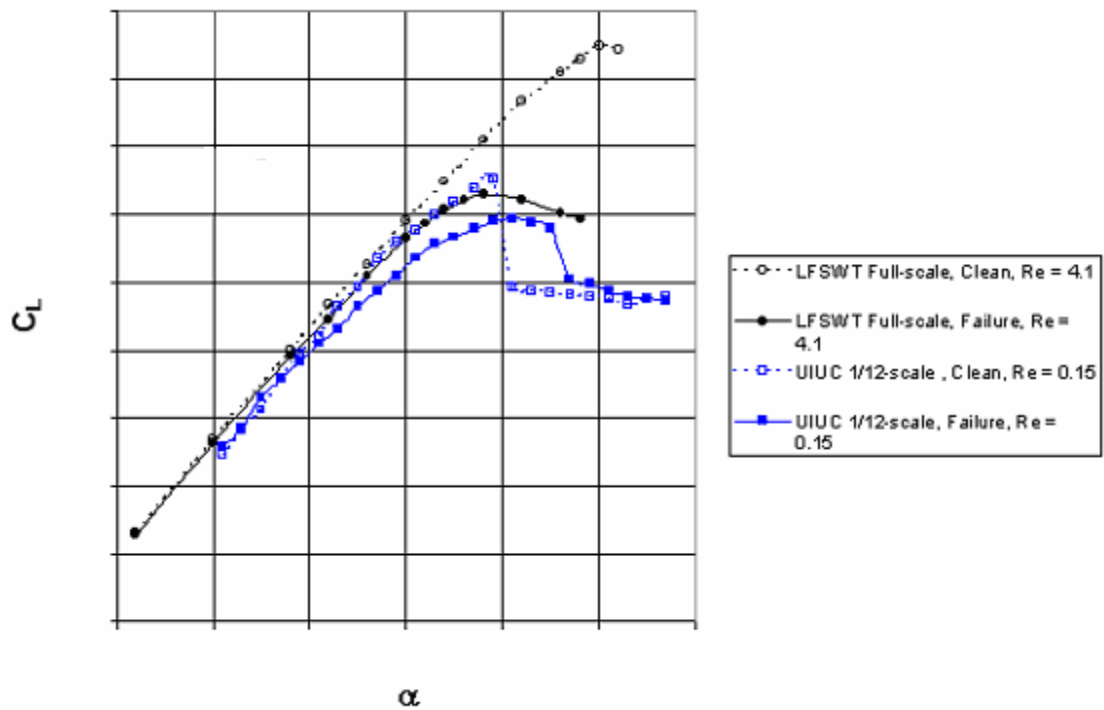


Figure 24. – Comparison of lift coefficients for clean wing and failure ice for wing panel tests at high and low  $Re$ .

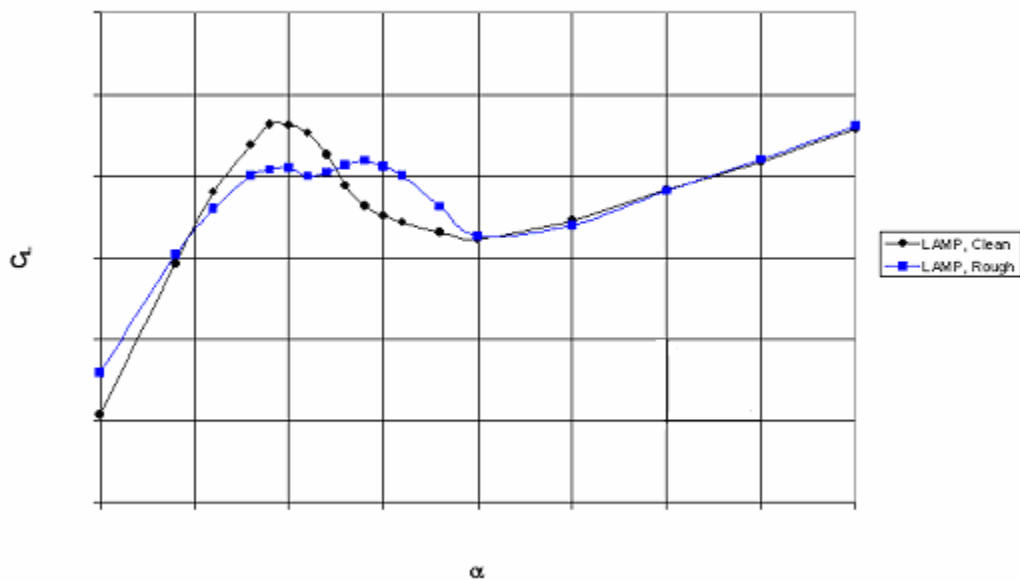


Figure 25. – Effect of pre-activation ice (roughness) on lift coefficient for 1/12-scale model in the LAMP wind tunnel

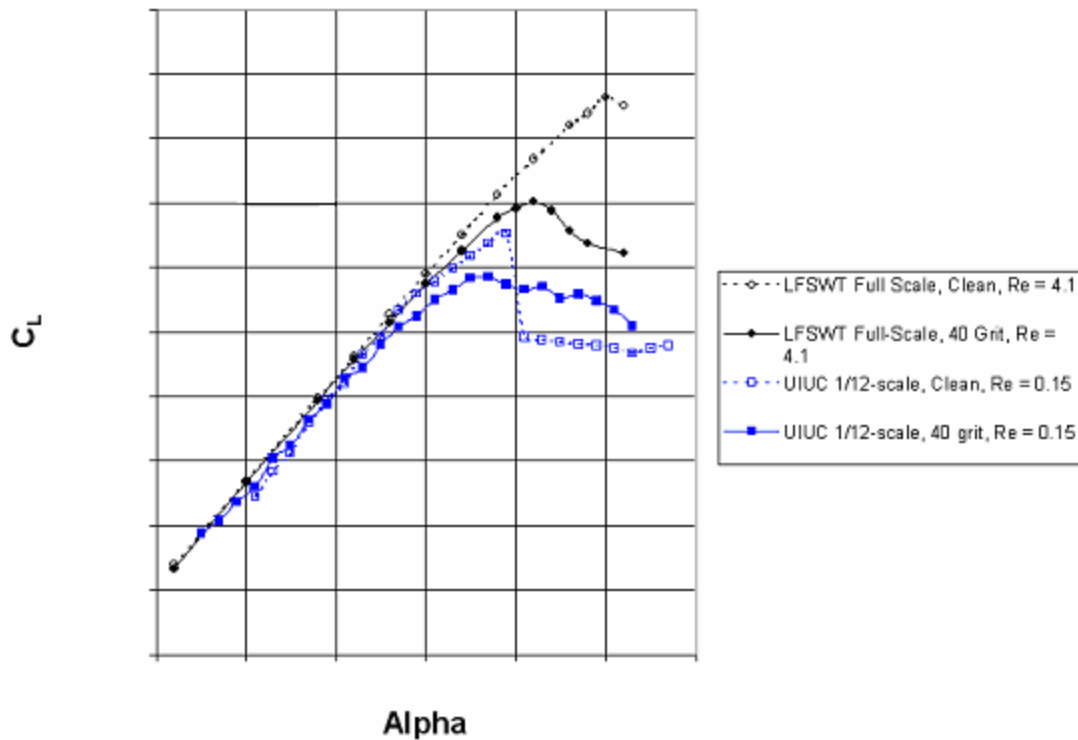


Figure 26. - Comparison of lift coefficients for clean wing and pre-activation ice for wing panel tests at high and low  $Re$ .

The effect of the pre-activation ice configuration on the lift coefficient of the 1/12-scale model is shown in Figure 25. For this condition, a decrease in maximum lift coefficient and a change in the post-stall lift characteristics are observed. For the wing panel tests, Figure 26, proportionately similar loss in maximum lift was observed for both the full-scale and 1/12-scale wing panels when 40 grit roughness was used. Furthermore, the 1/12-scale stall behavior with roughness, that was observed in the wing panel tests, is similar to what is observed for the complete airplane tests. For the full-scale wing panel test, the roughness resulted in a reduced stall angle of attack, as well. For math modeling the same proportional loss in lift and stall angle needs to be maintained when shifting the data.

The runback ice condition results in a change in lift slope and a loss in maximum lift coefficient, as shown in Figure 27. The shape of the lift curve, however, remains essentially the same. The wing panel tests showed similar results at both the high and low  $Re$  conditions, Figure 28, but at the low  $Re$  the change in lift slope was significantly greater. For math modeling, some adjustment needs to be made to the lift slope as well as shifting to the appropriate full-scale stall angle of attack. The proportional loss of lift in the LAMP test should be maintained during the  $Re$  adjustment.

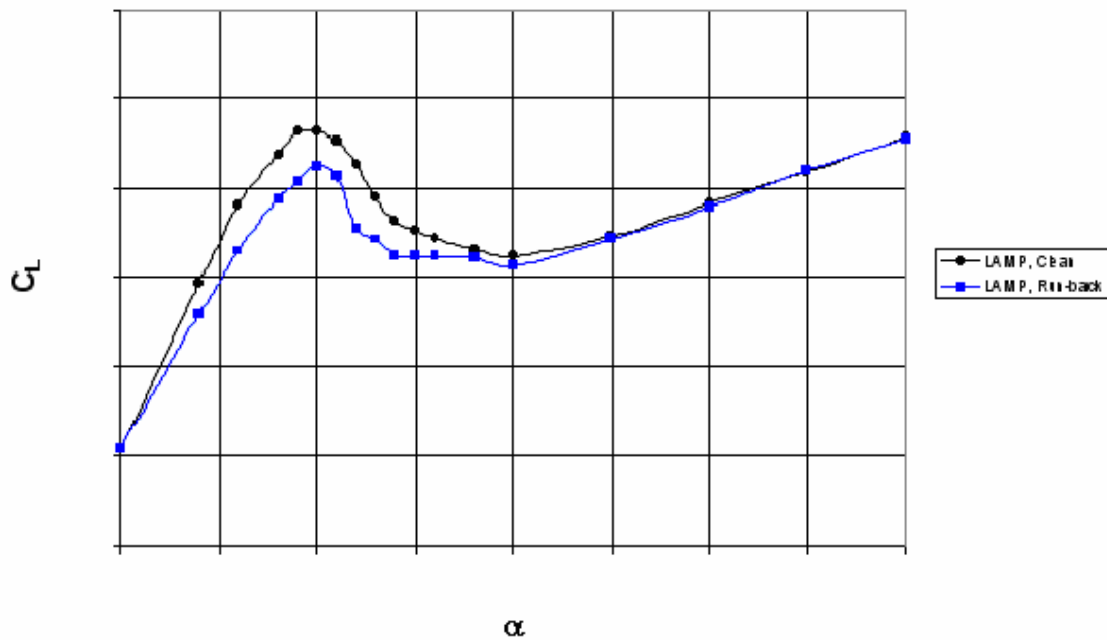


Figure 27. – Effect of runback ice on lift coefficient for 1/12-scale model in the LAMP wind tunnel.

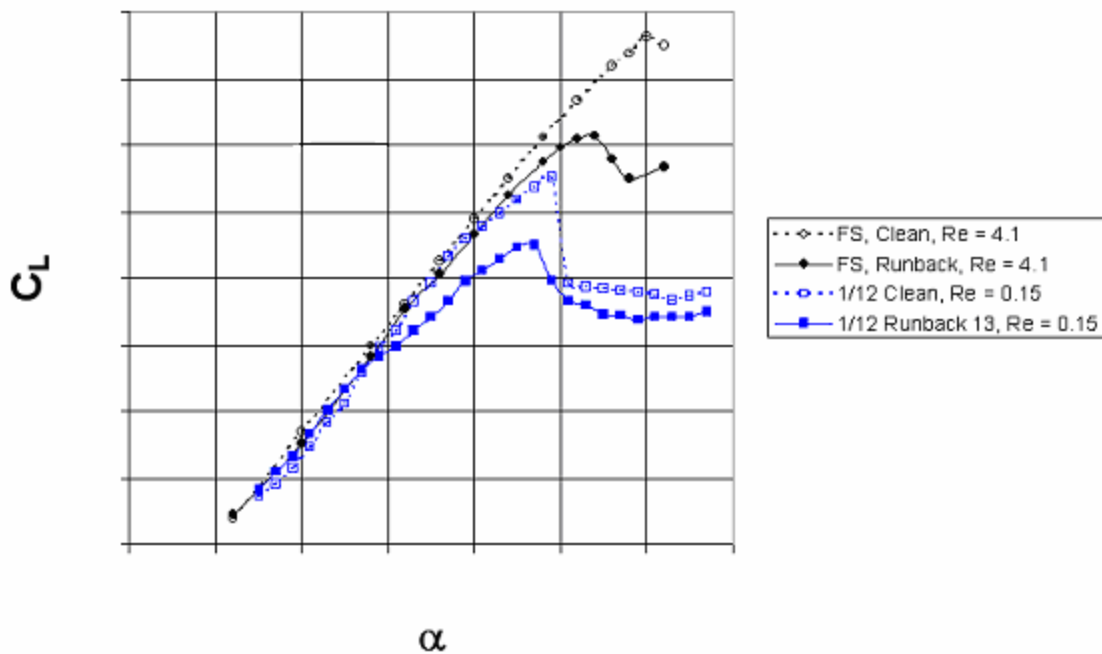


Figure 28. - Comparison of lift coefficients for clean wing and runback ice for wing panel tests at high and low Re.

The effects of ice configuration on pitching moment are shown in Figure 29 through Figure 31 for the failure ice, pre-activation ice, and runback ice configurations, respectively. The effects at stall and post-stall that were seen in lift are somewhat mirrored in the pitch characteristics in the post stall region in that the shape of the pitch curves with the failure and pre-activation ice conditions are modified and less maximum nose-down moment is obtained, while the runback ice condition results in very similar pitch characteristics to the un-iced airplane.

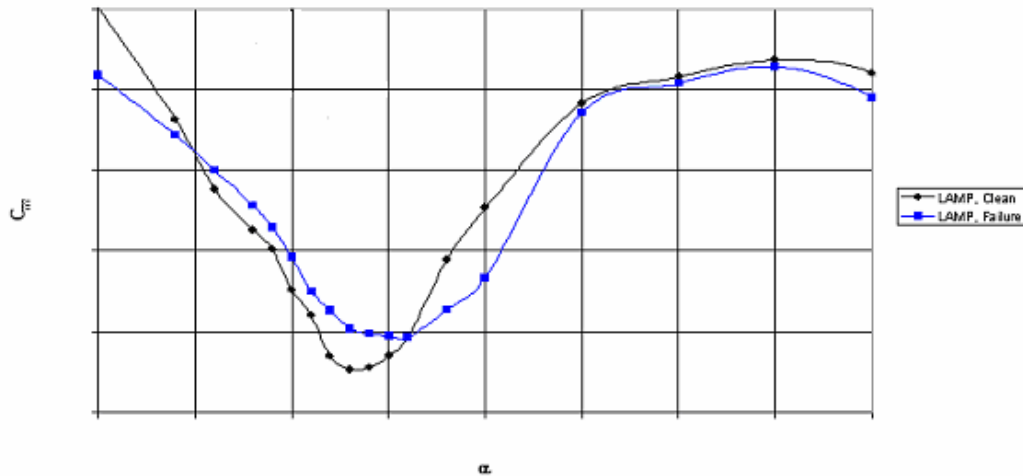


Figure 29. – Effect of failure ice on pitching moment coefficient for 1/12-scale model in the LAMP wind tunnel.

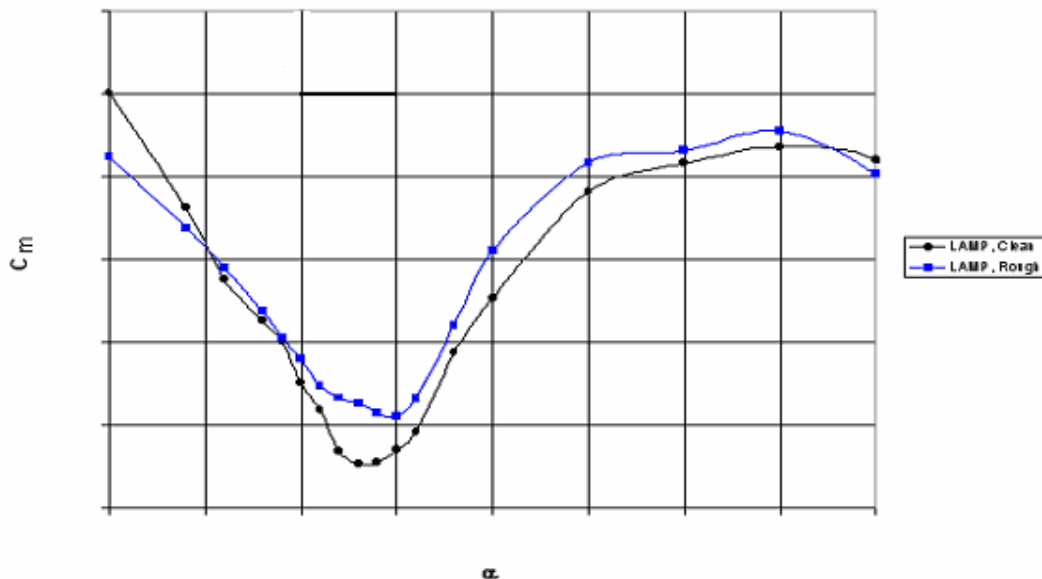


Figure 30. – Effect of pre-activation ice on pitching moment coefficient for 1/12-scale model in the LAMP wind tunnel.

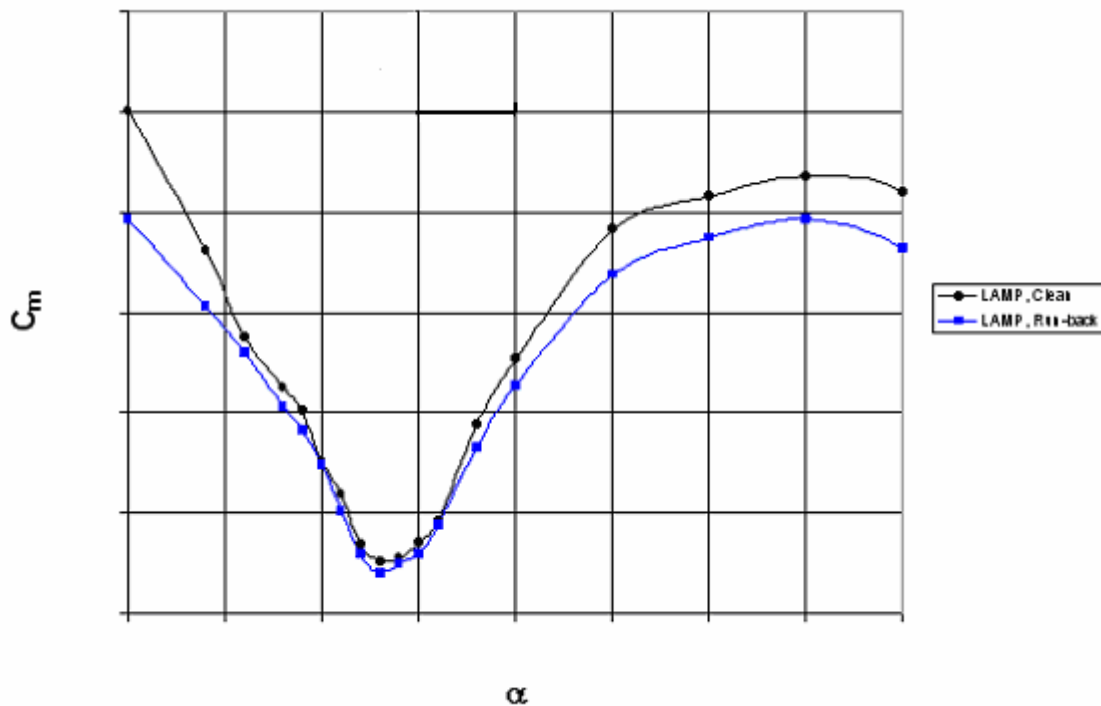


Figure 31. – Effect of runback ice on pitching moment coefficient for 1/12-scale model in the LAMP wind tunnel.

The influence of ice condition on the lateral directional stability is shown in Figure 32 and 33 for yawing moment and rolling moment, respectively, for ten degree sideslip angles. The yawing moment for this airplane, as measured on the 1/12-scale model in the LAMP tunnel starts out stable and actually increases stability significantly in the stall region before decreasing at larger post-stall angles of attack. The presence of ice does not significantly influence the yaw characteristics except for a decrease in the stability level at the low angles of attack, and a delay in the increase in the stall region for the failure condition.

The rolling moment, like the yaw, exhibits stability at the low angles of attack and increases in the stall region before decreasing somewhat at higher angles of attack. The presence of ice also causes a small decrease in rolling moment at sideslip at low angles of attack, as was seen in yaw. The failure ice condition and, to a lesser degree, the pre-activation ice condition delay the increase in rolling moment at stall.

In developing the math model all of the changes associated with the ice conditions have to be shifted to the appropriately higher angle of attack of the full-scale airplane stall.

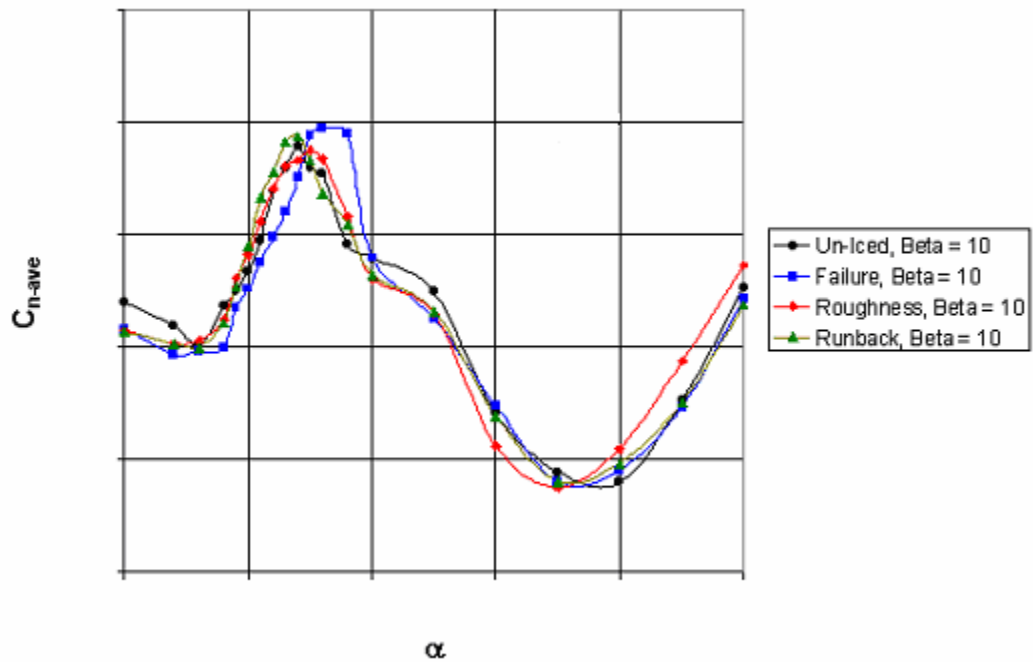


Figure 32. – Effect of ice shapes on yawing moment coefficient for 1/12-scale model in the LAMP wind tunnel. Data is average of the increments for  $\pm 10^\circ$  beta expressed for positive  $10^\circ$  beta.

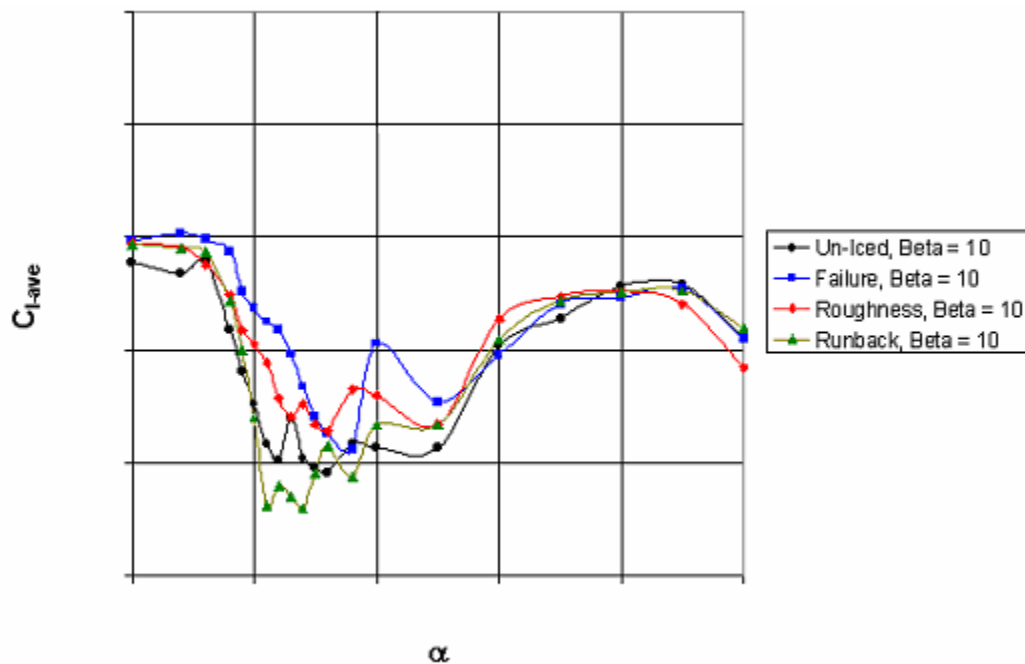


Figure 33. – Effect of ice condition on rolling moment coefficient for 1/12-scale model in the LAMP wind tunnel. Data is average of the increments for  $\pm 10^\circ$  beta expressed for positive  $10^\circ$  beta.

Most of the rotational data were not significantly influenced by the presence of the ice shapes. The primary exception was the rotational roll characteristics in the stall region. Near the stall, when the airplane rotates about the velocity vector, one wing will be operating at a stalled angle of attack and the other one will be operating at an un-stalled angle of attack. This condition produces the propelling rolling moments typically exhibited by most airplanes in this region. Since the presence of the ice conditions modifies the stall characteristics, it would be expected that the rolling moments would be different as a result. Figure 34 shows the rotational rolling moment for the un-iced airplane and for the three ice conditions in the immediate post-stall region. At this angle of attack, the un-iced airplane and the one with runback ice exhibit similar propelling rolling moments, while the failure ice and pre-activation ice conditions produce generally lightly damped rolling moments. The runback ice condition produced similar stall characteristics to the un-iced airplane, except shifted to lower maximum lift values, so it is not surprising that the rolling moment characteristics for these conditions are similar at stall. Both the failure ice case and the pre-activation roughness case also produced similar stall characteristics that were generally less abrupt than the un-iced airplane, so they both produce less propelling rolling moments.

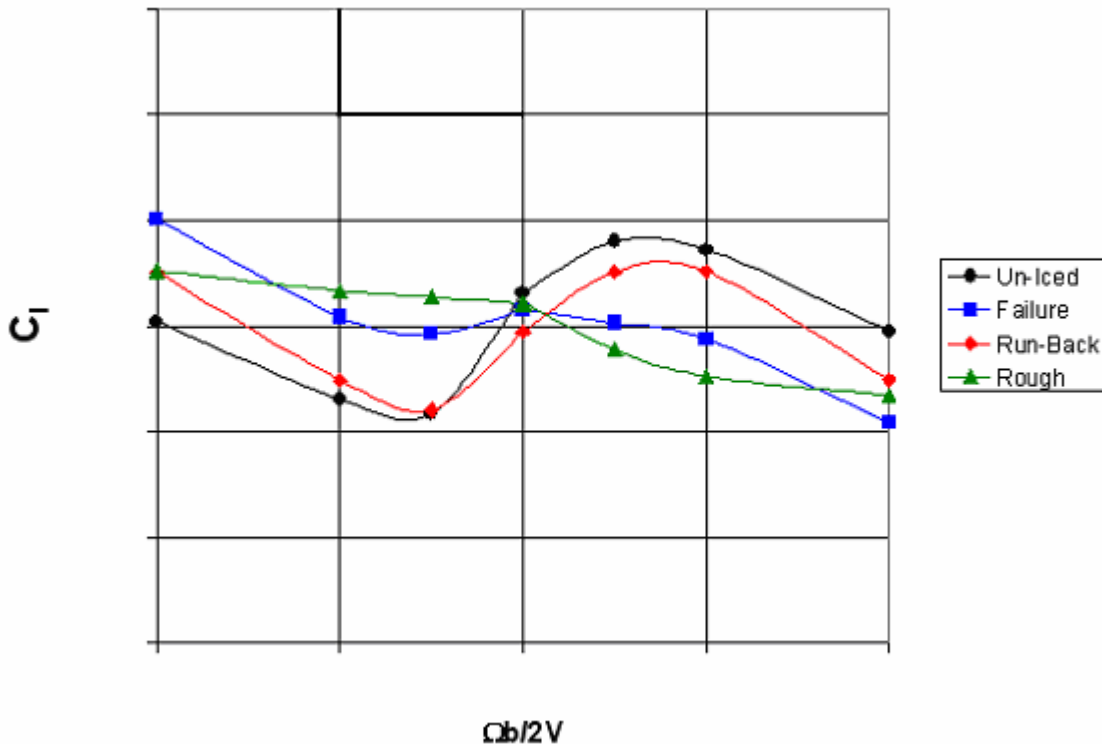


Figure 34. - Effect of ice condition on rotational rolling moment coefficient for 1/12-scale model in the LAMP wind tunnel in the immediate stall angle of attack region.

Figure 35 shows the same comparison at an angle of attack further into the stall region. At this angle of attack, the un-iced and runback ice airplanes

experience nearly equal lift on both the up-going and down-going wings and as a result, the rotational rolling moments are small, though still propelling. The failure and pre-activation ice conditions are still exhibiting significant propelling rolling moments because the lift on the down-going wing is still significantly less than on the up-going one. At angles of attack very far above stall, Figure 36, where both wings are fully stalled, all of the rotational rolling moments are essentially the same independent of the ice condition.

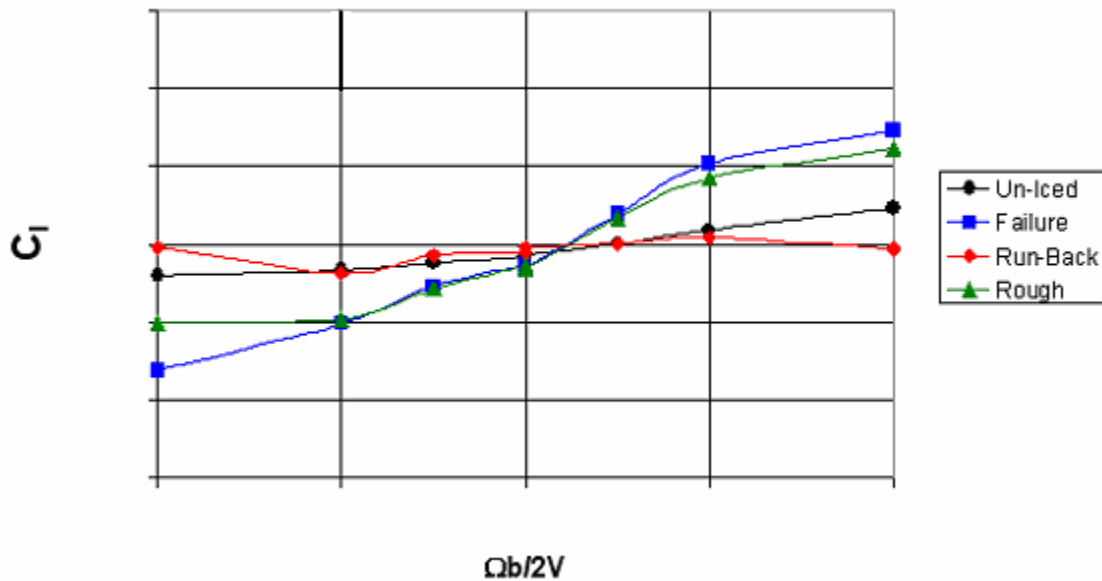


Figure 35. - Effect of ice condition on rotational rolling moment coefficient for 1/12-scale model in the LAMP wind tunnel in the post-stall angle of attack region.



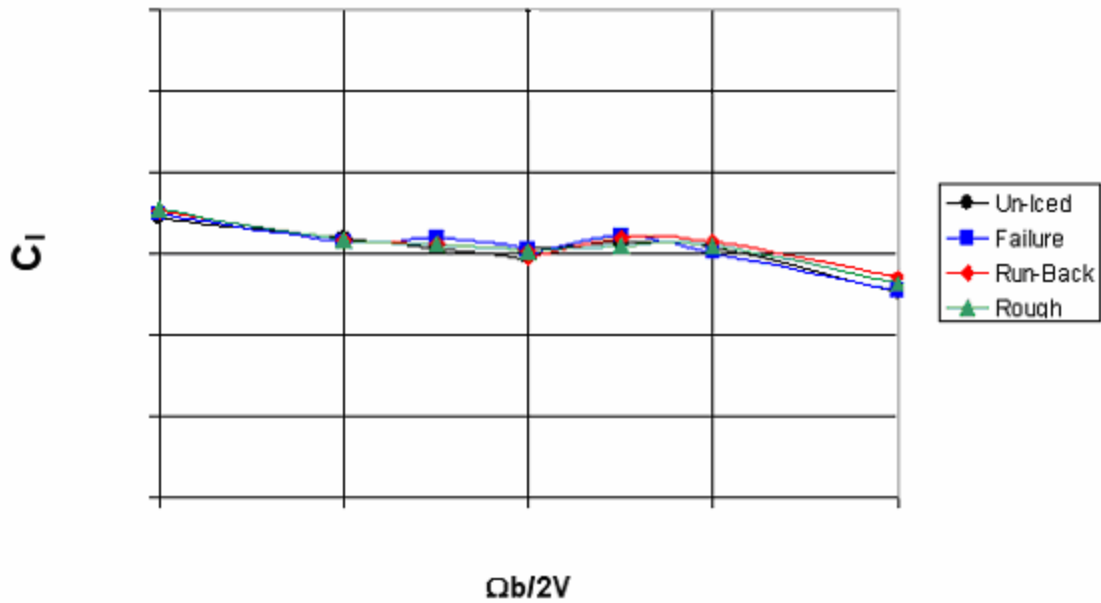


Figure 36. - Effect of ice condition on rotational rolling moment coefficient for 1/12-scale model in the LAMP wind tunnel in the fully-stalled angle of attack region.

As would be expected, the body axis damping in roll characteristics are very similar to the rotational rolling moment vs  $\Omega b/2V$  at low angles of attack where the  $\Omega$ -vector and the  $p_{body}$ -vector nearly line up. As the angle of attack increases, this is no longer the case. At un-stalled angles of attack, the airplane is well damped in roll with all of the tested ice conditions, as shown in Figure 37. The presence of ice does reduce the damping somewhat, but the damping levels are large enough in the normal flight region that it will probably not be noticeable to the pilot. In the stall region, the un-iced airplane and the airplane with runback ice tend to be more propelling as was seen for the rotational data and for the same reasons, Figure 38.

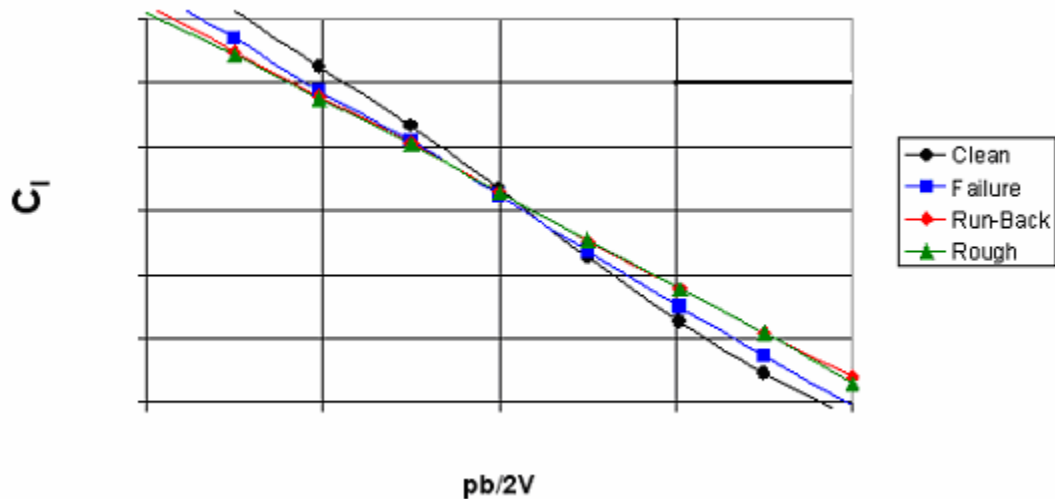


Figure 37. – Effect of ice condition on the rolling moment coefficient due to body-axis roll rate in the un-stalled angle-of-attack region for the 1/12-scale model in the LAMP wind tunnel.

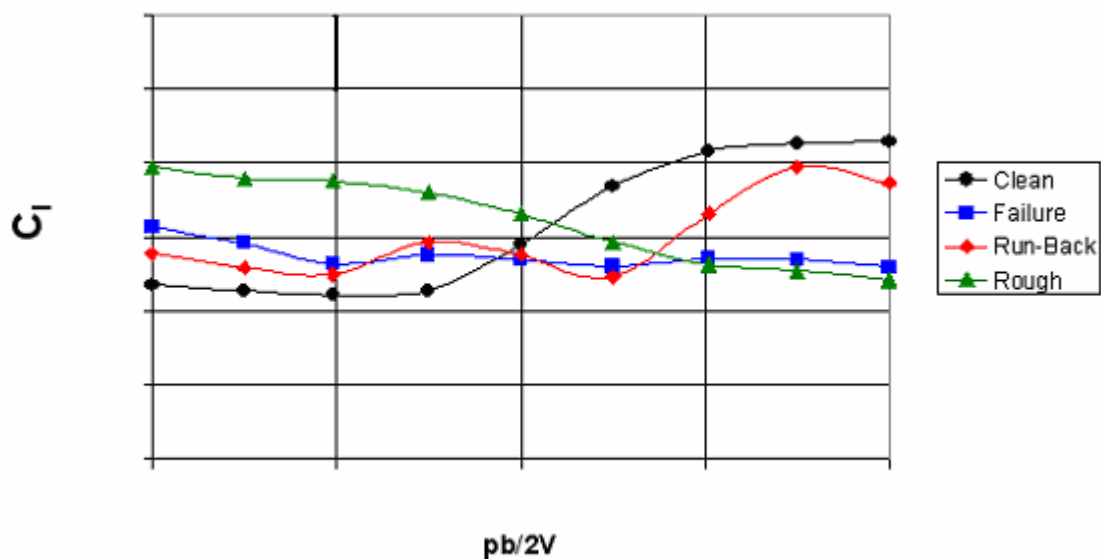


Figure 38. - Effect of ice condition on the rolling moment coefficient due to body-axis roll rate in the stall angle-of-attack region for the 1/12-scale model in the LAMP wind tunnel.

The forced oscillation results in yaw produced similar results for all ice conditions tested throughout the tested angle of attack region. Where there were small differences, they generally occurred in the stall region and the un-iced and runback ice conditions, again, produced similar characteristics as did the failure and pre-activation ice conditions, as shown in Figure 39 and Figure 40

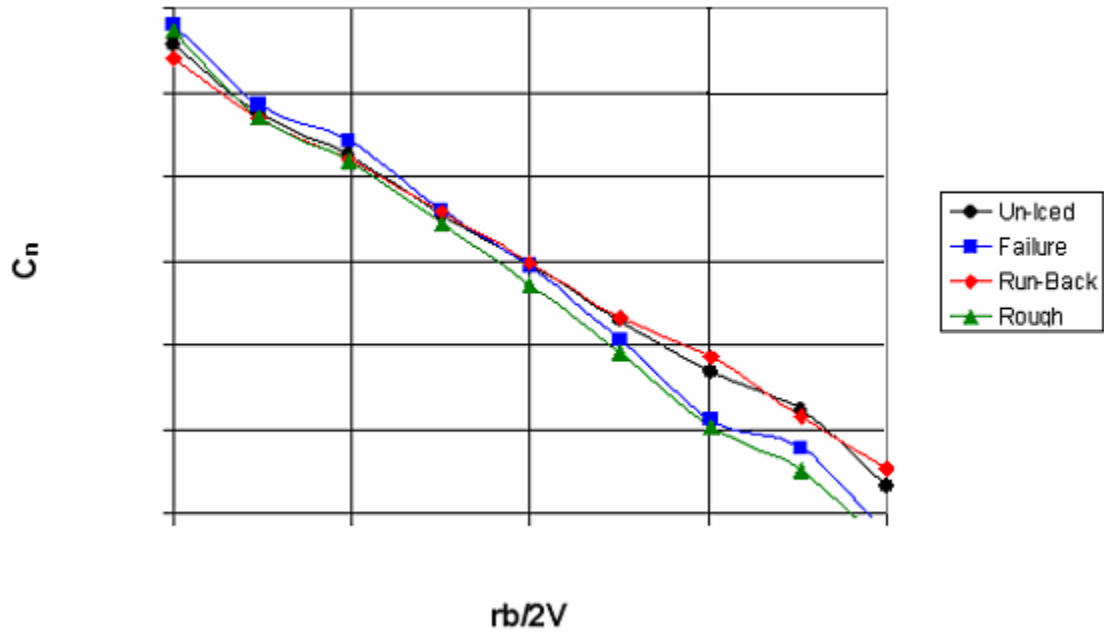


Figure 39. – Effect of ice condition on the yawing moment coefficient due to body-axis yaw rate in the post-stall angle of attack region for the 1/12-scale model in the LAMP wind tunnel.

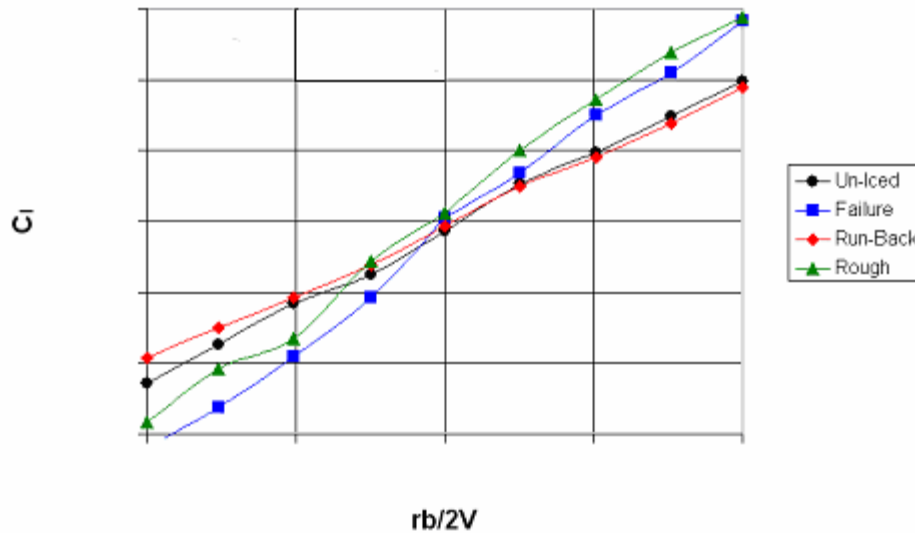


Figure 40. – Effect of ice condition on the rolling moment coefficient due to body-axis yaw rate in the post-stall angle of attack region for the 1/12-scale model in the LAMP wind tunnel.

Pitch damping was not significantly influenced by the ice condition at any tested angle of attack. Figure 41 and Figure 42 show the pitch damping curves at an un-stalled and a stalled angle of attack. The curves separate because of

the static shifts that occur with ice condition at the presented angles of attack, but the slopes are not significantly influenced by ice condition.

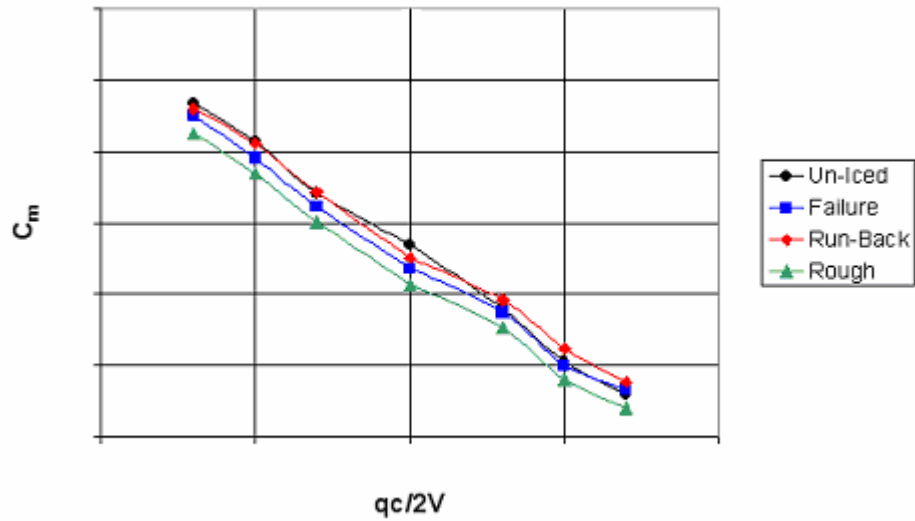


Figure 41. - Effect of ice condition on the pitching moment coefficient due to body-axis pitch rate in the un-stalled angle of attack region for the 1/12-scale model in the LAMP wind tunnel.

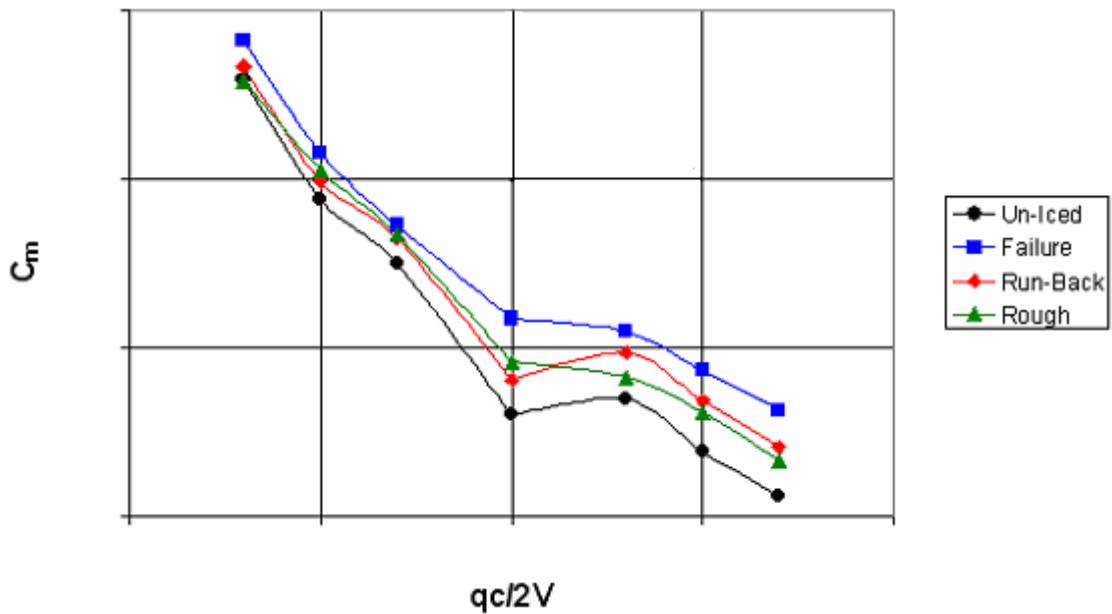


Figure 42. - Effect of ice condition on the pitching moment coefficient due to body-axis pitch rate in the stalled angle of attack region for the 1/12-scale model in the LAMP wind tunnel.

## 4. SIMULATION IMPLEMENTATION

### 4.1. *Initial modeling*

Once the complete airplane wind tunnel data measured at the LAMP facility were available and with the conclusions of how to properly shift the data to represent the full-scale Re conditions, the construction of the simulation math model could begin. The ground rules for the math model were that it would be a large angle, non-linear model that would capture all of the typical non-linearities in the stall and post-stall regions. Consequently, data tables for coefficients would be used to capture all of the functionalities. The model had to be representative of the full-scale airplane, so all stall related characteristics had to be shifted to the appropriate full-scale stall angle of attack. The model had to be capable of simulating all flap deflections for the clean airplane, as well as all three of the tested icing conditions.

#### 4.1.1. Baseline Airplane

The complete airplane data set measured at LAMP was used as the basis for the simulation modeling data base. Some modifications were made to this based on a previously measured, but less complete, higher Reynolds number data set supplied by Cessna in the form of a linearized model of the CJ2 airplane. Cessna also supplied flight extracted  $C_{Lmax}$  values for all three flap deflections. As was discussed in the previous section, by comparing the higher Re lift curve, the flight Re  $C_{Lmax}$  and the LAMP data it was determined that a good match for the un-iced airplane was obtained by shifting the lift curve up to match the maximum lift value and then shifting the angle of attack to force the curves to overlay. All of the wind tunnel data characteristics as a function of angle of attack were subsequently also shifted by the same amount so that the characteristics that were observed at stall would occur at the proper full-scale angle of attack (e.g., Figures 43 and 44).

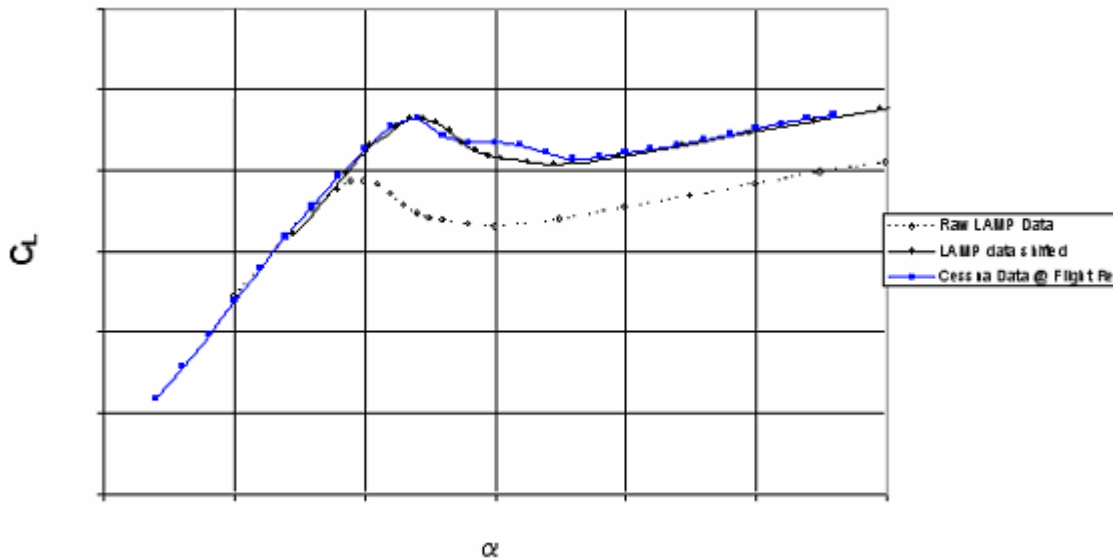


Figure 43. – Comparison of Low-Speed LAMP Lift Coefficient with Cessna Flight Re Characteristics for the No-Ice, Flaps = 0 condition before and after the correction for Re.

The low Re LAMP wind tunnel data has sometimes shown lower levels of control powers and in some cases lateral and/or directional stability than is observed at some higher speed tests for the same configurations and from flight data. Consequently, the low angle of attack LAMP measured levels were compared to the Cessna linear model values to see if the low angle of attack data required shifting. In many cases, at least some increase in control power and stability was incorporated in order to match the Cessna data.

Consequently, the guidelines used for the no-ice model were:

- All data were shifted so that the behavior at stall would occur at the proper angles of attack
- If there were a difference in the zero angle-of-attack data between the LAMP data and the Cessna data, the LAMP data would be adjusted, assuming that the adjustment made sense compared to what had been observed to be required from other tests in the LAMP tunnel.

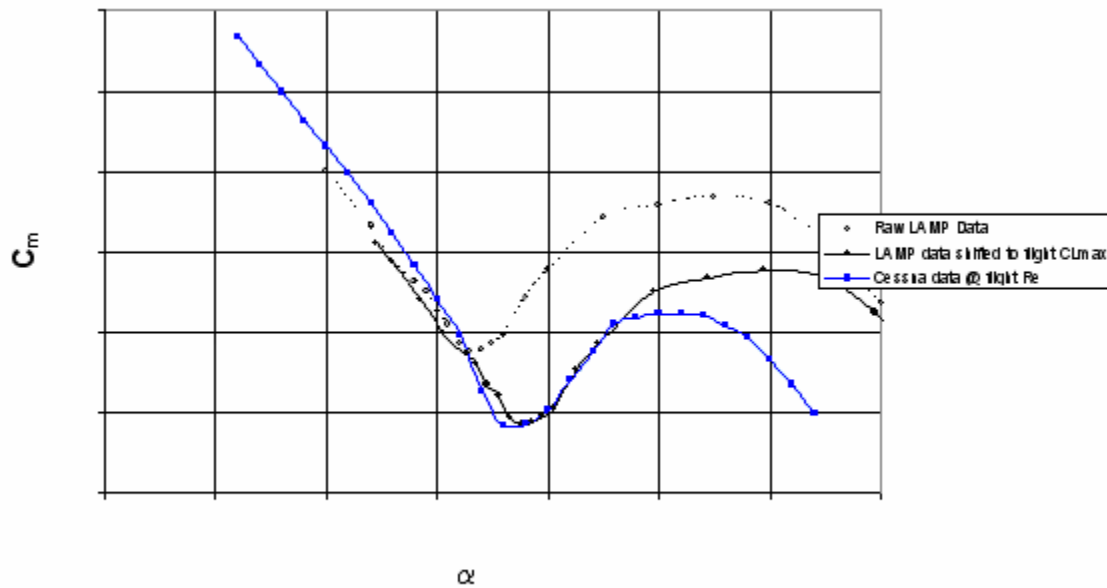


Figure 44. – Pitching moment coefficient plots showing the effect of shifting the pitch curves similarly to what was done for Lift; No-Ice, Flaps = 0.

Using these guidelines, the initial simulation model was constructed. In addition, The manufacturer had supplied their business jet simulation model that had high-speed data tables that were functions of Mach number. Incremental tables of the Mach effects were constructed in the D-Six format and included with the new model.

The data tables were used to construct a D-Six project of the business jet and after initial check-out, a preliminary validation effort was undertaken using supplied clean airplane flight data. The flight data supplied included control doublets in pitch, roll, and yaw, steady heading sideslips, stalls, and flap extensions and retractions.

#### 4.1.1.1. Static Aerodynamic Characteristics

Using the stall flight records it was found that while the results showed good matches in all cases for the un-stalled portion of the flight, some adjustments were required in the stall and immediate post-stall region in order to improve the match of the total lift coefficient. Consequently, the lift curves in this region were adjusted, as shown in Figures 45 through 47 for the three flap deflection tables.

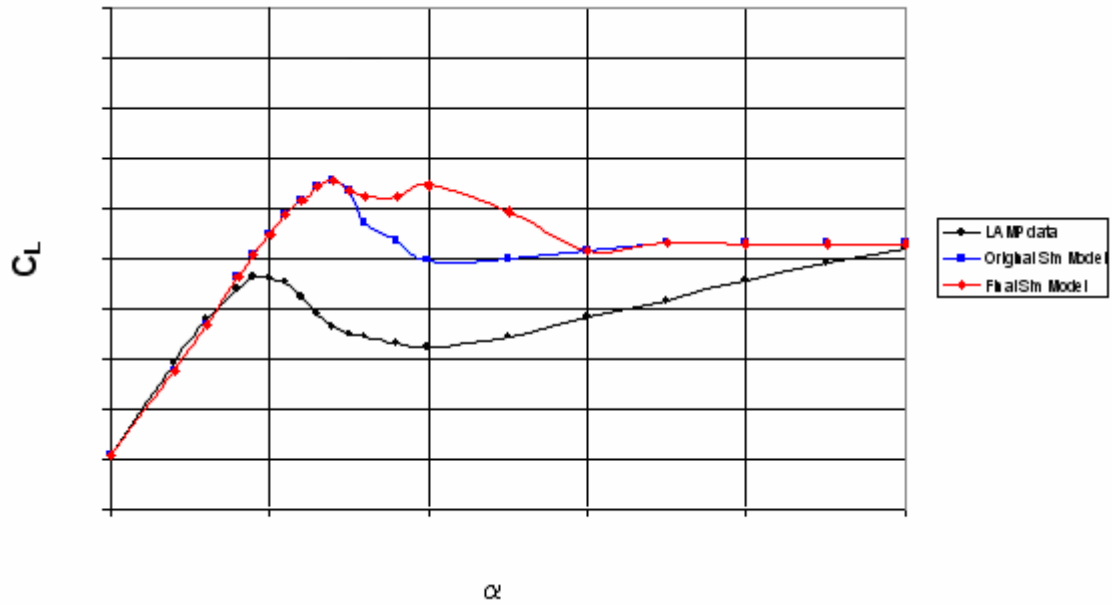


Figure 45. – Comparison of No-Ice Lift Coefficient from the LAMP Wind-Tunnel Data, the Initial Math Model, and the Final Model after Validation, Flaps = 0.

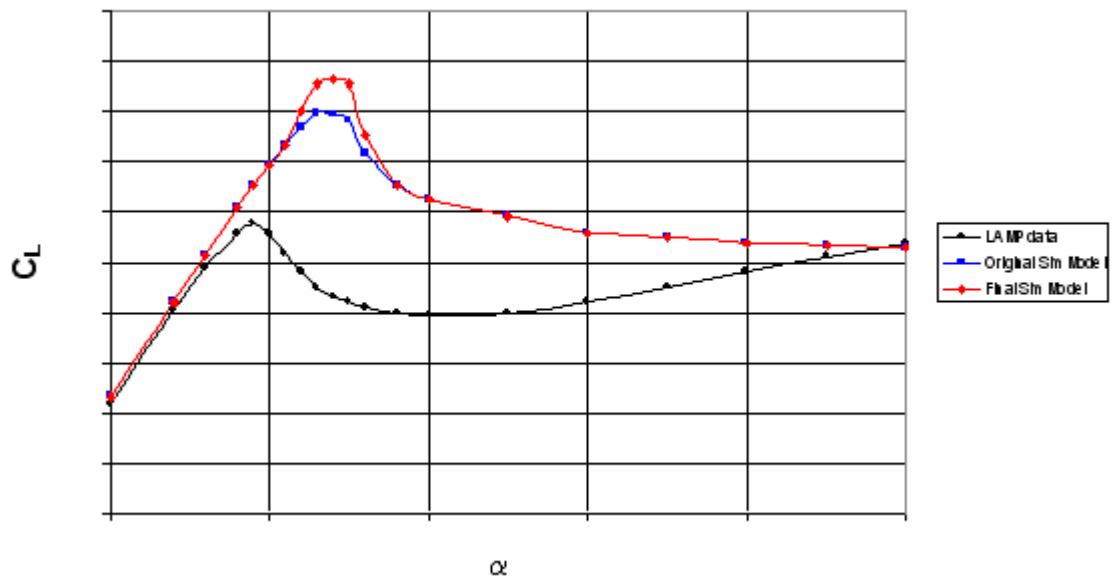


Figure 46. – Comparison of No-Ice Lift Coefficient from the LAMP Wind-Tunnel Data, the Initial Math Model, and the Final Model after Validation, Flaps = 20.



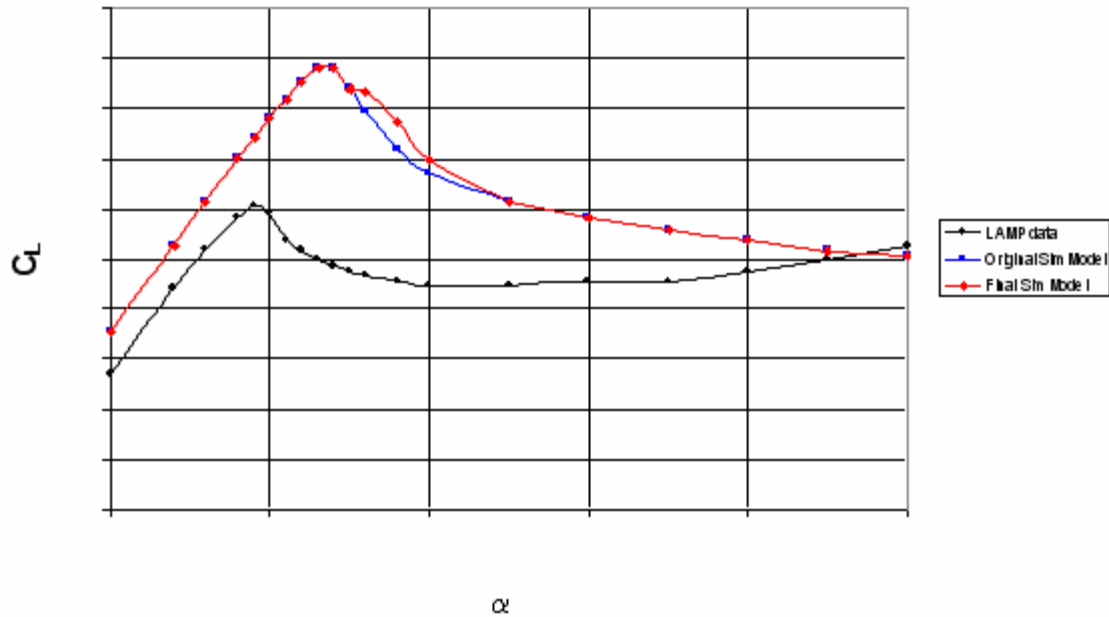


Figure 47. – Comparison of No-Ice Lift Coefficient from the LAMP Wind-Tunnel Data, the Initial Math Model, and the Final Model after Validation, Flaps = 40.

The pitching moment coefficient curves were adjusted primarily based on pitch doublet overdrive runs. These comparisons provided the required adjustments to both the basic  $C_m$  vs. angle of attack characteristics (Figures 48 and 49) and the elevator pitch control term,  $\Delta C_{m\delta e}$  (Figures 50 and 51).

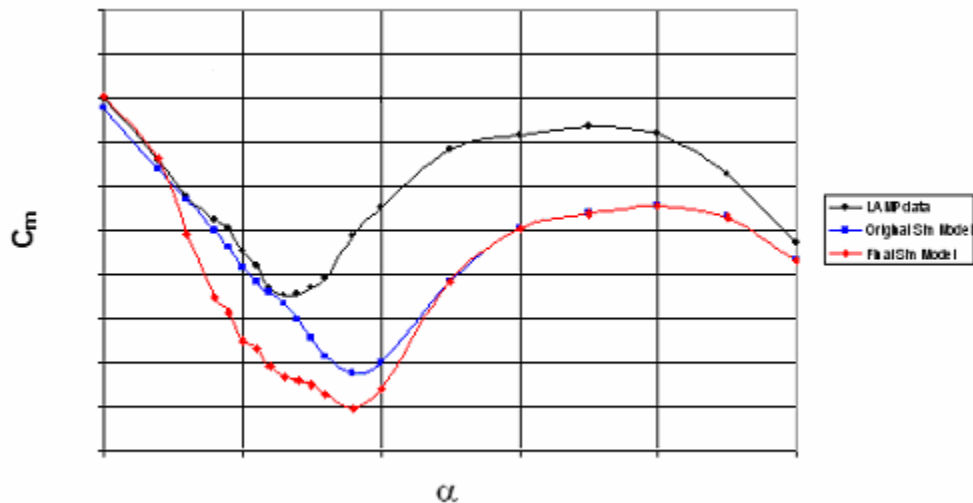


Figure 48. – Comparison of No-Ice Pitching Moment Coefficient from the LAMP Wind-Tunnel Data, the Initial Math Model, and the Final Model after Validation, Flaps = 0.

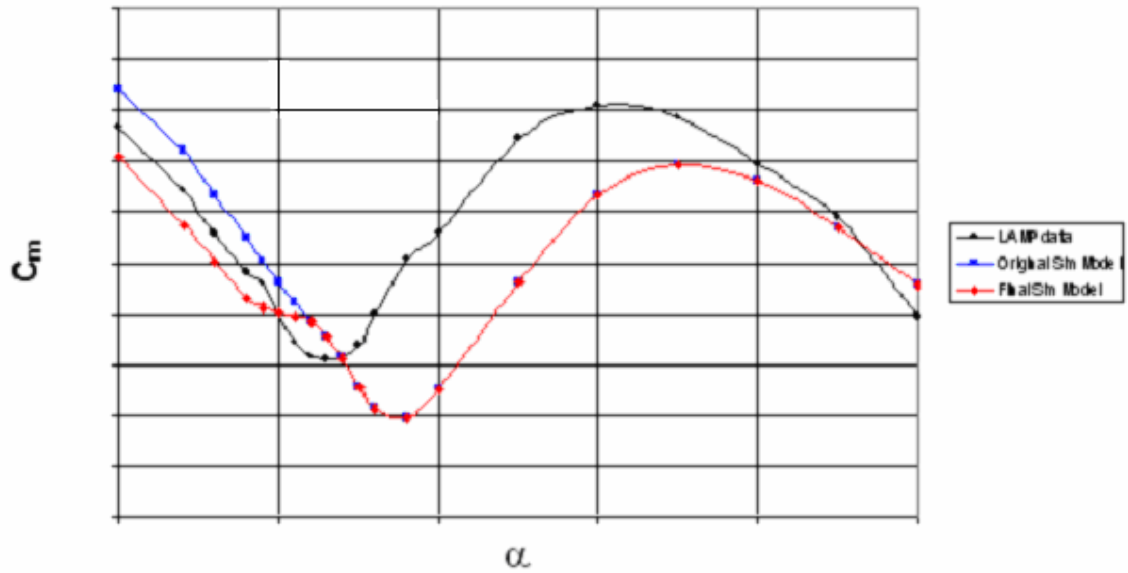


Figure 49. – Comparison of No-Ice Pitching Moment Coefficient from the LAMP Wind-Tunnel Data, the Initial Math Model, and the Final Model after Validation, Flaps = 20.

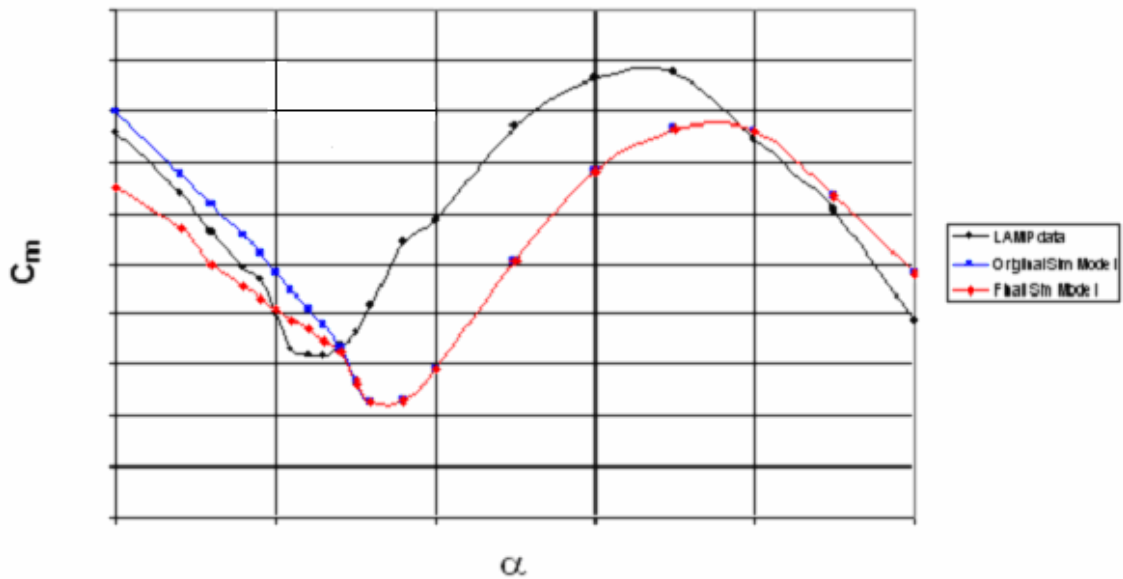


Figure 50. – Comparison of No-Ice Pitching Moment Coefficient from the LAMP Wind-Tunnel Data, the Initial Math Model, and the Final Model after Validation, Flaps = 40.

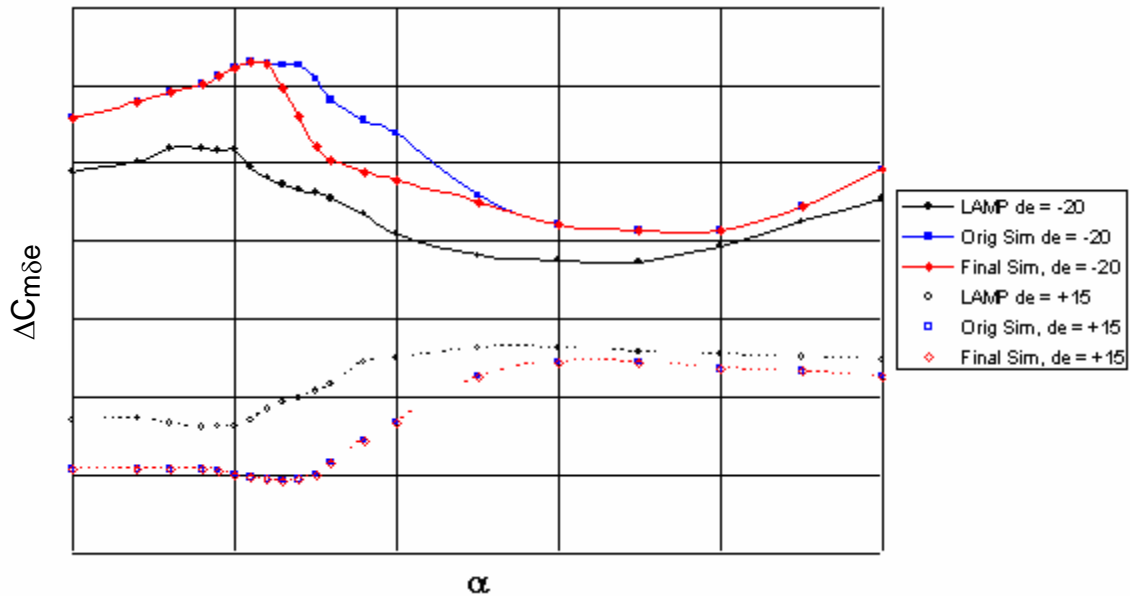


Figure 51. – Comparison of No-Ice Incremental Pitching Moment Coefficient due to elevator deflection from the LAMP Wind-Tunnel Data, the Initial Math Model, and the Final Model after Validation, Flaps = 0.

Some corrections were made to the incremental pitching moment due to elevator coefficient as a result of the validation effort, as shown in Figure 52 for flaps = 0.

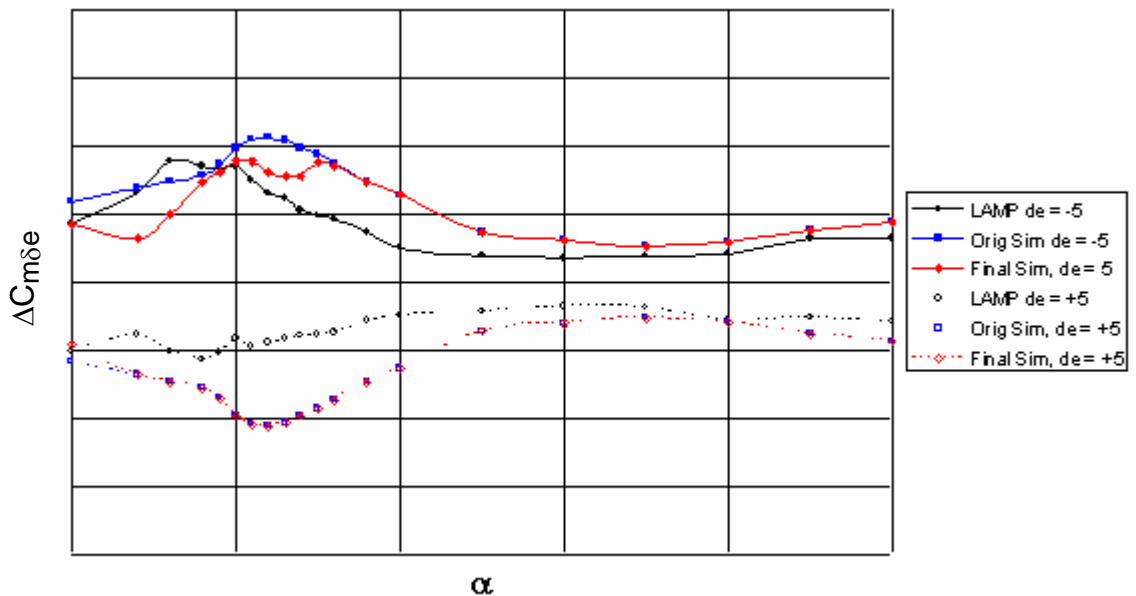


Figure 52. – Comparison of No-Ice Incremental Pitching Moment Coefficient due to elevator deflection from the LAMP Wind-Tunnel Data, the Initial Math Model, and the Final Model after Validation, Flaps = 0.

The drag coefficient data was shifted in angle of attack by the same 4.5 degree shift that was used for all of the data in order to agree with the full-scale Re stall. In the case of flaps = 0, the validation effort showed that the overdrive runs agreed better if the shift were essentially removed, as shown in Figure 53. For the other flap deflections, no changes were made to the original drag curves as a result of the validation effort (Figures 54 and 55).

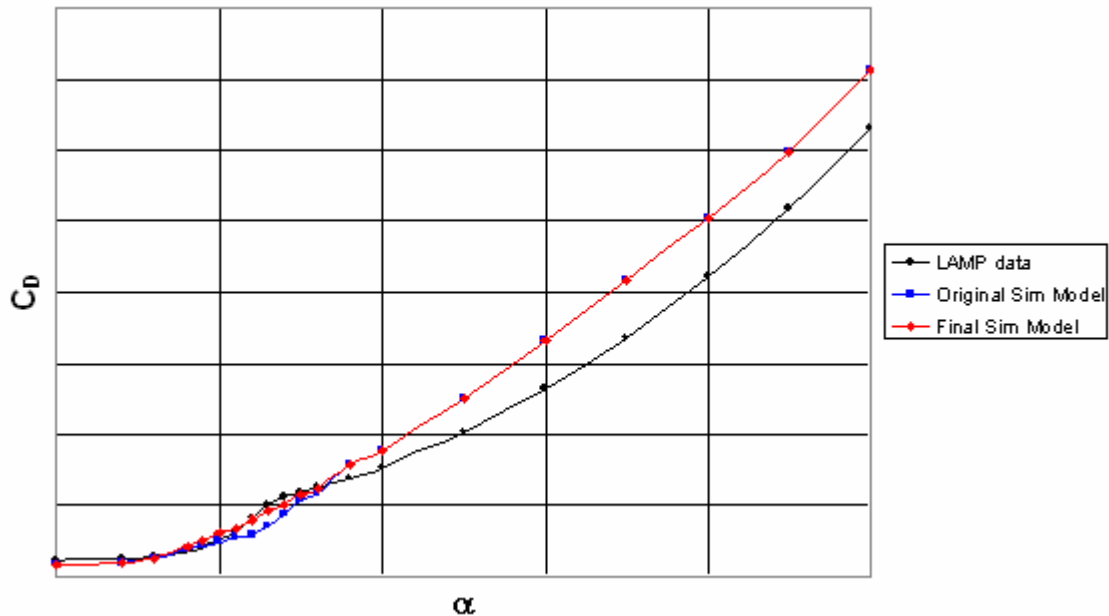


Figure 53. – Comparison of No-Ice Drag Coefficient from the LAMP Wind-Tunnel Data, the Initial Math Model, and the Final Model after Validation, Flaps = 0.

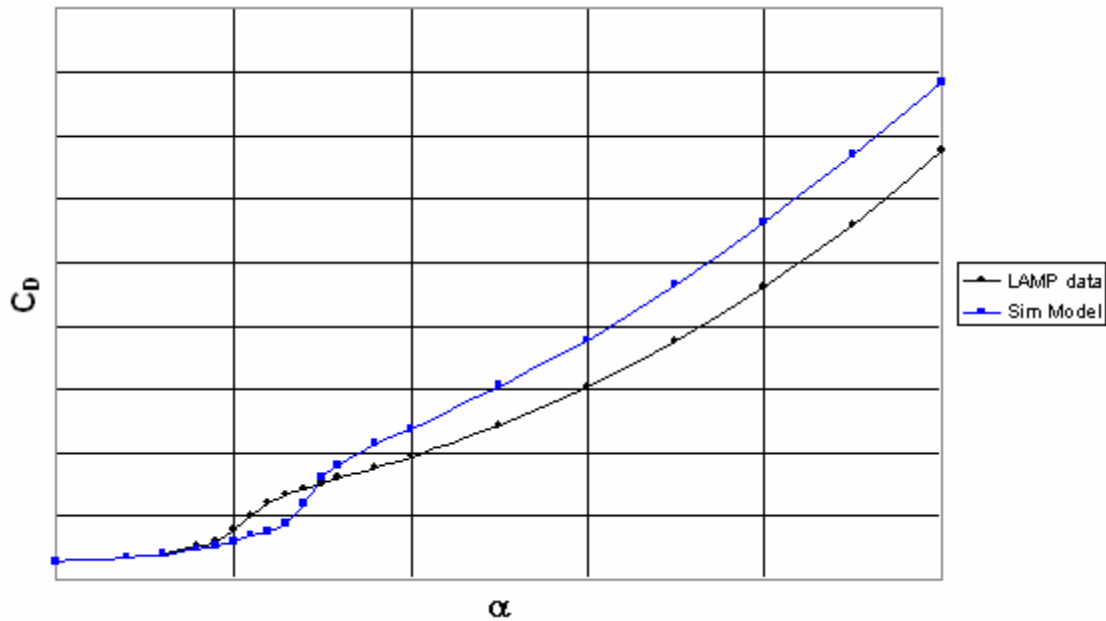


Figure 54. – Comparison of No-Ice Drag Coefficient from the LAMP Wind-Tunnel Data and the Math Model, Flaps = 20.

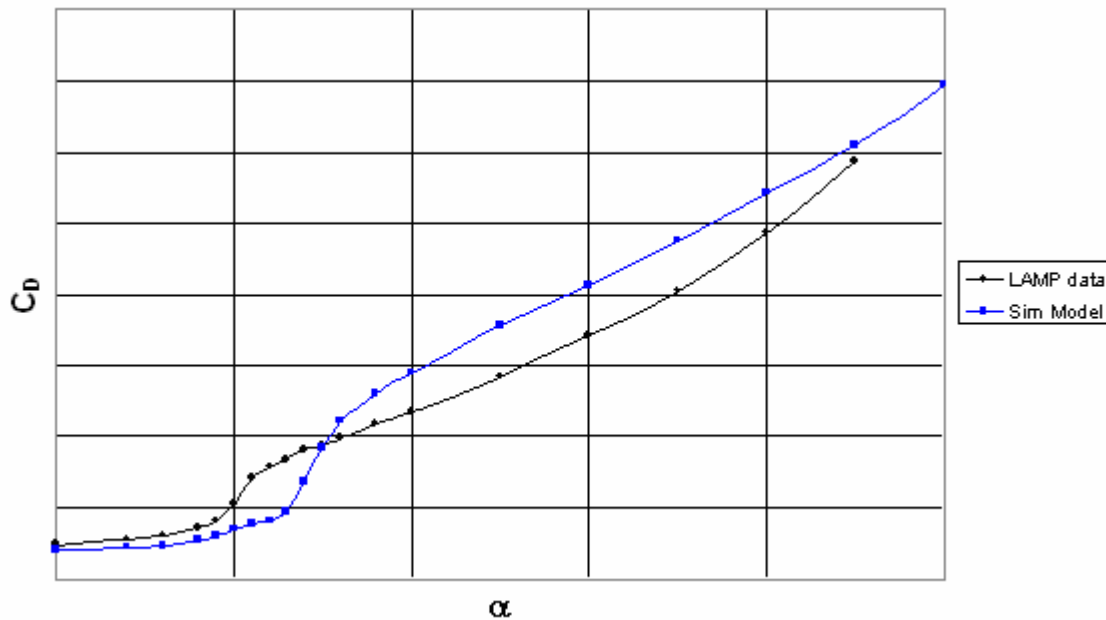


Figure 55. – Comparison of No-Ice Drag Coefficient from the LAMP Wind-Tunnel Data and the Math Model, Flaps = 40.

The rolling moment coefficient data were shifted in stall angle of attack and the low angle of attack lateral stability levels were also increased somewhat based on the manufacturer's data levels, as shown in Figure 56. The results of

the validation effort showed that these levels were too high, and they were reduced to closer to the LAMP tunnel data, as also shown in Figure 56.

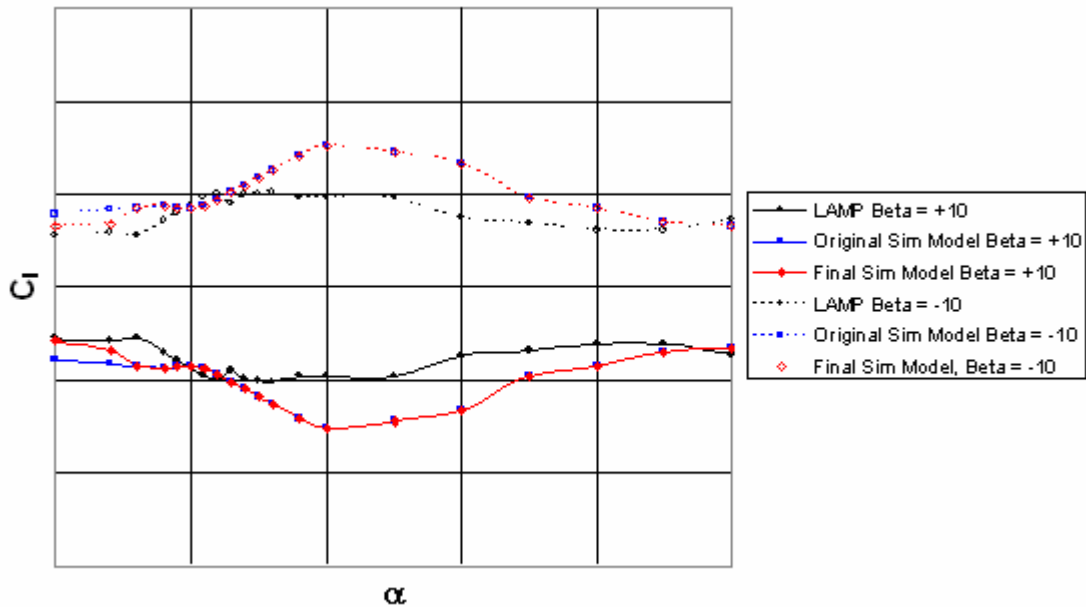


Figure 56. - Comparison of No-Ice Rolling Moment Coefficient at  $\pm 10^\circ$  sideslip from the LAMP Wind-Tunnel Data, Initial Math Model, and the Final Math Model after Validation, Flaps = 0.

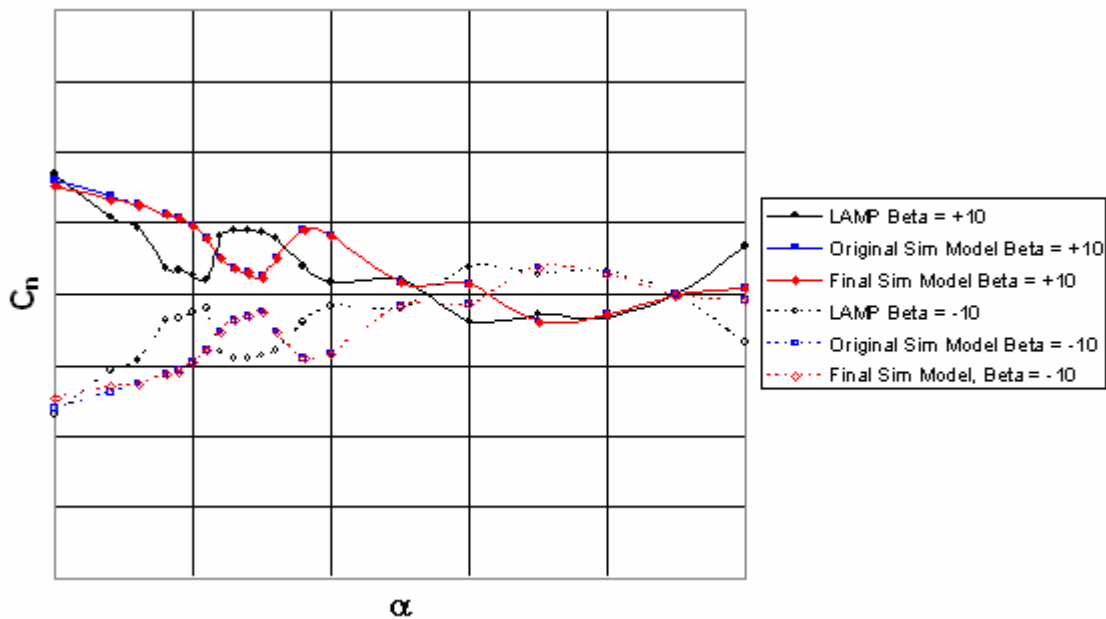


Figure 57. - Comparison of No-Ice Yawing Moment Coefficient at  $\pm 10^\circ$  sideslip from the LAMP Wind-Tunnel Data, Initial Math Model, and the Final Math Model after Validation, Flaps = 0.

The yawing moment coefficient curves were also shifted by the same  $4.5^\circ$  angle of attack as were the other coefficients. No other adjustments were made

to the data for the initial math model. The validation effort produced only a very small adjustment in the data near zero angle of attack, as shown in Figure 57.

Side force coefficient was shifted to the correct stall angle and the low angle of attack levels were adjusted somewhat to agree with the manufacturer's data levels. The validation showed that a reduction in the levels at low angles of attack was required for flaps = 0, as shown in Figure 58, but no adjustments were required for the other flap deflections.

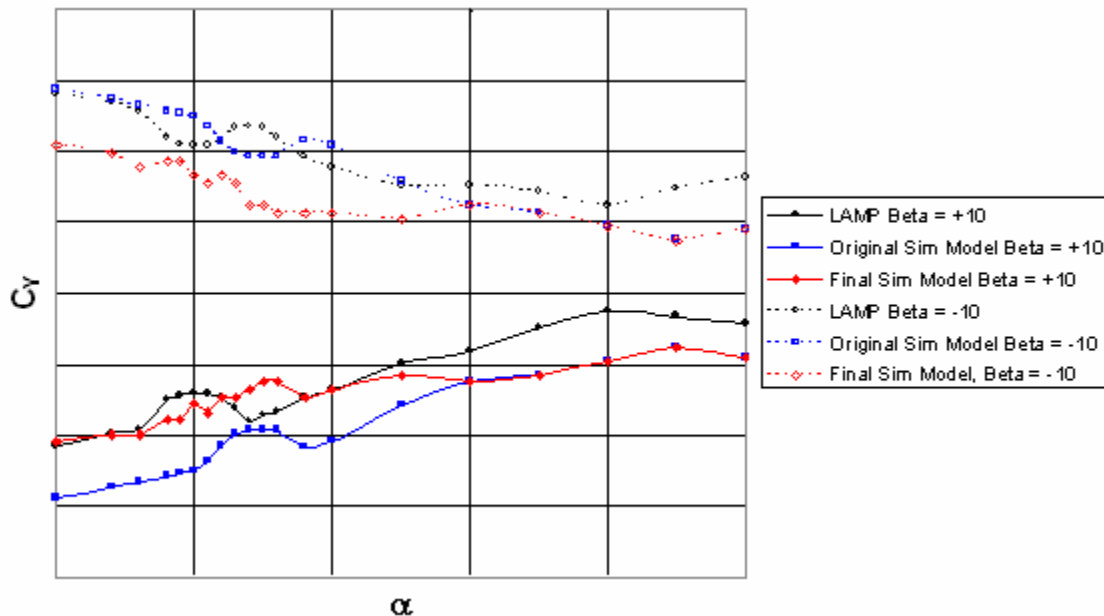


Figure 58. - Comparison of No-Ice Side Force Coefficient at  $\pm 10^\circ$  sideslip from the LAMP Wind-Tunnel Data, Initial Math Model, and the Final Math Model after Validation, Flaps = 0.

The rolling moment due to aileron deflection manufacturer's data showed significantly more control power at low angles of attack than was measured in the LAMP tunnel. Consequently, the initial math model values were shifted closer to those values in that angle of attack region, and the data were shifting for stall angle. The validation results indicated, however, that the values should be between the manufacturer and LAMP results, as shown in Figure 59.

The LAMP wind tunnel data showed some small levels of yawing moment due to the aileron deflections. However, the initial implementation of the model showed that it was difficult to fly at angles of attack near stall because of the adverse yaw with aileron inputs. Subsequent validation overdrives showed that the agreement with flight data was better if the term were zeroed out. Consequently, the term was dropped from the simulation model.

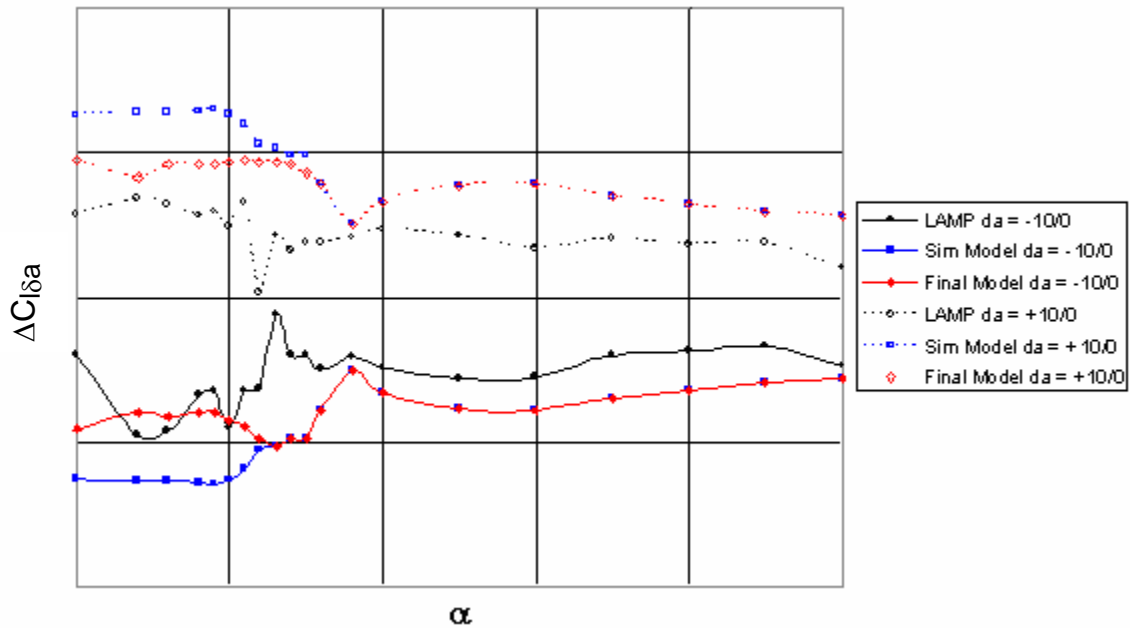


Figure 59. – Comparison of No-Ice Incremental Rolling Moment Coefficient due to aileron deflection from the LAMP Wind-Tunnel Data, the Initial Math Model, and the Final Model after Validation, Flaps = 0.

The change in yawing moment coefficient due to rudder deflection is shown in Figure 60. For this term, the manufacturer's data showed significantly larger values than the LAMP data and the simulation math model reflects these levels. No modifications to this term were made based on the validation Overdrive runs.



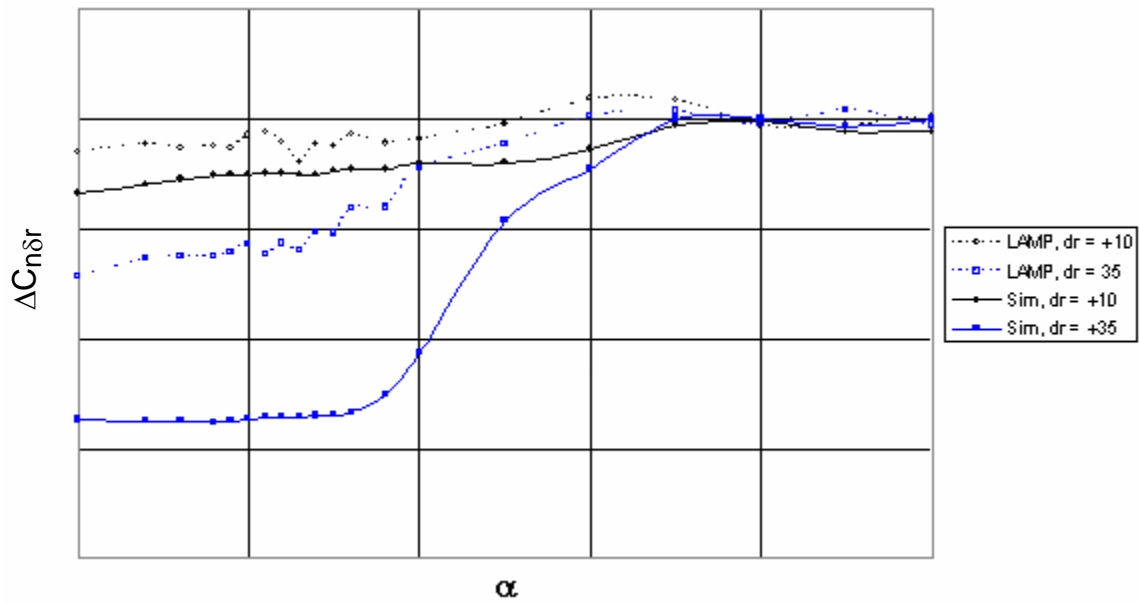


Figure 60. – Comparison of No-Ice Incremental Yawing Moment Coefficient due to rudder deflection from the LAMP Wind-Tunnel Data and the Math Model.

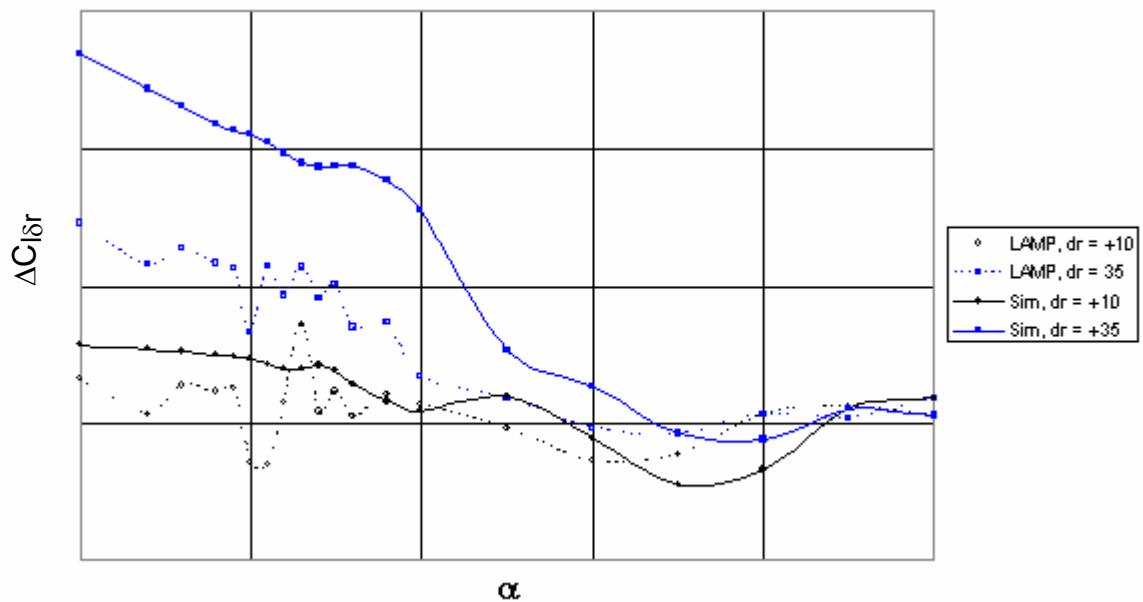


Figure 61. - Comparison of No-Ice Incremental Rolling Moment Coefficient due to rudder deflection from the LAMP Wind-Tunnel Data and the Math Model.

As with many of the other control effectiveness terms, the rolling moment due to rudder deflection as measured in the LAMP tunnel was lower in magnitude than the manufacturer's model data. Consequently, the data at low

angles of attack was shifted to agree with the manufacturer's data and then the data were shifted with angle of attack to agree with the full-scale stall angle. The comparison of the LAMP measured results and the simulation data is shown in Figure 61. No alterations were made to this term as a result of the initial validation effort.

#### 4.1.1.2. Body-Axis Damping Terms

The body axis damping terms were derived from forced oscillation testing at the BAR LAMP wind tunnel. The un-iced airplane simulation data tables for these terms used the data as they were measured in the tunnel, but the data were all shifted  $4.5^\circ$  in angle of attack to put the behavior at stall at the proper location for the full-scale airplane. These data terms are all implemented as incremental coefficients as functions of angle of attack and the non-dimensionalized body rates (e.g.  $qc/2V$ ,  $pb/2V$ , and  $rb/2V$ ). Sample plots comparing the incremental moments measured during the LAMP wind tunnel test with those modeled in the simulation data base are shown for selected angles of attack in figures 62 through 64 for the pitching, rolling, and yawing moment coefficients, respectively.

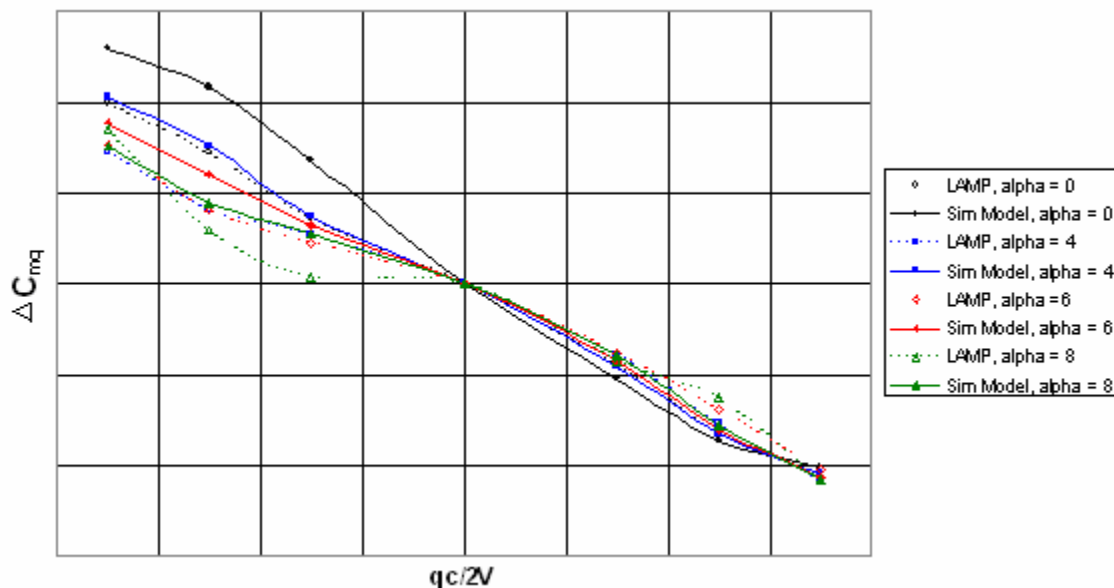


Figure 62. – Comparison of No-ice Incremental Pitching Moment Coefficient due to non-dimensionalized Pitch Rate for LAMP Wind Tunnel Data and for the Sim Model Data at selected Angles of Attack, Flaps = 0.

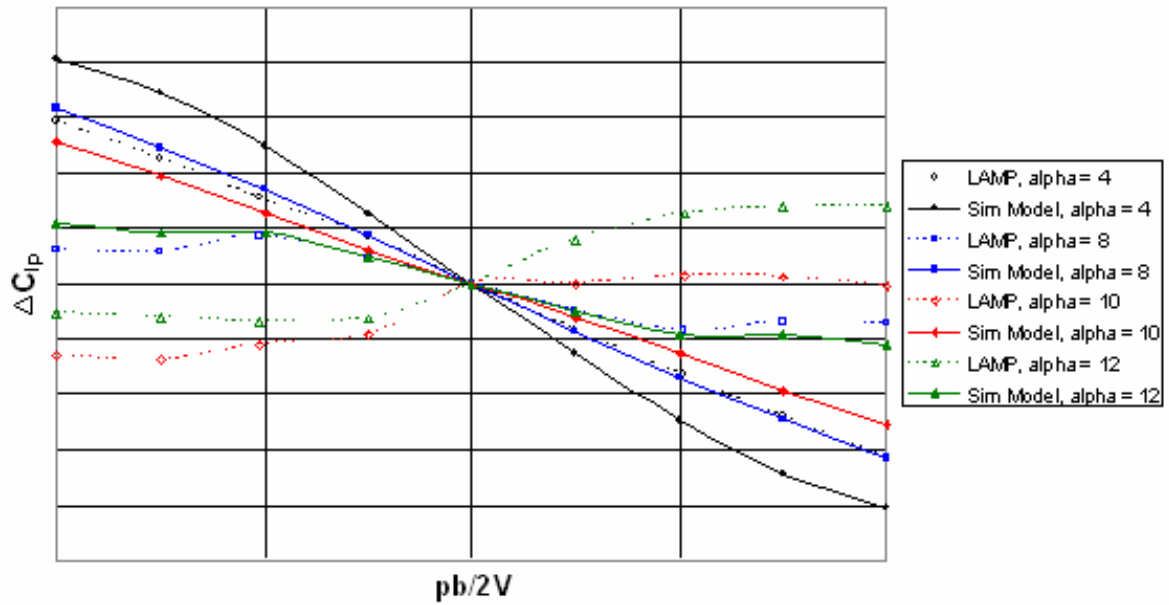


Figure 63. – Comparison of No-ice Incremental Rolling Moment Coefficient due to non-dimensionalized Roll Rate for LAMP Wind Tunnel Data and for the Sim Model Data at selected Angles of Attack, Flaps = 0.

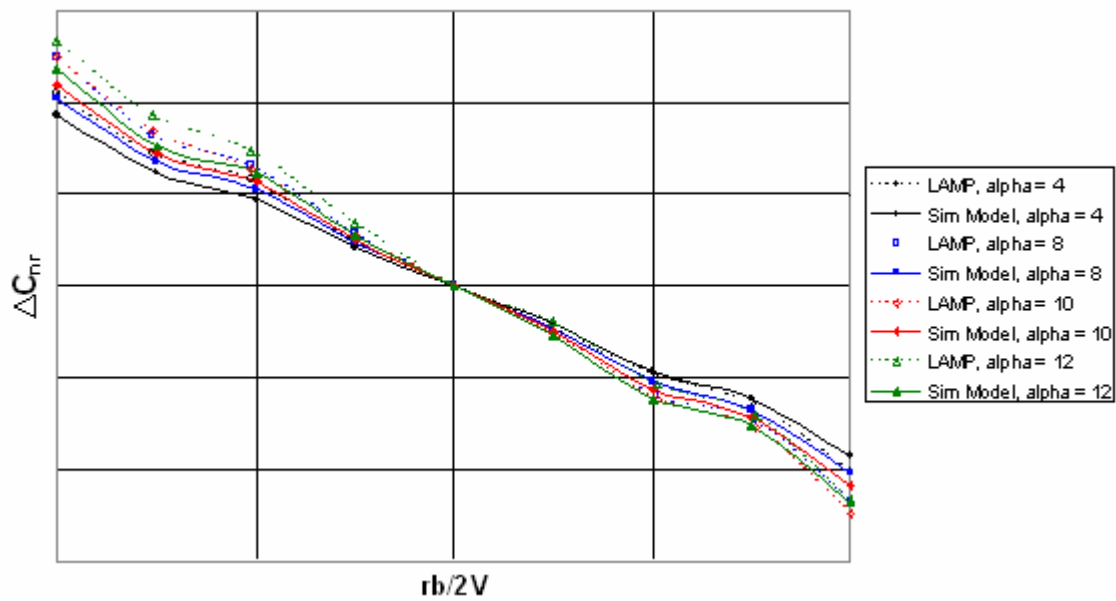


Figure 64. – Comparison of No-ice Incremental Yawing Moment Coefficient due to non-dimensionalized Yaw Rate for LAMP Wind Tunnel Data and for the Sim Model Data at selected Angles of Attack, Flaps = 0.

#### 4.1.2. Iced Airplane Configurations

Additional simulation data base tables were generated to account for the incremental effects of ice on the terms of the aerodynamic coefficients for each of the three icing conditions that were tested. The wind tunnel data for each of the icing conditions were treated as discussed in Section 2.2.7.2 in order to produce simulation data that represented the best estimate of what the full-scale airplane would experience. An example of the incremental icing tables is shown in Figure 65 for the effect of failure ice on the lift coefficient.

In the simulation, a flag is set for the particular ice condition desired and the flag determines which set of incremental tables are added to the other coefficient tables to simulate the ice condition.

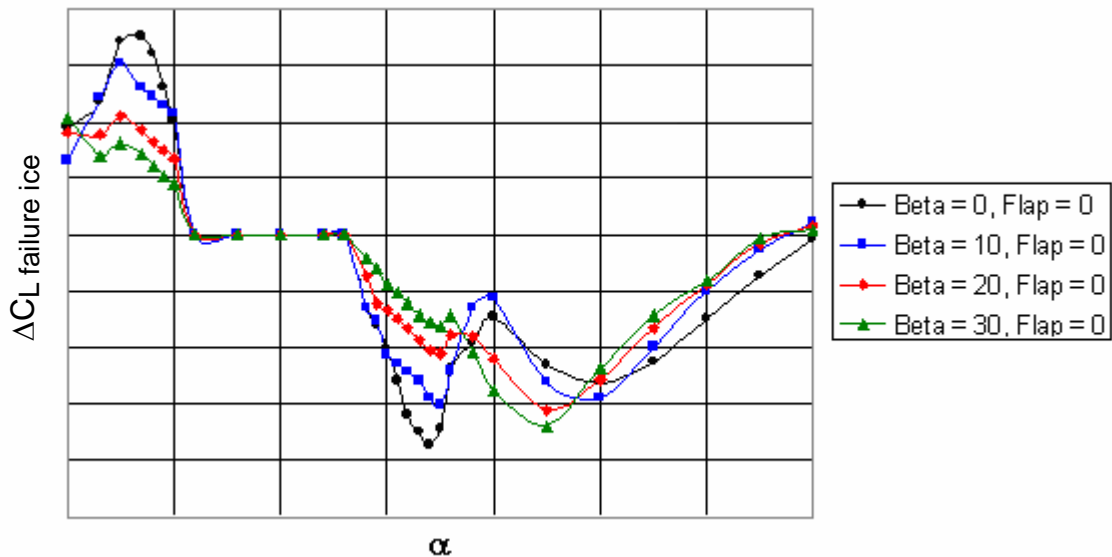


Figure 65. – An Example of the Incremental Tables to Account for the Effects of Icing. In this Case, the Incremental Lift Coefficient due to Failure Ice is Presented as a Function of Angle of Attack and Sideslip.

#### 4.2. *Ice Contamination Effects Flight Training Device*

The business jet simulation databases were then hosted on NASA's Ice Contamination Effects Flight Training Device (ICEFTD). The ICEFTD was developed to provide NASA with a portable device that could be taken to various venues to demonstrate the effects of icing and to provide pilot training on the proper responses to icing encounters.

This is a portable stand-alone device that consists of a raised platform and framework that supports a pilot seat, a control yoke, rudder pedals, a twin throttle

quadrant, three flat panel monitors for out-the-window graphics, and two additional flat panel monitors for instrument panel graphics (Figure 66).

The control column is connected to a programmable loader for longitudinal force feedback, whereas the yoke (lateral) and rudder pedals force gradients are provided by spring resistance. A curtain surrounds the ICEFTD to isolate the pilot from external visual distractions. An instructor station is set up on a table directly behind the ICEFTD (Figure 67). The instructor station consists of a laptop computer to provide control of the simulation (initial conditions, start, stop, etc), video recording and monitoring devices, and an intercom system for communications between the training pilot and the instructor. A second laptop computer is used to transcribe pilot comments and relevant notes during the simulation sessions.



Figure 66. - Ice Contamination Effects Flight Training Device



Figure 67. - Ice Contamination Effects Flight Training Device Setup with Instructor Workstation

The D-Six simulation software that was used for math model development also serves as the host for the ICEFTD simulation and for the graphics displays. The out-the-window view (Figure 68) is generated from a generic terrain model and includes features such as an airport, buildings, trees, and varied terrain elevations. Also sky conditions, based on time of day and cloud bases and tops, are fully programmable. The cloud functions are a key feature used in the scenario-based training module. Winds, turbulence and wind shear are also configurable within D-Six's environmental settings.

The instrument panel graphics (Figure 69) were designed to represent traditional round dial instrument displays typically found in general aviation airplanes with airspeed, attitude, altitude, vertical speed, heading, and turn/bank indicator instruments. Torque pressure, flap position, and elevator trim tab position indicators are also provided.

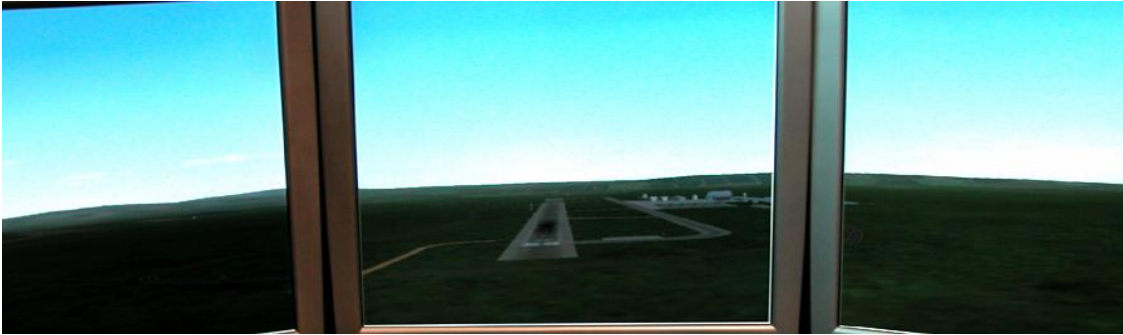


Figure 68. - Out-the-Window graphics



Figure 69. - Instrument panel graphics

The original data base used on the ICEFTD was of NASA's DeHavilland Twin Otter airplane that is used for icing research flights. The D-Six simulation environment permitted the quick and easy change to the business jet data base. The ICEFTD was then used for pilot evaluations during the flight test program and for a final evaluation after the data base was adjusted slightly based on the data from the validation flight tests.

## 5. VALIDATION DATA FLIGHT TEST PROGRAM

A flight test program was undertaken to gather the data required to do validation of the simulation of the iced airplane configurations. The flight tests were performed during September of 2005. The full-scale airplane was configured with the same three icing conditions that were used for the wind tunnel tests of the wings and complete airplane model. In addition, some intermediate conditions were also flown to build up to the final condition when it was a condition that the manufacturer had not previously flight tested for this airplane. For example, the simulated ice was only installed on the inner third of the wing initially and a flight was made to exercise the evaluation maneuvers.



Then the simulated ice was installed on the inner two thirds of the wing and the flight repeated. Finally, the entire wing was fitted with the simulated ice and the final flights with that ice condition were flown.

A series of selected maneuvers were flown for all of the ice conditions at flaps = 0°, 15°, and 35°. They were:

- Stalls
- Roll, pitch, and yaw doublets
- Wind up turns
- 1/2g and 0g push overs
- Roll rate tests (30° to 30° banks) with 1/3, 2/3, and full-throw ailerons
- Steady-heading sideslips
- Thrust transients (accelerations)
- Flap extension and retraction

These were all done at 1.3Vs, 1.5Vs, and 1.7Vs, and some at additional speeds (e.g. Vfe).

The first flights flown were for the inter-cycle (roughness) ice condition. The ice was represented by 40-grit sandpaper attached to the leading edges of the flight surfaces. Because the manufacturer had not flown this ice condition with gear up (although they had flown a similar condition with gear down) flights were flown with a build up to the final configuration for safety reasons. The first flight was flown with the sandpaper on the leading edge of the horizontal and vertical tails, but only on the inner 1/3 of the wing. The second flight had sandpaper on the inner 2/3 of the wing, and the final flight had it on the full wing span. During build up flights, the pilots wore personal chutes and armed an escape hatch in the airplane. For flights that they had done previously for certification they did not use personal chutes, but always flew with a spin chute on the airplane. The test airplane with the sandpaper installed is shown in Figures 70 and 71.





Figure 70. - 40-grit sandpaper (blue area) on wing leading edge to simulate inter-cycle ice.



Figure 71. - 40 grit sandpaper (darker blue areas) on horizontal and vertical tail leading edges to simulate inter-cycle ice.

The second icing condition flown was the run-back ice condition. The ice shapes for this were the same as the ones tested in the wind tunnel. It was assumed that the ice protection system was working and so there was no ice on the wing leading edge, but the run-back shapes were installed where the ice would refreeze aft of the heated area. Also, the ice protection does not run all the way to the wing tip, so there is a small area at the wing tip that is not protected. In this region 45 minute ice shapes were installed (see Figures 72 and 73). The horizontal tail has icing protection on the leading edge except for small areas at the root and tip. As with the wing, 45 minute ice shapes were added to these unprotected areas and the sandpaper was left on the remainder of the horizontal leading edge. The aircraft does not have ice protection on the vertical tail, so 45 minute ice shapes were added to the entire vertical leading-edge, Figure 74.



Figure 72. - View of upper surface run-back ice shape and 45 minute leading edge shape on unprotected wing tip.



Figure 73. - Lower wing surface run-back ice shape.



Figure 74. - Ice shapes used on tail surfaces during run-back and failure ice conditions.



Figure 75. – Horizontal tail ice shapes used during run-back and failure ice condition testing.

The final ice condition was the failure ice. The manufacturer had not flown this ice condition before, so a build up was required for this condition as well. As was done with the sandpaper, the first flight was with the inner 1/3 of the wing iced, the second was with the inner 2/3 and the final with the full span 22.5 minute ice shape (except for the wing tips, which always had the 45 minute ice shape attached). The horizontal and vertical tail surfaces for this ice condition were the same as they had been for the run-back case: sandpaper on the protected areas and 45 minute ice shapes on the unprotected areas. The failure ice shapes are shown installed on the wings in Figures 76 and 77.





Figure 76. - 22.5 minute failure ice shape attached to inner 2/3 of the wing during build up testing and before grit was attached.



Figure 77. – Full span 22.5 minute failure ice attached and gritted.

The results of the flight test were as expected from the results of the wind tunnel tests. The most significant differences were in the stall characteristics with all three of the ice conditions producing higher stall speeds (and lower stall alphas) than the un-iced airplane, as had been predicted. The inter-cycle ice (roughness) condition also produced a significant wing drop at stall which is not present on the un-iced airplane. The other two ice conditions produced little or no wing drop at stall.

The ICEFTD had been brought to the site of the flight testing with the business jet simulation installed. Consequently, it was possible to evaluate how well the models were predicting the results that were seen in the actual flights. The test pilots who were flying the airplane also were able to do a limited evaluation of the simulation shortly after flying the test flights. Some of the initial evaluations were:

- With the roughness, the simulation model over-predicted the decrease in stall angle and in  $CL_{max}$ , but the simulation appeared to be reasonably close on the other two ice conditions.
- The simulation also showed a tendency to pitch up at stall with the flaps down which the airplane did not do. Consequently, it appears that in shifting the pitching moment out to “full-scale” Reynolds’ number, the point where the pitching moment slope becomes positive after stall was not shifted sufficiently.

## **6. FINAL SIMULATION MODEL AND RESULTS**

The D-Six based simulation model was run in overdrive mode using the flight records from the test flights for a more thorough evaluation of the data base. Where differences were noted, the math model was modified to minimize the differences. The D-Six “Overdrive” function is shown schematically in Figure 78. In Overdrive mode the equations of motion are not integrated, but instead are driven by the time histories of the vehicle states. At each time slice, extraction of aerodynamic moment coefficients from the flight recorded time history occurs as shown on the right side of Figure 78. Angular rates are numerically differentiated to obtain the angular acceleration of the vehicle. After the removal of the inertial effects, the remainder is non-dimensionalized to calculate the aerodynamic force and moment coefficients experienced during flight. Also, at each time step, flight-recorded states, such as angle of attack, angle of sideslip, control surface positions, etc., are used to exercise the aerodynamic model in accordance with the aerodynamic model specification discussed previously. Each aerodynamic model element (i.e., pitching moment due to elevator, etc.) is stored and summed as prescribed in the aerodynamic model. By over-plotting the model predicted coefficients with the flight extracted total coefficients, differences can be easily identified. Correlating the

discrepancies with the excitation of the individual elements and parameters from the flight time history aids to isolate potential weaknesses in the aerodynamic model.

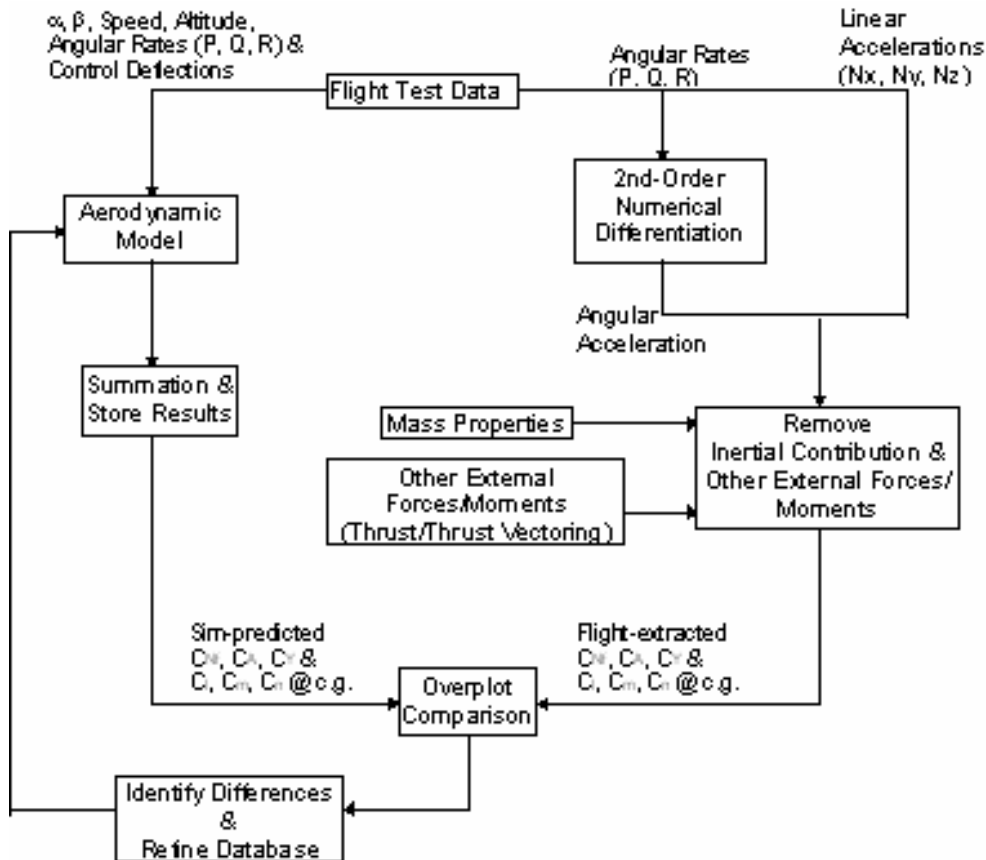
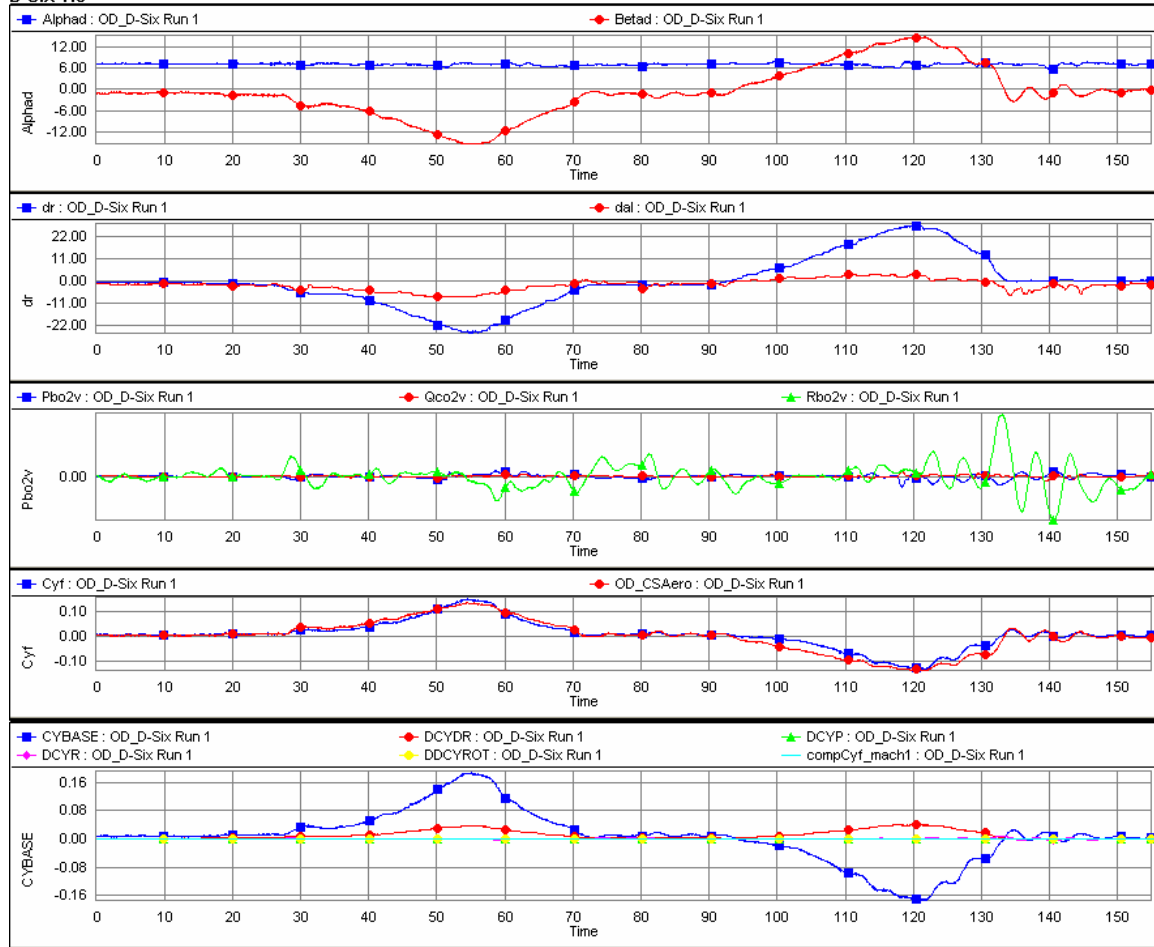


Figure 78. – Schematic of the Overdrive Procedure.

Selected Overdrive time history plots from the final validation effort have been reproduced here to demonstrate the excellent correlation of the model with the flight extracted coefficients (Figures 79 through 83). Overall, the original models proved to be very good at simulating the airplane both for an un-iced condition and for the three iced conditions that were modeled. Only relatively minor adjustments were required to the simulation data base to obtain the results shown. During the validation effort, the stall time histories were the primary source for evaluation of the icing effects because the influence of the ice condition on the stalls were the most noticeable effects. The control doublets were used primarily to evaluate control effectiveness and vehicle dynamics. The other maneuvers were used where required to verify and validate other aspects of the simulation.

# D-Six 1.9



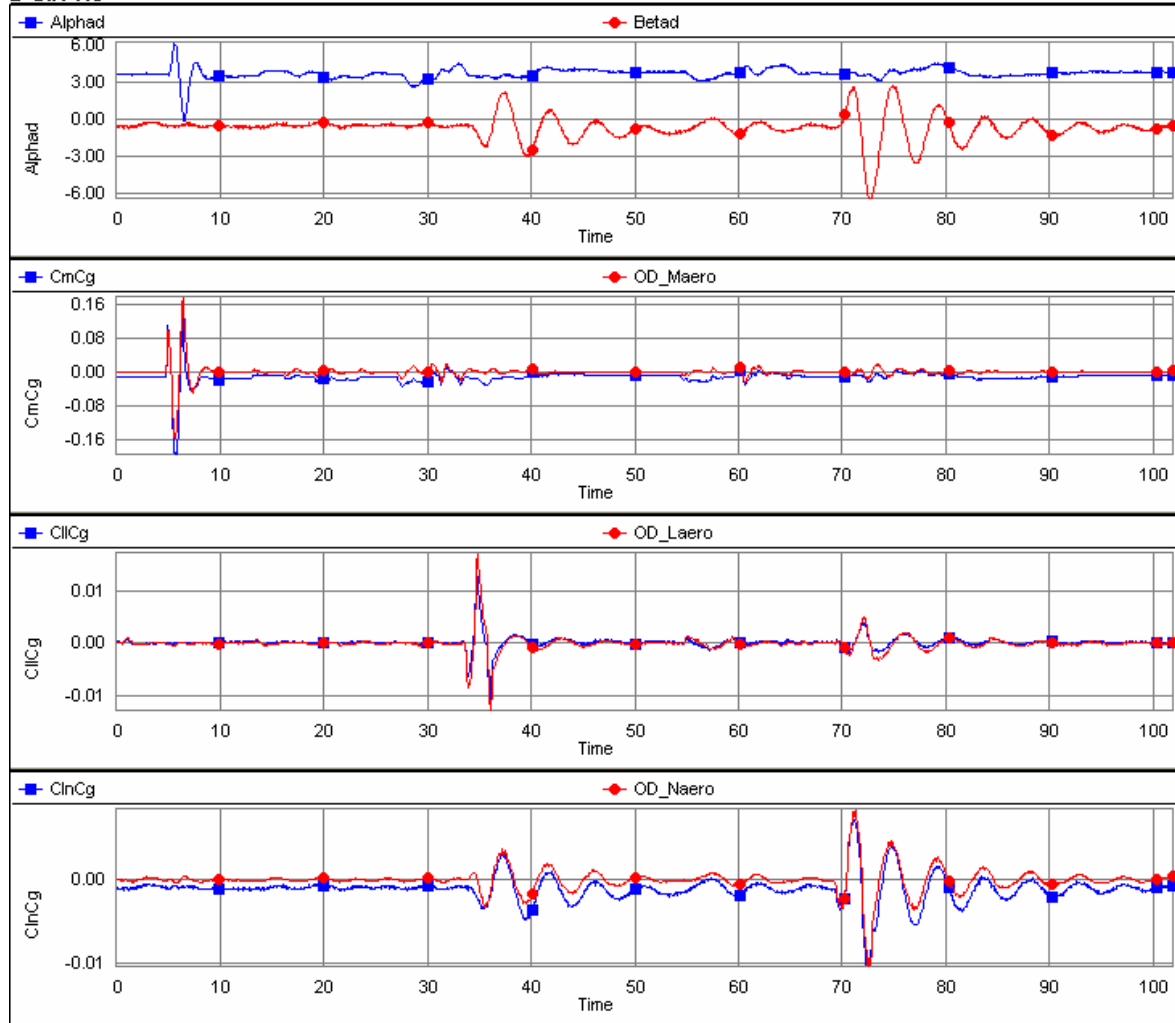
10/02/2006 18:13:12 Default Plot Template

Figure 79. – Overdrive time histories for a steady-heading sideslip maneuver.

Figure 79 shows the side force coefficient for both the simulation and the flight test airplane during a steady-heading sideslip. The angle of attack and sideslip angle are shown from flight, as well as the rudder and aileron deflections. The total side force coefficient and the contributions of each of the components that make up the total coefficient are shown.



# D-Six 1.9

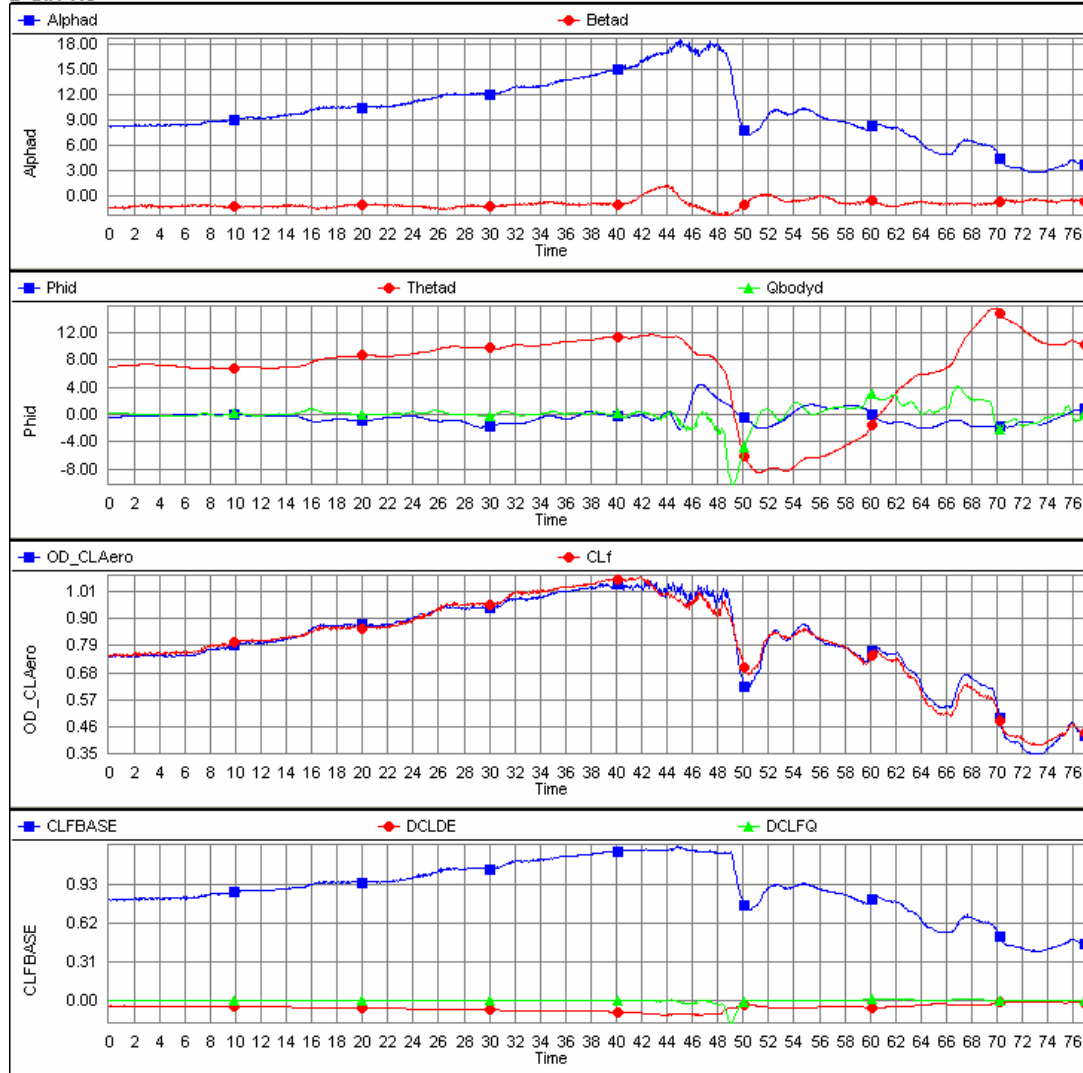


10/03/2006 15:05:47 Default Plot Template

Figure 80. – Overdrive time histories for pitch, roll, and yaw doublets with 15° flaps.

An overdrive run for doublets in each of the axis is shown in Figure 80. In general, the simulated airplane's change in coefficients due to the control inputs matches very well, as does the airplane's frequency and damping characteristics. It should be noted that there is a small steady-state sideslip angle in the flight record that does not appear to produce any moments, so it is assumed that this is an instrumentation produced reading. When the model is overdriven, however, it will produce an offset in yawing moment, as shown in the  $Cln$  time histories.

# D-Six 1.9

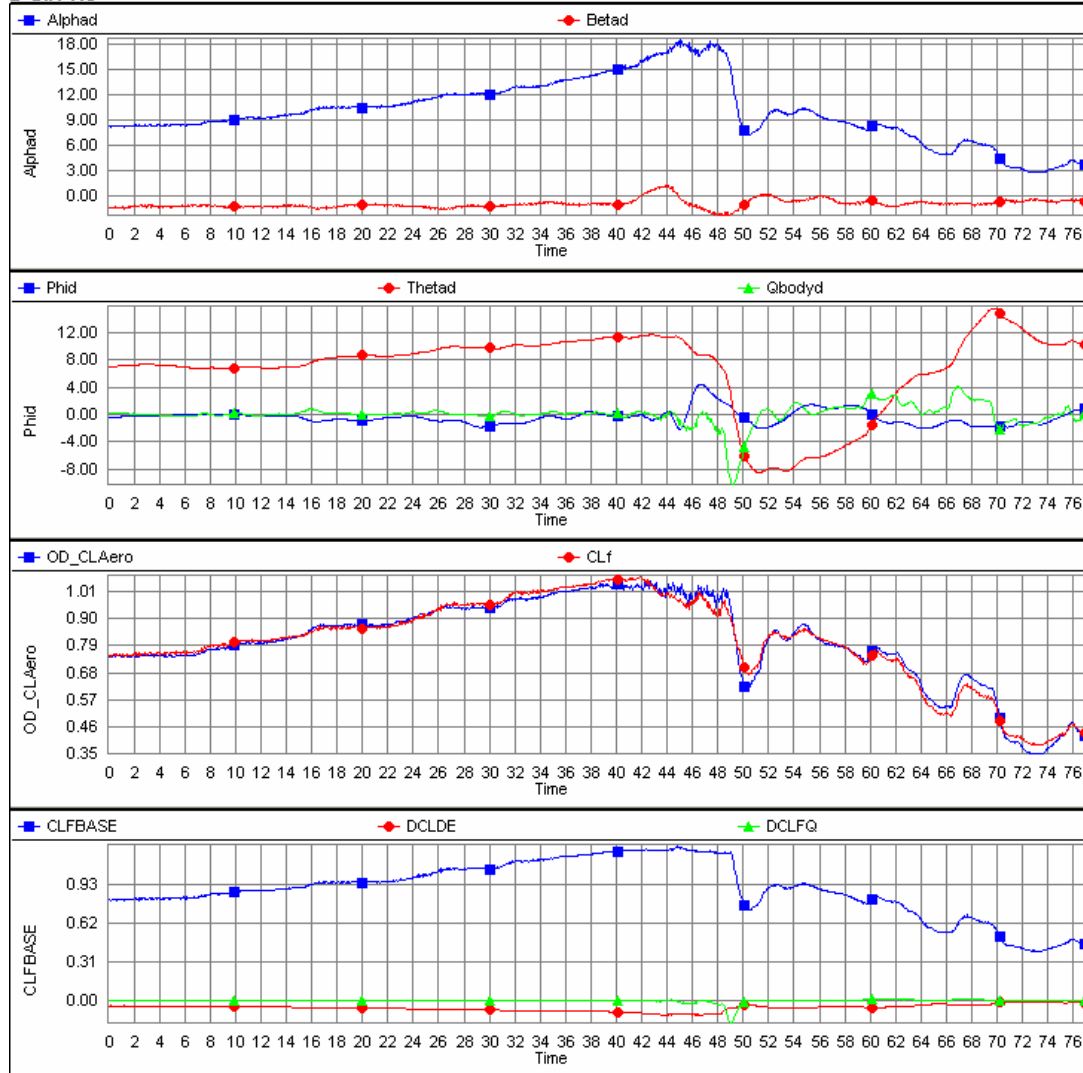


10/02/2006 17:30:30 Default Plot Template

Figure 81. – Overdrive time histories for a Clean airplane 0° flap stall.

Figures 81 through 83 show lift coefficient time history overdrive runs of stalls for a clean airplane, for an airplane with failure ice, and for one with inter-cycle ice. As is shown, very good correlations were obtained for these stall conditions throughout the time history record.

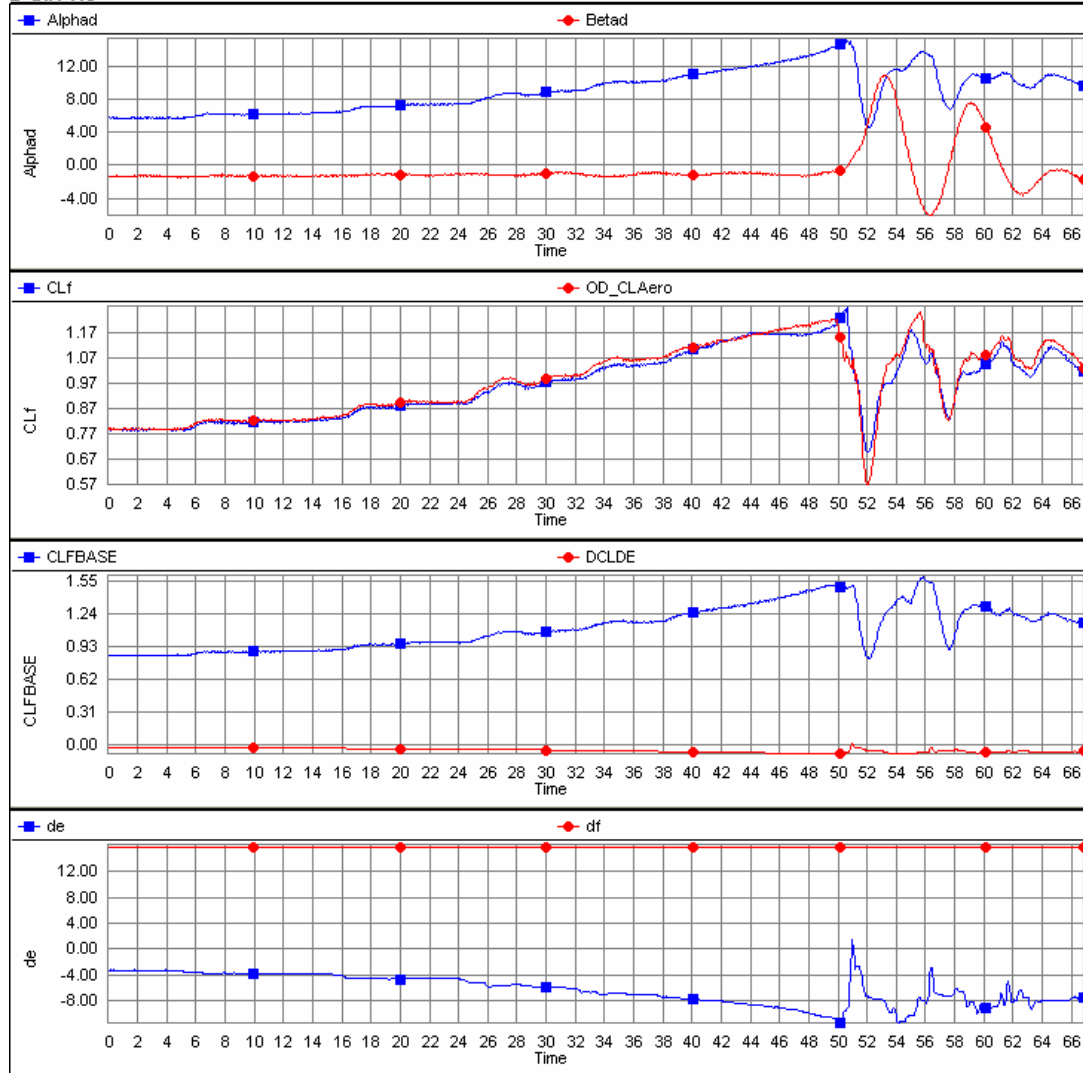
# D-Six 1.9



10/02/2006 17:30:30 Default Plot Template

Figure 82. – Overdrive stall time histories for an airplane with failure ice condition.

# D-Six 1.9



10/04/2006 21:53:05 Default Plot Template

Figure 83. – Overdrive stall time histories for an inter-cycle (roughness) ice condition,

## 7. CONCLUDING REMARKS

A process was demonstrated for developing representative iced airplane simulation data bases from wind tunnel data for a business jet type airplane. The study used various scale wing panel tests to identify the influences of the simulated ice shapes at various Reynolds number. Based on these tests, methods were developed to “adjust” the low Reynolds number data to flight Reynolds number for each of the ice conditions. When the adjustment techniques were applied to low Reynolds number complete airplane data, the initial results were very representative of the full-scale airplane characteristics. Some minor adjustments were made to the math model to improve the correlation to the flight records, but these were comparable to similar adjustments that are normally made to improve low-speed wind tunnel based simulation models of un-iced airplanes.

The results of this program, when combined with the results of the preceding Twin Otter program, indicate that it is likely that there are little Reynolds number corrections required for failure ice simulations using low Reynolds number test data, at least for wings without leading-edge high lift devices. This is apparently because the upper ice “horn” sets the separation point at high angles of attack almost independently of the Reynolds number.

The inter-cycle (roughness) ice and the runback ice cases required careful correction of the low speed data to represent the full-scale airplane, as well as picking the proper equivalent ice representation that gave low-speed results that were proportionately similar to their effects at full-scale aircraft Re. As a result, additional configurations would need to be similarly evaluated before any conclusions can be made as to whether it will be necessary to do the wing panel Reynolds number study prior to the complete airplane tests for future modeling of these types of ice configurations.

## 8. REFERENCES

1. Gingras, D.R, Dickes, E.G, Ratvasky, T.P., and Barnhart, B.P, "Modeling of In-Flight Icing Effects for Pilot Training," AIAA Modeling and Simulation Technologies Conference and Exhibit, Aug. 5-8, 2002, Monterey, CA, AIAA Paper 2002-4605.
2. Ratvasky, T.P, Ranaudo, R.J., Barnhart, B.P., Dickes, E.G, and Gingras, D.R, "Development and Utility of a Piloted Flight Simulator for Icing Effects Training," AIAA 41st Aerospace Sciences Meeting and Exhibit, Jan. 6-9, 2003, Reno, NV, AIAA Paper 2003-0022.
3. Papadakis, M., Gile Laflin, B.E., Youssef, G.M, and Ratvasky, T.P., "Aerodynamic Scaling Experiments with Simulated Ice Accretions," AIAA 39th Aerospace Sciences Meeting and Exhibits, Jan. 8-11, 2001, Reno, NV, AIAA Paper 2001-0833.
4. Lee, S., Ratvasky, T.P., Thacker, M., and Barnhart, B.P., "Geometry and Reynolds Number on an Iced Business Jet Wing," AIAA 43<sup>rd</sup> Aerospace Sciences Meeting and Exhibits, Jan. 10-13, 2005, Reno, NV, AIAA Paper 2005-1066.
5. Lee, S., Barnhart, B., Ratvasky, T.P., and Thacker, M., "Dynamic Wind-Tunnel Testing of a Sub-Scale Iced Business Jet," AIAA 44<sup>th</sup> Aerospace Sciences Meeting and Exhibits, Jan. 9-12, 2006, Reno, NV, AIAA Paper 2006-0261.

Table 6. – Configurations and file names for LAMP complete airplane tests.

Configuration	$\alpha$	$\beta$	$\delta_e$	$\delta_r$	$\delta_a$	Flaps	Ice	Stat/ Rot	File Name	Comments
BWNYAVH3s	$\alpha_2$	0	0	0	0/0	0	None	Stat	R01	
SBWNYAVH3sp+5		5						Stat	R02	
SBWNYAVH3sp-5		-5						Stat	R03	
SBWNYAVH3sp-15		-15						Stat	R04	
SBWNYAVH3sp+15		15						Stat	R05	
BWNYAVH3sp+10		10						Stat	R06	
BWNYAVH3sp-10		-10						Stat	R07	
SBWNYAVH3sp+20		20						Stat	R08	
SBWNYAVH3sp-20		-20						Stat	R09	
SBWNYAVH3sp-30		-30						Stat	R10	
SBWNYAVH3sp+30		30						Stat	R11	
SBWNYAVH3s-20e		0	-20					Stat	R12	
SBWNYAVH3sp+10-20e		10						Stat	R13	
SBWNYAVH3s-10e		0	-10					Stat	R14	
SBWNYAVH3s-5e		0	-5					Stat	R15	
SBWNYAVH3s+5e		0	5					Stat	R16	
SBWNYAVH3s+10e		0	10					Stat	R17	
SBWNYAVH3s+15e		0	15					Stat	R18	
SBWNYAVH3sp+10+15e		10						Stat	R19	
BWNYAVH3s		0	0					Rot	R61	
BWNYAVH3sp+10		10						Rot	R62	
BWNYAVH3sp-10		-10						Rot	R63	
SBWNYAVH3s+35r		0		35				Stat	R20	
SBWNYAVH3sp+10+35r		10						Stat	R22	
SBWNYAVH3sp-10+35r		-10						Stat	R21	

Table 6. – Continued.

Configuration	$\alpha$	$\beta$	$\delta_e$	$\delta_r$	$\delta_a$	Flaps	Ice	Stat/ Rot	File Name	Comments	
SBWNYAVH3s+10r	$\alpha_2$	0	0	10	0/0	0	None	Stat	R23		
SBWNYAVH3sp-10+10r		-10						Stat	R24		
SBWNYAVH3sp-15+10r		-15						Stat	R25		
SBWNYAVH3sp+10+10r		10						Stat	R26		
SBWNYAVH3sp+15+10r		15						Stat	R27		
SBWNYAVH3sp-10-25/0a		-10		0	-25/0			Stat	R36		
SBWNYAVH3s-25/0a		0						Stat	R28		
SBWNYAVH3sp+10-25/0a		10						Stat	R35		
SBWNYAVH3s-10/0a		0						-10/0	Stat	R34	
SBWNYAVH3s+10/0a		0						10/0	Stat	R33	
SBWNYAVH3s+20/0a		0			20/0			Stat	R29		
SBWNYAVH3s+20/0a+grnyfl		0						Stat	R30	1/16"x1/8" strip	
SBWNYAVH3sp+10+20/0a		10						Stat	R32		
SBWNYAVH3sp-10+20/0a		-10						Stat	R31		
SBWNYAVH3s+40fl		0						0/0	Stat	R37	
SBWNYAVH3s+40fl+grnyfl	$\alpha_3$	0	Stat	R38	1/16X1/8" strip upper surf.						
SBWNYAVH3s+40fl grnyfl2		0	Stat	R39	1/16X1/8" strip lower surf.						
SBWNYAVH3sp+10+40fl	$\alpha_2$	10	Stat	R40							
SBWNYAVH3sp-10+40fl		-10	Stat	R41							
SBWNYAVH3sp-20+40fl		-20	Stat	R42							
SBWNYAVH3sp+20+40fl		20	Stat	R43							
SBWNYAVH3s+40fl-20e		0	-20	Stat	R44						
SBWNYAVH3sp+10+40fl-20e	10	Stat		R45							
SBWNYAVH3s+40fl+15e	0	15	Stat	R46							
SBWNYAVH3sp+10+40fl+15e	10		Stat	R47							



Table 6. – Continued.

Configuration	$\alpha$	$\beta$	$\delta_e$	$\delta_r$	$\delta_a$	Flaps	Ice	Stat/ Rot	File Name	Comments	
SBWNYAVH3s+40fl-25/0a	$\alpha_2$	0	0	0	-25/0	40	None	Stat	R48		
SBWNYAVH3s p-10+40fl-25/0a		-10						Stat	R50		
SBWNYAVH3sp+10+40fl-25/0a		10						Stat	R49		
SBWNYAVH3s+40fl+20/0a		0						+20/0	Stat	R51	
SBWNYAVH3sp-10+40fl+20/0a		-10							Stat	R53	
SBWNYAVH3sp+10+40fl+20/0a		10							Stat	R52	
SBWNYAVH3s+40fl		0			0/0	<b>Rot</b>		R64			
SBWNYAVH3sp+10+40fl		10				<b>Rot</b>		R65			
SBWNYAVH3sp-10+40fl		-10				<b>Rot</b>		R66			
SBWNYAVH3s+20fl		0				20		Stat	R54		
SBWNYAVH3sp+10+20fl		10						Stat	R55		
SBWNYAVH3sp-10+20fl		-10						Stat	R56		
SBWNYAVH3s+20fl-20e		0	-20		Stat			R57			
SBWNYAVH3sp+10+20fl-20e		10			Stat			R58			
SBWNYAVH3s+20fl+15e		0	15		Stat			R59			
SBWNYAVH3sp+10+20fl+15e		10			Stat	R60					
SBWNYAVH3s+20fl		0	0		<b>Rot</b>	R67					
SBWNYAVH3sp+10+20fl		10			<b>Rot</b>	R68					
SBWNYAVH3sp-10+20fl		-10			<b>Rot</b>	R69					

Table 6. – Continued.

Configuration	$\alpha$	$\beta$	$\delta_e$	$\delta_r$	$\delta_a$	Flaps	Ice	Stat/ Rot	File Name	Comments
SBWNYAVH3sFI	$\alpha_2$	0	0	0	0/0	0	Failure	Stat	R70	Lewice on wing, VT, HT@
SBWNYAVH3sFIp+10		10						Stat	R71	Unprotected areas – 40 grit
SBWNYAVH3sFIp-10		-10						Stat	R72	elsewhere
SBWNYAVH3sFIp+15		15						Stat	R73	
SBWNYAVH3sFIp-15		-15						Stat	R74	
SBWNYAVH3sFI-20e		0	-20					Stat	R78	
SBWNYAVH3sFIp+10-20e		10						Stat	R79	
SBWNYAVH3sFI+15e		0	15					Stat	R80	
SBWNYAVH3sFIp+10+15e		10						Stat	R81	
SBWNYAVH3sFIp+10+10r		10	0	10				Stat	R82	
SBWNYAVH3sFI-25/0a		0		0	-25/0			Stat	R83	
SBWNYAVH3sFI+20/0a		0			+20/0			Stat	R84	
BWNYAVH3sFI		0		0/0	Rot			R75		
BWNYAVH3sFIp+10		10			Rot			R76		
BWNYAVH3sFIp-10		-10			Rot			R77		
SBWNYAVH3sFI+20fl		0		20	Stat	R94				
SBWNYAVH3sFIp+10+20fl		10			Stat	R95				
SBWNYAVH3sFIp-10+20fl		-10	Stat		R96					
SBWNYAVH3sFI+20fl-20e		0	-20		Stat	R97				
SBWNYAVH3sFIp+10+20fl-20e		10			Stat	R98				
SBWNYAVH3sFI+20fl+15e		0	15		Stat	R99				
SBWNYAVH3sFIp+10+20fl+15e		10			Stat	R100				
BWNYAVH3sFI+20fl	$\alpha_4$	0	0		Rot	R101				
BWNYAVH3sFIp+10+20fl	$\alpha_4$	10			Rot	R102				

Table 6. – Continued.

Configuration	$\alpha$	$\beta$	$\delta_e$	$\delta_r$	$\delta_a$	Flaps	Ice	Stat/ Rot	File Name	Comments		
SBWNYAVH3sFI+40fl	$\alpha_2$	0	0	0	0/0	40	Failure	Stat	R85	Lewice on wing, VT, HT@		
SBWNYAVH3sFIp+10+40fl		10						Stat	R86	Unprotected areas – 40 grit		
SBWNYAVH3sFIp-10+40fl		-10						Stat	R87	elsewhere		
SBWNYAVH3sFI+40fl-20e		0	-20					Stat	R88			
SBWNYAVH3sFIp+10+40fl-20e		10						Stat	R89			
SBWNYAVH3sFI+40fl+15e		0	15					Stat	R90			
SBWNYAVH3sFIp+10+40fl+15e		10						Stat	R91			
BWNYAVH3sFI+40fl		0						Rot	R92			
BWNYAVH3sFIp+10+40fl		$\alpha_4$	10									Rot
SBWNYAVH3s40g	$\alpha_2$	0	0	0	0/0	0	Rough	Stat	R154	40 grit on wing, VT & HT		
SBWNYAVH3s40gp+10		10						Stat	R155			
SBWNYAVH3s40gp-10		-10						Stat	R156			
SBWNYAVH3s40g-20e		0	-20					Stat	R160			
SBWNYAVH3s40g+15e		0						+15	Stat	R161		
SBWNYAVH3s40g-25/0a		0			-25/0				Stat	R162		
SBWNYAVH3s40gp+10-25/0a		10	Stat						R163			
SBWNYAVH3s40Gp-10-25/0a		-10	Stat					R164				
SBWNYAVH3s40g+20/0a		0	+20/0		Stat			R165				
SBWNYAVH3s40gp+10+20/0a		10			Stat			R166				
SBWNYAVH3s40gp-10+20/0a		-10			Stat			R167				
BWNYAVH3s40g			0						Rot	R157		
BWNYAVH3s40gp+10		$\alpha_5$	+10							Rot	R158	
BWNYAVH3s40gp-10		$\alpha_5$	-10							Rot	R159	

Table 6. – Continued.

Configuration	$\alpha$	$\beta$	$\delta_e$	$\delta_r$	$\delta_a$	Flaps	Ice	Stat/ Rot	File Name	Comments
SBWNYAVH3s40g+20fl	$\alpha_2$	0	0	0	0/0	20	Rough	Stat	R175	40 grit on wing, VT & HT
SBWNYAVH3s40gp+10+20fl		10						Stat	R176	
SBWNYAVH3s40gp-10+20fl		-10						Stat	R177	
SBWNYAVH3s40g+20fl-20e		0	-20					Stat	R179	
SBWNYAVH3s40g+20fl+15e		0	+15					Stat	R180	
BWNYAVH3s40g+20fl		0	0					Rot	R178	
BWNYAVH3s40gp+10+20fl		10						Rot	R181	
SBWNYAVH3s40g+40fl		0				40		Stat	R168	
SBWNYAVH3s40g+10+40fl		10						Stat	R169	
SBWNYAVH3s40g-10+40fl		10						Stat	R170	
SBWNYAVH3s40g+40fl-20e		0	-20					Stat	R173	
SBWNYAVH3s40g+40fl+15e		0	+15					Stat	R174	
BWNYAVH3s40g+40fl		0	0					Rot	R171	
BWNYAVH3s40g+10+40fl		0						Rot	R172	
SBWNYAVH3sRB	$\alpha_2$	0	0	0	0/0	0	Runback	Stat	R103	3/32" sq on bottom of wing,
SBWNYAVH3sRBp+10		10						Stat	R104	0.025" piano wire on upper.
SBWNYAVH3sRBp-10		-10						Stat	R105	VT & HT and wing tips same
SBWNYAVH3sRB-20e		0	-20					Stat	R106	As failure case
SBWNYAVH3sRB+15e		0	15					Stat	R107	
SBWNYAVH3sRB-25/0a		0	0	0	-25/0			Stat	R108	
SBWNYAVH3sRBp+10-25/0a		10						Stat	R109	
SBWNYAVH3sRBp-10-25/0a		-10						Stat	R110	
SBWNYAVH3sRB+20/0a		0			+20/0			Stat	R111	
SBWNYAVH3sRBp+10+20/0a		10						Stat	R112	
SBWNYAVH3sRBp-10+20/0a	$\alpha_3$	-10						Stat	R113	

Table 6. – Continued.

Configuration	$\alpha$	$\beta$	$\delta_e$	$\delta_r$	$\delta_a$	Flaps	Ice	Stat/ Rot	File Name	Comments
BWNYAVH3sRB	$\alpha_2$	0	0	0	0/0	0	Runback	<b>Rot</b>	R114	3/32” sq on bottom of wing,
BWNYAVH3sRBp+10	$\alpha_5$	10						<b>Rot</b>	R115	0.025” piano wire on upper.
BWNYAVH3sRBp-10	$\alpha_5$	-10						<b>Rot</b>	R116	VT & HT and wing tips same
SBWNYAVH3sRB+20fl	$\alpha_2$	0			20	Stat		R124	As failure case	
SBWNYAVH3SrbP+10+20fl		10				Stat		R125		
SBWNYAVH3sRBp-10+20fl		-10				Stat		R126		
SBWNYAVH3sRB+20fl-20e		0				-20		Stat	R127	
SBWNYAVH3sRB+20fl+15e	0	15				Stat		R128		
BWNYAVH3sRB+20fl	$\alpha_5$	0				0		<b>Rot</b>	R129	
BWNYAVH3sRBp+10+20fl	$\alpha_7$	0						<b>Rot</b>	R130	
SBWNYAVH3sRB+40fl	$\alpha_2$	0				40		Stat	R117	
SBWNYAVH3sRBp+10+40fl		10			Stat			R118		
SBWNYAVH3sRBp-10+40fl		-10			Stat			R119		
SBWNYAVH3sRB+40fl-20e		0			-20			Stat	R120	
SBWNYAVH3sRB+40fl+15e	0	15			Stat			R121		
BWNYAVH3sRB+40fl	$\alpha_5$	0			0			<b>Rot</b>	R122	
BWNYAVH3sRBp+10+40fl	$\alpha_5$	10					<b>Rot</b>	R123		
IBWNYAVH3s	$\alpha_6$	0	0	0	0/0		0	Clean	Stat	R145
IBWNYAVH3s+40fl		0				40			Stat	R146
IBWNYAVH3s40g+40fl		0				40	Rough	Stat	R152	
BWNYAVH3SFI2	4	0	0	0	0/0	0	Fail 2	<b>Rot</b>	R182	Only 22.5 min shape
BWNYAVH3SFlequiv	4	0					3/32” sq	<b>Rot</b>	R183	3/32”n sq balsa strip at upper horn position

Table 6. – Concluded.

Configuration	$\alpha$	$\beta$	$\delta_e$	$\delta_r$	$\delta_a$	Flaps	Ice	Axis	File Name	Comments
YBWNVAVH3sRB	$\alpha_2$	0	0	0	0/0	0	Runback	Yaw	R131	Forced Oscillation Runs
RBWNVAVH3sRB	$\alpha_2'$							Roll	R132	
RBWNVAVH3sRB+40fl	$\alpha_2'$							Roll	R133	
PBWNVAVH3sRB	$\alpha_2$							Pitch	R134	
PBWNVAVH3sRB+40fl	$\alpha_2$							Pitch	R135	
PBWNVAVH3sFI	$\alpha_2$					0	Failure	Pitch	R136	
PBWNVAVH3sFI+40fl	$\alpha_2$							Pitch	R137	
RBWNVAVH3sFI	$\alpha_2'$							Roll	R138	
RBWNVAVH3sFI+40fl	$\alpha_2'$							Roll	R139	
YBWNVAVH3sFI	$\alpha_2$							Yaw	R140	
YBWNVAVH3s	$\alpha_2$					0	Clean	Yaw	R141	
RBWNVAVH3s	$\alpha_2'$							Roll	R142	
RBWNVAVH3s+40fl	$\alpha_2'$							Roll	R143	
PBWNVAVH3s	$\alpha_2$							Pitch	R146	
PBWNVAVH3s+40fl	$\alpha_2$							Pitch	R147	
PBWNVAVH3s40g	$\alpha_2$					0	Rough	Pitch	R148	
PBWNVAVH3s40g+40fl	$\alpha_2$							Pitch	R149	
YBWNVAVH3s40g	$\alpha_2$							Yaw	R153	
RBWNVAVH3s40g	$\alpha_2'$							Roll	R150	
RBWNVAVH3s40g+40fl	$\alpha_2'$							Roll	R151	

 $\alpha_1$ : 0, 4, 6, 8, 9, 10, 11, 12, 14, 16, 18, 20, 25, 30, 35, 40, 45, 50 $\alpha_2$ : 0, 4, 6, 8, 9, 10, 11, 12, 13, 14, 15, 16, 18, 20, 25, 30, 35, 40, 45, 50 $\alpha_3$ : 0, 4, 6, 8, 9, 10, 11, 12, 13, 14, 15, 16, 18, 20 $\alpha_4$ : 0, 4, 6, 8, 9, 10, 11, 12, 13, 14, 15, 16, 18, 20, 25, 30 $\alpha_5$ : 0, 4, 6, 8, 9, 10, 11, 12, 13, 14, 15, 16, 18, 20, 25 $\alpha_6$ : -2, -4, -6, -8, -10, -12, -14, -16, -18, -20 $\alpha_7$ : 0, 4, 6, 8, 9, 10, 11, 12, 13, 14